Modélisation multiphysique basée images, évaluation de la durée de vie et analyse des scénarios de rupture des mini-composites à matrice céramique auto-cicatrisante sous tension

Giulia Bellezza

THÈSE PRÉSENTÉE
POUR OBTENIR LE GRADE DE

DOCTEUR DE

L'UNIVERSITÉ DE BORDEAUX

ÉCOLE DOCTORALE MATHÉMATIQUES ET INFORMATIQUE
Mathématiques Appliquées et Calcul Scientifique

Par **Giulia Bellezza**

Image-based multiphysics modelling, lifetime evaluation, and failure scenario analysis of self-healing Ceramic-Matrix mini-Composites under a tensile load

Sous la direction de **Mario Ricchiuto** et **Gérard L. Vignoles**

Soutenue le 20 Septembre 2022

Membres du jury :

M.	BARANGER, Emmanuel	Chargé de recherche	CNRS, LMPS	Rapporteur
M.	GIGLIOTTI, Marco	Professeur	ISAE-ENSMA, PPRIME	Rapporteur
Mme.	CATAPANO, Anita	Maître de conférences	Bordeaux INP, I2M	Examinateur
Mme.	CINEFRA, Maria	Associate Professor	Politecnico di Bari	Examinateur
M.	COUDIÈRE, Yves	Professeur	IMB, Université de Bordeaux	Examinateur
M.	GENET, Martin	Maître de conférences	École Polytechnique, LMS	Examinateur
M.	COUÉGNAT, Guillaume	Chargé de recherche	CNRS, LCTS	Invité

Modélisation multiphysique basée images, évaluation de la durée de vie et analyse des scénarios de rupture des mini-composites à matrice céramique auto-cicatrisante sous tension

Resumé

La présente thèse se propose de développer un modèle capable de décrire le comportement auto-cicatrisant des composites à matrice céramique destinés à être utilisés dans les parties chaudes des turbines d'avion et d'étudier l'effet des interactions physiques, chimiques et mécaniques complexes en termes de durée de vie. L'intérêt pour ces matériaux est dû à leur durée de vie extrêmement élevée en raison de leur capacité à cicatriser leurs fissures par l'action d'un oxyde protecteur. La première partie du manuscrit est consacrée à la description du modèle numérique construit pour caractériser le comportement et la rupture d'un mini-composite sous une charge de traction à partir d'un modèle bidimensionnel basé image d'une fissure transversale. Un système d'EDP et d'EDO moyennées sur une fissure est proposé pour le transport de l'oxygène et de l'évolution de toutes les espèces chimiques impliquées dans le processus de cicatrisation. La forme adimensionnelle des équations est étudiée pour effectuer les choix de discrétisation les plus appropriés concernant l'intégration temporelle et les conditions aux limites. Concernant la dégradation des fibres, un modèle de propagation sous-critique des défauts dépendant explicitement des paramètres environnementaux est calibré en utilisant une solution exacte particulière impliquant des paramètres externes constants et intégré numériquement dans le cas général. La rupture du fil résulte de la distribution statistique de la résistance initiale des fibres, de la cinétique de croissance progressive des défauts et du mécanisme de répartition de la charge suite à la rupture des fibres. Ce processus est décrit par un modèle mécanique analytique. Les capacités de prédiction de la durée de vie du modèle numérique multi-physique résultant, ainsi que l'impact de la température, de la charge appliquée, de la variation spatiale de la distribution statistique de la résistance des fibres et de la forme et de la taille du fil sont étudiés dans la deuxième partie du mémoire. Enfin, pour examiner le degré de variabilité de la durée de vie calculée, une étude de quantification des incertitudes ainsi qu'une analyse de sensibilité de ce modèle sont proposées afin d'estimer ses marges de fiabilité et de décrire précisément comment l'incertitude des paramètres d'entrée se propage dans la simulation.

Mots clés : composites à matrice céramique, cicatrisation, fissuration sous-critique, modélisation basée sur l'image, quantification de l'incertitude

Image-based multiphysics modelling, lifetime evaluation, and failure scenario analysis of self-healing Ceramic-Matrix mini-Composites under a tensile load

Abstract

This thesis aims to develop a model capable of describing the self-healing behaviour of ceramic matrix composites considered for use in hot parts of aircraft turbines and to investigate the effect of complex physical, chemical and mechanical interactions in terms of lifetime. The interest in these materials is due to their extremely long lifetime because of their ability to heal cracks by the action of a protective oxide. The first part of the manuscript is devoted to the description of the numerical model built to characterize the behaviour and failure of a mini-composite under a tensile load proceeding from a two-dimensional image-based model of a transverse crack. A system of crack-averaged PDEs and ODEs is proposed for the transport of oxygen and of all the chemical species involved in the healing process. The dimensionless form of the equations is studied to perform the most appropriate discretization choices concerning time integration and boundary conditions. Concerning the fibres' degradation, a slow crack growth model explicitly dependent on the environmental parameters is calibrated using a particular exact solution involving constant external parameters and integrated numerically in the general case. The tow failure results from the statistical distribution of the fibres' initial strength, the slow crack growth kinetics, and the load transfer following fibres breakage. The latter is described via an analytical mechanical model. The lifetime prediction capabilities of the resulting multi-physics numerical model, as well as the impact of temperature, applied load, spatial variation of the statistical distribution of fibres strength and tow's shape and size are investigated in the second part of the thesis. Moreover, to examine the degree of the related variability of the evaluated lifetime shown by the results, an uncertainty quantification study together with a sensitivity analysis of our model are proposed to specify the reliability domain of the model and to describe accurately how the uncertainty of the input parameters can be propagated throughout the simulations.

Keywords : ceramic-matrix composites, self-healing, slow crack growth, image-based modeling, uncertainty quantification

INRIA Bordeaux Sud-Ouest, Institut de Mathématiques de Bordeaux (IMB)

Research funding

The author acknowledges the French Research Agency ANR for its support to this research under grant no. ANR-17-CE08-0030.

Acknowledgements

This thesis was made possible by the trust reposed in me by my supervisor Mario, whom I also thank for the serenity, simplicity and quality of our exchanges.

I would like to thank my co-supervisor Gérard for his patience, meticulousness and for always being willing to help.

A huge thank you goes to Guillaume for being an important guide during the development of this thesis. I appreciated your genuine and fun disposition, as well as the dedication you put into your work and how you transmit it to others.

I thank the whole Cardamom team, for making the workplace so pleasant and in particular Sixtine, Elie and Mirco for always being a great support, for sharing joys and sorrows, but most of all for being good friends.

I would like to thank my lifelong friends, for always being close with their hearts no matter how far away they are.

I thank my family with all my heart:
Alberto, for being a strong and reassuring silent presence, for caring all my choices, for always being there to hold my hand out whenever things get rough and for being moved by my joys; my mother Tonia, my father Nico and my brother Andrea for always and constantly standing by me, for the perpetual support, and for the endless possibilities to which they have always opened me up.

Résumé en francais

Contexte

Les matériaux composites à matrice céramique (CMC) représentent une frontière très intéressante pour le développement technologique dans plusieurs domaines d'application et en particulier dans le secteur aérospatial. Leur résistance à de fortes charges mécaniques, à des températures très élevées et à des contraintes chimiques sévères en fait des candidats parfaits pour toutes les activités où l'adaptabilité à ces conditions extrêmes est un facteur crucial pour la durée de vie des composants. Les CMC surclassent les superalliages généralement utilisés dans le secteur aéronautique, car ils conservent leurs propriétés thermomécaniques à des températures de service plus élevées (supérieures à 1100 °C), ce qui permet aux moteurs d'être plus efficaces, et ils présentent une densité plus faible. L'augmentation du rendement des moteurs, associée à la réduction du poids, représente un point clé dans la réalisation de la réduction des émissions de gaz à effet de serre. En particulier, l'objectif fixé est d'atteindre des réductions de 90% et 75% des émissions de NO_x et de CO_2 respectivement par kilomètre et par passager d'ici 2050, conformément à ce qui a été initialement défini dans Vision 2020 [8] et AGAPE 2020 [74].

Sujet et motivations

La limitation de la durée de vie induite par l'oxydation constitue un problème majeur pour les CMC. Dans ce contexte, des CMC de type SiC/SiC ont été développés, présentant une résistance élevée à l'oxydation et ne présentant aucune différence de coefficient d'expansion thermique entre les fibres et les matrices. Ces matériaux sont constitués d'un renforcement fibreux en SiC et sont intégrés dans une matrice en SiC qui est obtenue par infiltration chimique en phase vapeur (CVI) et/ou par infiltration à l'état fondu (MI). En outre, une fine couche d'interphase est placée autour des fibres afin de garantir une amélioration de la résistance mécanique. En ce qui concerne l'architecture, les CMC présentent des paquets de fibres tissés les uns avec les autres afin d'obtenir des caractéristiques de continuité et de résistance. Le produit qui en résulte est un complexe tissu topologique tridimensionnel. La structure complexe et les propriétés chimiques/mécaniques des constituants des CMCs résultent en un matériau hautement

hétérogène et poreux qui nécessite une étude précise à différentes échelles. Dans cette thèse, nous ne ferons référence qu'à l'échelle des constituants d'un fil. L'objet de cette étude est donc les composites unidirectionnels et en particulier les mini-composites. Les CMC SiC/SiC et $SiC/[Si-B-C]$ étant des composites inverses (c'est-à-dire que l'allongement à la rupture de la matrice est inférieur à celui des fibres), ils peuvent présenter un comportement pseudo-ductile alors qu'ils sont constitués d'éléments fragiles. Ces excellentes propriétés mécaniques sont obtenues en présence d'interphases sur mesure qui dévient les fissures long des fibres [10, 24, 32], conférant une certaine pseudo-plasticité au matériau malgré qu'il soit constitué de composants fragiles. Initialement, la fissure affecte la matrice et ensuite se propage, sous l'action d'une certaine charge, vers certaines fibres en provoquant des dégradations ou des ruptures. Ces fissures à l'intérieur du matériau permettent la diffusion de l'oxygène, qui peut atteindre les fibres et causer leur oxydation. Les propriétés des fissures et leur distribution dans le matériau sont fonction de la nature et de l'intensité de la liaison entre la fibre et la matrice et de la charge appliquée. En particulier, un matériau présentant une faible densité de microfissures sera caractérisé par une forte contrainte de cisaillement entre les fibres et la matrice. Une solution a donc été proposée en introduisant à l'intérieur ou à l'extérieur de la matrice des éléments capables de produire de plus grandes quantités d'oxyde à basse température. Les composites avec ces éléments additionnels, appelés composites à matrice céramique autocicatrisante (SH-CMC), doivent satisfaire plusieurs conditions : [47]. Ils doivent être capables de guérir la fissure grâce à un oxyde qui isole l'interphase et les fibres, et ils doivent être chimiquement et mécaniquement compatibles avec les autres constituants. Cependant, dans la pratique, étant donné qu'il n'existe pas encore de matériau possédant toutes les propriétés susmentionnées, un système multicouche est adopté afin de tirer parti des différentes propriétés physiques et chimiques. Plusieurs systèmes multicouches ont été étudiés dans la littérature.

Dans cette thèse, un système à matrice alternée de couches de B_4C et de SiC est considéré. Concernant ce système, plusieurs études [28, 29] ont montré que sa résistance à l'oxydation dépend des proportions de SiC et de B_4C et de l'homogénéité du mélange de poudre. Ainsi, une bonne protection contre l'oxydation est garantie pour des températures comprises entre 800°C et 1400°C par la formation d'une couche uniforme de borosilicate jusqu'à 10 heures. En raison de la longue durée de vie de ces matériaux, la réalisation de campagnes expérimentales est onéreuse et nécessite un temps considérable. En conséquence, la modélisation numérique est un outil complémentaire particulièrement nécessaire. Cependant, la difficulté de décrire le comportement de ces matériaux est liée à la résolution d'un problème multi-physique complexe représentant l'évolution

spatio-temporelle des phénomènes physico-chimiques qui se produisent tels que la diffusion de l'oxygène à travers la fissure, l'évolution des espèces chimiques produites et consommées pendant l'oxydation, et la dégradation des fibres. Bien que plusieurs travaux aient traité de modèles complexes décrivant la mécanique de la rupture des CMCs [36, 57, 66], les défis mentionnés ci-dessus ont conduit de nombreux auteurs à utiliser des hypothèses simplificatrices. En particulier, certains travaux antérieurs décrivant le comportement du processus de cicatrisation des fissures s'appuient sur des approximations 0D [2, 15, 40] ou 1D [85] simplifiées, donnant des valeurs de la concentration en oxygène en des points stratégiques du matériau. Cela présente l'avantage de permettre de résoudre le problème avec une méthode analytique ou semi-analytique, mais certaines information sur le processus complet sont perdues. Pour éviter cette perte, le travail [81] a décrit le processus de cicatrisation d'une fissure, en privilégiant la description de la propagation de l'oxyde mais en nécessitant un temps de calcul onéreux.

Dans ce contexte, la présente thèse se propose de rendre le modèle multiphysique et multidimensionnel le plus traitable possible grâce à des choix d'intégration numérique appropriés suite à une étude approfondie des phénoménologies se manifestant dans la fissure. En effet, la modélisation bidimensionnelle de la fissure à partir d'images permet de connaître et d'analyser l'évolution des variables d'intérêt dans l'espace, de comprendre comment l'oxygène diffuse dans la fissure, comment il est lié à l'oxydation des couches réactives de la matrice et l'effet de l'oxyde dans le temps. En obtenant le champ physico-chimique détaillé de cette manière, il est raisonnable de se poser la question de sa relation avec les mécanismes d'oxydation et de dégradation des fibres dans le mini-composite. En particulier, une telle description permet de construire un modèle explicitement dépendant des conditions environnementales qui prend en entrée les variables obtenues à partir du champ de variables physico-chimiques calculé dans la fissure. En implémentant un modèle mécanique approprié, il serait également possible d'étudier les variations de la durée de vie du mini-composite non seulement en fonction des paramètres environnementaux (qui sont explicites dans tous les modèles impliqués) et des conditions de charge, mais également en fonction des paramètres géométriques et de forme. La description bidimensionnelle permet par ailleurs de prendre en compte l'influence de la distribution spatiale des résistances des fibres, ce qui rend possible la description d'un scénario de rupture complet du mini-composite en fonction de ces valeurs.

La présente thèse a été développée dans cette perspective, fixant comme objectif le développement d'un modèle numérique fiable et validé, capable de reproduire le plus finement possible le comportement du mini-composite CMC auto-cicatrisant.

Travail effectué

Cette thèse se propose d'évaluer et d'analyser la durée de vie d'un mini-composite SH-CMC dans une atmosphère oxydante sous une charge de tension. Elle est essentiellement structurée en deux parties : dans la première partie, est présenté le modèle qui a été réalisé et utilisé afin de calculer la durée de vie du mini-composite considéré, présentant dans chaque chapitre les éléments fondamentaux du modèle. Le chapitre 2 présente la modélisation des processus diffusifs-réactifs moyennés sur la fissure transversale. En particulier, ce modèle permet de coupler la diffusion de l'oxygène à travers la fissure et l'évolution des espèces chimiques produites et consommées pendant l'oxydation. Ce modèle bidimensionnel basé sur l'image, précédemment introduit dans [81], a été ici l'objet d'une étude de la forme adimensionnelle de l'EDP associée. L'analyse permet de comprendre pleinement la contribution de chaque terme, et d'effectuer les choix de discrétisation les plus appropriés en termes de conditions aux limites, et d'intégration temporelle, rendant le modèle considérablement plus rapide d'un point de vue computationnel. Les résultats obtenus en termes de diffusion de l'oxygène, d'oxydation des couches réactives de la matrice et de cicatrisation des fissures sont présentés, en mettant en évidence leur évolution dans l'espace. Dans le chapitre 3, une présentation des principaux mécanismes de dégradation associés aux fibres Hi-Nicalon est donnée, avec un focus particulier sur le phénomène de propagation sous-critique de défauts. Un modèle de propagation progressive des défauts inspiré de celui proposé dans [56] est ici présenté. Ce modèle est utilisé pour prédire la dégradation progressive des fibres en tenant compte des paramètres environnementaux, notamment la concentration en oxygène, en considérant sa variation extrême à travers la fissure. En particulier, une solution analytique a été dérivée pour ce modèle, ce qui a permis de le calibrer et de comparer les solutions obtenues avec les données expérimentales et le modèle numérique. Enfin, afin d'évaluer sa stabilité et l'influence des paramètres présents, une analyse de sensibilité a été réalisée. Le chapitre 4 est enfin consacré à la présentation du modèle mécanique utilisé et de la stratégie de calcul de la durée de vie du mini-composite SH-CMC analysé. La prédiction de la rupture du mini-composite dépend de la résistance initiale statistique des fibres, de l'évolution des mécanismes d'oxydation et de cicatrisation dans la fissure, de la cinétique de propagation progressive des défauts et de la répartition de la charge après la rupture des fibres. Plus précisément, la durée de vie a été analysée en termes de variations de température, de contrainte appliquée et de distribution statistique de la résistance des fibres, ce qui permet d'avoir une vision approfondie du scénario de rupture en fonction du temps et de la classification du comportement du matériau.

La deuxième partie est consacrée à l'évaluation et à la quantification de l'influence de différents paramètres (topologiques, géométriques, dimensionnels) sur la durée de vie du mini-composite. Plus précisément, la description bidimensionnelle de la fissure dans le mini-composite permet d'analyser l'influence des paramètres géométriques, topologiques et de taille sur la durée de vie. Par conséquent, dans le chapitre 5 sont présentées diverses configurations de fils virtuels, obtenues en faisant varier le nombre de fibres et la forme du fil, pour lesquelles les durées de vie ont été calculées. L'influence de ces paramètres a ensuite été évaluée, permettant de définir des facteurs d'échelle et de forme pour différentes conditions de charge et de température. La compréhension de cette influence a conduit à une stratégie d'estimation de la durée de vie des mini-composites de différentes formes et de différents nombres de fibres impliquant uniquement ces facteurs. Considérant que le problème ainsi décrit est naturellement dispersé, une étude de convergence a également été présentée dans ce chapitre afin de prendre en compte le bon degré de dispersion des résultats obtenus en termes de durée de vie. Afin d'évaluer rigoureusement l'influence des facteurs considérés dans la prédiction de la durée de vie du mini-composite, une étude d'incertitude combinée à une analyse de sensibilité de ces paramètres est présentée au chapitre 6. En particulier, un métamodèle basé sur l'Expansion en Chaos Polynomial (PCE) a été construit pour reproduire le modèle multi-physique adopté pour le calcul de la durée de vie du mini-composite et a permis d'analyser comment les paramètres d'entrée se propagent pour générer une variation des quantités de sortie. Cette démarche a permis de mettre en évidence les paramètres ayant une influence appréciable dans un scénario le plus général possible. Les effets de la distribution spatiale des fibres dans le mini-composite ont ensuite été mis en évidence et quantifiés par la construction d'un métamodèle dans des conditions environnementales fixes. Le résultat intéressant de cette étude réside dans le fait qu'une variation spatiale des paramètres les plus influents a été trouvée lorsque la géométrie du mini-composite a changé, mettant en évidence un mécanisme et un scénario de rupture différents.

Don't judge each day by the harvest you reap
but by the seeds that you plant.

Robert Louis Stevenson

Contents

Chapter 1

Introduction

1.1 Context and motivation

Ceramic matrix composite (CMC) materials represent a promising frontier in technological development in many application domains and in particular in the aerospace sector. Their ability to withstand heavy mechanical loads, very high temperatures and severe chemical stress makes them perfect candidates for all those activities where adaptability to such demanding conditions is a crucial factor for the lifetime of the components. CMCs outcompete the super alloys generally used in the aeronautical sector, as they maintain their thermomechanical properties [51] at higher operating temperatures (greater than 1100 °C), allowing engines to be more efficient, and as they have a lower density. The increase in engine efficiency together with weight reduction represents a key point in the achievement of greenhouse gas emission reduction. In particular, the target set is to achieve 90% and 75% reductions of NO_x and CO_2 emissions respectively per kilometre and per passenger by 2050, as originally defined in Vision 2020 [8] and AGAPE 2020 [74]. For instance, SiC/SiC CMCs were introduced to be deployed in the high-pressure turbine of the Leading Edge Aviation Propulsion (LEAP) engine (see Fig. 1.1) for the Airbus A320 NEO. Furthermore, on January 2020, the GE9X engine in which the combustion chamber liner, shutters, and vanes were made of SiC/SiC CMCs, had its first flight on the Boeing 777 [94].

A major problem for CMCs is the oxidation-induced lifetime limitation. The first CMCs developed are of the C/C type [91]. Composites of this type exhibit very good thermomechanical properties at high temperatures (2000 °C) as they dissipate large amounts of incident thermal energy before being consumed. This resistance to ablation has led to their use in applications such as heat shields and nozzle diverters. They also exhibit excellent dimensional stability as they have a low coefficient of expansion. This is

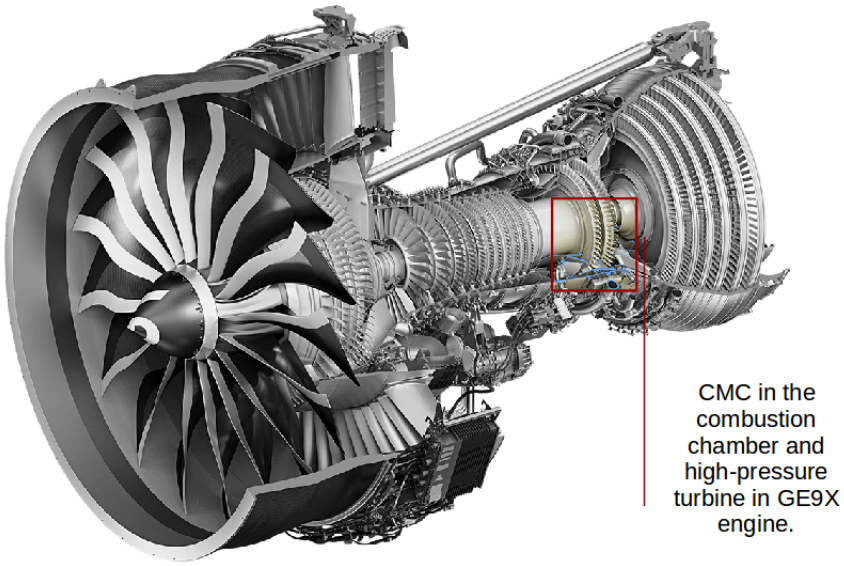

Figure 1.1: CMCs in the high-bypass turbofan in Leading Edge Aviation Propulsion (LEAP).

why they are considered for high-temperature aircraft turbine parts, since in these engines the atmosphere is highly oxidative. The main problem with C/C-type CMCs is that they oxidise as early as 400 °C. For this reason, CMCs of the C_f $/SiC_m$ type, and subsequently SiC/SiC, have been developed. The latter perform better because the fibres are more resistant to oxidation and there is no difference in the thermal expansion coefficient between fibres and matrices. These materials consist of SiC fibrous reinforcement and are immersed in a SiC matrix that can be obtained by chemical vapour infiltration (CVI) and/or melt infiltration (MI). In particular, composites consisting of a SiC matrix obtained by CVI are porous (5-15%), (Si+SiC) obtained by MI processes are more dense [51]. In addition, a thin layer of interphase is placed around the fibres in order to guarantee improved mechanical resistance. Actually, the interphase plays the crucial role of deflecting the matrix cracks [10, 24, 32], conferring a certain pseudo-plasticity to the material despite being constituted by brittle components. Currently used interphase materials are pyrocarbon (pyC) or hexagonal boron nitride (hex-BN). The use of the latter gives the SiC/SiC composite a good resistance to oxidation in a dry environment for moderate temperatures (about 600°C) [64, 76]. Actually, the oxidation of BN results in the production of a liquid oxide (B_2O_3) starting at 460°C. In addition, silica is formed by the oxidation of SiC from the 900°C [46]. Although the latter reaction produces silica which may have the ability to create a seal in the formed micro-crack, it is not efficient below 1100°C.

Regarding the architecture, CMCs show bundles of fibres interwoven with each other in order to obtain characteristics of continuity and resistance. The resulting product is an

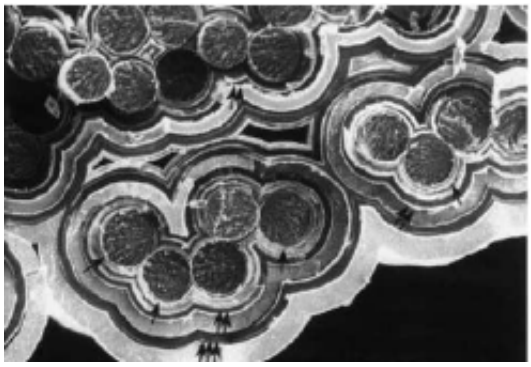

Figure 1.2: Transversal section of a multi-layered SH-CMC mini-composite [86].

elaborate three-dimensional topological network. The complex structure and the chemical/mechanical properties of the CMCs constituents results in a highly heterogeneous and porous material that requires accurate investigation at different scales. In particular, the *micro-scale* (see Fig. 1.3(a)) is defined as the scale of the elementary constituents and ranges from one to several micrometres. At the *meso-scale* (see Fig. 1.3(b)), the composite material is seen as a set of yarns and therefore the representative scale is that of the section of the yarn, i.e. some millimetres. Finally, the scale of the whole part is known as *macro-scale* (see Fig. 1.3(c)) and, according to the part considered, its size can be a few centimetres or decimetres.

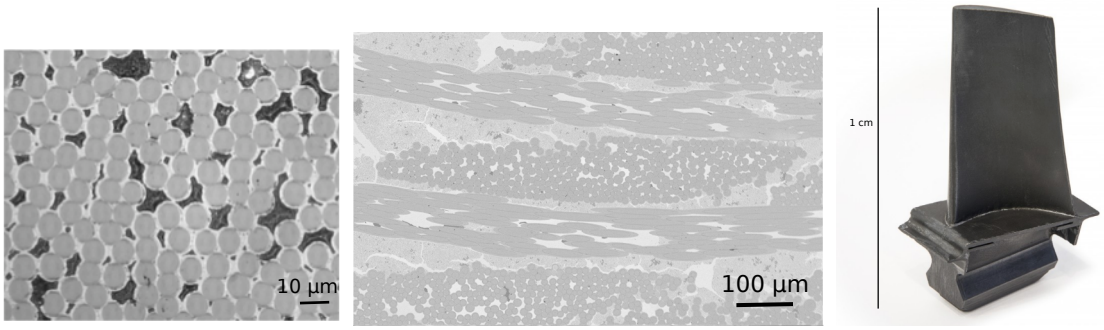

(a) microscopic scale (b) mesoscopic scale (c) macroscopic scale

Figure 1.3: Different scales for CMCs.

In this thesis, we will consider the constituent scale of a yarn. The object of this study is therefore unidirectional composites and in particular mini-composites.
Generally, we refer to two types of unidirectional models of composite materials: micro-composites and mini-composites [77].
Micro-composites, such as the one represented in Fig. 1.4, consist of a single fibre surrounded by an elementary sequence of matrix layers and are therefore also known as *single fibre composites*. They allow a remarkably in-depth study but are complex to

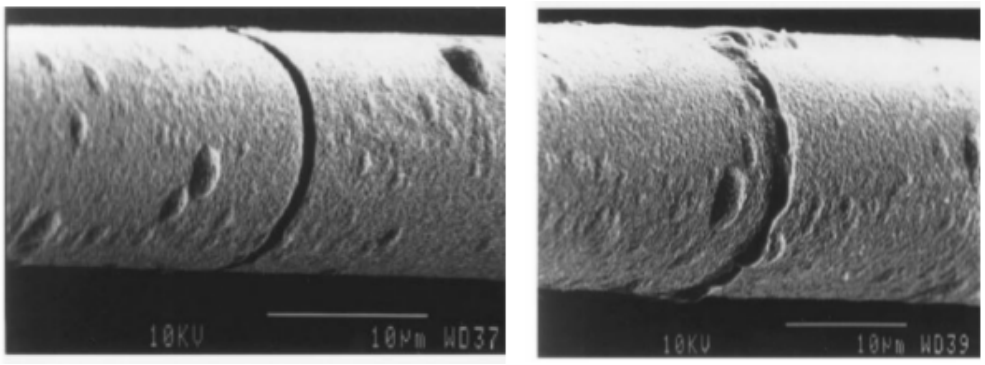

Figure 1.4: Micro-composite with a matrix crack formed after a fatigue test (left) and filled with healing oxide after aging under tension (right) [77].

fabricate.

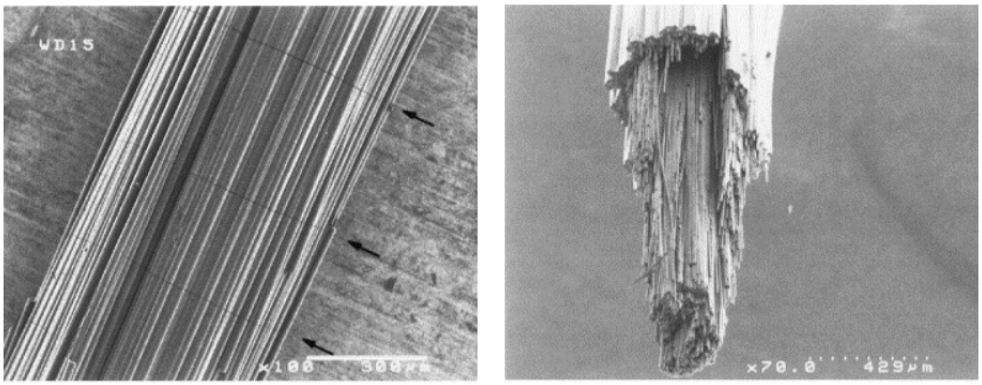

Figure 1.5: Multiple matrix microcracking (left) and failure surface (right) of C/C mini-composites [77].

On the other hand, mini-composites consist of bundle of fibres immersed in the reference matrix and are easier to produce than micro-composite. Essentially, the mini-composite corresponds to the yarn that constitutes the composite material. A representation of a mini-composite is given in Fig. 1.5. The investigation of mini-composites provides a more complete understanding of the failure mechanisms that occur in the yarn subsequent to the interaction between multiple fibres. The introduction of these models has enabled a more in-depth study of phenomena such as the transverse cracking of yarns [67], fibre/matrix decohesion [11, 75, 87] and the self-healing mechanism [2, 15, 40, 61]. Since SiC/SiC and $SiC/[Si-B-C]$ CMCs are inverse composites (i.e. the failure strain of the matrix is lower than that of the fibres), they may exhibit a pseudo-ductile behaviour even though they consist of brittle elements. These excellent mechanical properties are obtained in presence of tailored interphases that deflect cracks along the fibres. Initially, the crack affects the matrix and then propagates, under the action of a certain load, to some fibres causing damage or breakage. These cracks inside the material allow the

diffusion of oxygen, which can reach the fibres and cause their oxidation. The properties of the cracks and their distribution in the volume of the material are a function of the nature and intensity of the bonding between the fibre and matrix and the applied load. In particular, a material with a low density of micro-cracks will be characterised by high shear stress between the fibres and the matrix.

Therefore, a solution has been proposed by introducing into or outside the matrix elements capable of producing larger amounts of condensed oxide through oxidation at lower temperatures. These additional elements in such composites, called Self-Healing Ceramic Matrix Composites (SH-CMCs), must satisfy several requirements [47]. They should be able to heal the crack through an oxide which isolates the interphase and the fibres, and they should be chemically and mechanically compatible with the other constituents. However, in practice, since a material with all the above properties does not yet exist, a multi-layer system is adopted in order to take advantage of different physical and chemical properties (see Fig. 1.2). Several multi-layer systems have been investigated in the literature. In particular, a family of self-healing matrices were developed by Snecma Propulsion Solide and employed in the production of two materials named CERASEP®A410 and CERASEP®A40C [4]. Manufactured using CVI, they consist of multiple sequences of the $Si - B - C$ system.

In this thesis, a system whose matrix layers of B_4C and SiC are alternating is considered. Regarding this system, several studies [28, 29] have shown that its oxidation resistance depends on the proportions of SiC and B_4C and on the homogeneity of the powder mixture. Hence, good protection against oxidation is guaranteed for temperatures between 800°C and 1400°C by the formation of a uniform borosilicate layer for up to 10 hours. Nevertheless, in humid atmospheres, the protection guaranteed by this system is almost non-existent for temperatures between 700°C and 1000°C [50].

Due to the long lifetime of these materials, conducting experimental campaigns is expensive and time-consuming, and numerical modelling is a particularly needed complementary tool. However, the difficulty in describing the behaviour of such materials is related to the resolution of a complex multi-physical problem representing the space-time evolution of physico-chemical phenomena that occur such as the oxygen diffusion through the crack, the evolution of the chemical species produced and consumed during oxidation, and the degradation of the fibres. The first works dealing with CMCs concerned unidirectional CMCs [7, 18, 72] and successively woven CMCs [43, 55]. The first applications of CMCs concerned, in particular, C/C [36] considering applications with short operating times, describing the mechanical behaviour of pieces until failure. A subsequent evolution of this model was then proposed in [54, 57] thanks to the anisotropic

damage theory presented in [52]. Similar approaches have been proposed for CMCs in the literature [10, 12, 13, 66, 68, 69] while keeping the mechanics of damage as the modelling framework. The problem of the lifetimes associated with SH-CMCs appears in [2, 15, 65], where microscopic models were introduced into the macroscopic model to describe the oxide-protective effects in cracks. However, although these works have dealt with complex models describing the failure mechanics of CMCs, regarding the coupling with the environmental condition, the challenges of dealing with an elaborate multi-physics model have led many authors to use many simplifying assumptions. In particular, the previous works describing the behaviour of the crack healing process rely on simplified 0D [2, 15, 40] or 1D [85] approximations, providing values of the oxygen concentration in strategic points of the material. This has the benefit of allowing to solve the problem with some analytical or semi-analytical technique, but some information about the complete process is lost. To mitigate this loss, the work [81] described the self-healing process in a crack, focusing on the description of the oxide spreading but requiring an onerous computational time.

For this purpose, the present thesis aims at making the multi-dimensional and multi-physics model as tractable as possible through appropriate numerical integration choices resulting from an in-depth study of the phenomenologies occurring in the crack. Indeed, the two-dimensional image-based crack modelling allows knowledge and analysis of how the variables of interest evolve in space, comprehension of how oxygen diffuses within the crack, how it relates to the oxidation of the reactive matrix layers and the effect of the protective oxide over time. Obtaining the detailed physico-chemical field in this way, it is reasonable to wonder about how it is related to the mechanisms of oxidation and degradation of the fibres in the mini-composite. In particular, such a description allows implementation of a model explicitly dependent on environmental conditions that takes as input the variables obtained from the physico-chemical variable field calculated in the crack. By implementing an appropriate mechanical model, it would also be possible to study variations in the lifetime of the mini-composite not only depending on environmental parameters (which are explicit in all the involved models) and loading condition but also on geometrical and shape parameters. The two-dimensional description of the involved processes also allows the influence of the spatial distribution of the fibre strengths to be taken into account, enabling a complete failure scenario of the mini-composite to be painted in dependence on these values.

The present thesis was developed with these purposes, setting as its objective the development of a reliable, validated numerical model able to reproduce the self-healing CMC mini-composite behaviour in as much detail as possible.

1.2 Outline of the manuscript

This thesis aims to evaluate and analyse the lifetime of an SH-CMC mini-composite in an oxidising atmosphere under a tension load. It is basically structured in two parts: in the first part, the implemented model used in order to calculate the lifetime of the considered mini-composite is presented, highlighting the fundamental building blocks of the model in each chapter.

- **Chapter 2** presents the section averaged approximation for the diffusive-reactive processes in the transverse crack. In particular, this model allows the coupling of the oxygen diffusion through the crack and the evolution of the chemical species produced and consumed during oxidation. This two-dimensional image-based model, previously introduced in [81], was here subjected to a study of the dimensionless form of the associated PDE. The analysis allows to fully understand the contribution of each term, and perform the most appropriate discretisation choices in terms of boundary conditions, and time integration, making the model much faster from a computational point of view. The results obtained in terms of oxygen diffusion, oxidation of the reactive matrix layers, and crack healing are presented, highlighting how they evolve in space and their correlation.

- Subsequently, **Chapter 3** presents an overview of the main degradation mechanisms associated with Hi-Nicalon fibres, with a particular focus on the phenomenon of sub-critical defect propagation. A slow crack growth model inspired by the one proposed in [56] is here presented. This model is used to predict the fibres progressive degradation taking into account the environmental parameters, especially the oxygen concentration, considering its extreme variation through the crack. In particular, an analytical solution was derived for this model, which allowed it to be calibrated and the obtained solutions to be compared with experimental data and the numerical model. In addition, in order to assess its stability and the influence of the considered parameters, a sensitivity analysis was carried on.

- **Chapter 4** is finally devoted to the presentation of the mechanical model used and the strategy for calculating the lifetime of the analysed SH-CMC mini-composite. The tow failure prediction depends on the statistical fibres initial strength, the evolution of oxidative and healing mechanics in the crack, slow crack growth kinetics, and load sharing following fibres breakage. Specifically, the lifetime was analysed in terms of temperature variations, applied stress and statistical distribution of fibres strength, allowing an in-depth view of the failure scenario over

time and the classification of material behaviour.

The second part is devoted to the evaluation and quantification of the influence of various parameters (topological, geometrical, size) on the lifetime of the mini-composite:

- Specifically, the two-dimensional description of the crack in the mini-composite allows the influence of geometrical, topological and scaling parameters on lifetime to be analysed. Therefore, various virtual tow configurations are presented in **Chapter 5**, varying the number of fibres and the shape for which the respective lifetimes were calculated. The influence of these parameters was then evaluated, allowing scaling and shape factors to be defined for different load and temperature conditions. The understanding of this influence led to a strategy for estimating the lifetime of mini-composites with different shapes and number of fibres involving only these factors. Bearing in mind that the problem thus described is naturally scattered, a convergence study has also been presented in this chapter to take into account the proper degree of scattering of the obtained results in terms of lifetime.

- In order to formally evaluate the influence of the factors considered in the lifetime prediction of the mini-composite, an uncertainty study combined with a sensitivity analysis of these parameters is presented in **Chapter 6**. In particular, a PCE-based metamodel was built to reproduce the multi-physics model adopted for the calculation of the lifetime of the mini-composite and analysed how the input parameters propagate to generate a variation in the output. This made it possible to highlight the most influential parameters in the most general case possible. Subsequently, the effects of the spatial distribution of the fibres in the mini-composite were highlighted and quantified through the construction of a metamodel under fixed environmental conditions.

- Finally, the section **Conclusions and perspectives** reviews and discuss the most relevant findings and results obtained and presented throughout this thesis with a view to the original objectives set and to the future research prospects.

1.3 Dissertation activities

Most of the work presented in this thesis has been the subject of public presentations at international level.

- In particular, the numerical model implemented to calculate the lifetime of the mini-composite and the numerical strategy adopted were the subject of the talk **"Healing process modelling and lifetime evaluation for self-healing ceramic matrix composites"** during SIAM Conference on Mathematical Aspects of Materials Science - SIAM-MS21, May 17-28, 2021, Bilbao, Spain, web.

- Furthermore, the results concerning the lifetime of the mini-composite under different loading conditions, temperature and spatial variation of the fibre strength distribution were presented in the talk **"A two-dimensional numerical strategy for computing self-healing ceramic matrix composites lifetime"** during 8th ECCOMAS Thematic Conference on the Mechanical Response of Composites - COMPOSITES 2021, September 22-24, 2021, Gothenburg, Sweden, web.

- In addition, a poster entitled **"Image-based lifetime evaluation of self-healing CMCs"** was presented during the 4th winter school held by LabEx tec21 in Grenoble (January 26-31, 2020).

Furthermore, the work of this thesis allowed the achievement of the following scientific contributions:

- the publication of the article **"A 2D image-based multiphysics model for lifetime evaluation and failure scenario analysis of self-healing ceramic-matrix mini-composites under a tensile load"** in the Journal of the European Ceramic Society.

- an article about the analysis of parameters variability on the lifetime of the mini-composite associated with the uncertainty quantification analysis, **"Sensitivity analysis of SH-CMC mini-composite lifetime on its geometric, topological and environmental characteristics"**, is ongoing and will be submitted soon.

Chapter 2

2D crack-average model for SH-CMCs

Contents

2.1 Introduction

The lifetime modeling of healing matrix composites requires the description and characterisation of the phenomena that occur at the microscale as a consequence of crack network development, such as transport of species through them and oxidation or production of other chemical species within them. For this reason, the first part of the chapter is devoted to the description of the crack-averaged scheme coupling the PDEs and ODEs system used to model oxygen diffusion through the crack and the evolution of the chemical species produced and consumed during oxidation. A complete study of the dimensionless form of the equations is presented and the variational formulation in the weak form of the whole system is expressed in the second part of the chapter. The proposed analysis allowed us to fully understand the contribution of each term, make strategic choices from the computational time point of view by setting an adaptative integration time and perform the most appropriate choices in terms of boundary conditions understanding their influence on the model. Finally, the last part of the chapter is consecrated to show the capabilities of the presented model.

2.2 Matrix cracking scenario for CMCs

There are different mechanisms of microcracking in CMCs, but the key phenomenon is the deflection of the crack first formed in the matrix towards the fibre/matrix interphase [10, 24, 32]. This mechanism confers a certain pseudo ductility to the material even though its components are brittle, ensuring the protection of the fibres and the development of a network of cracks. The density and the opening of these micro-cracks depend on the applied load and the architecture of the fibres as well as on the strength of the interphase bond (see Fig. 2.1).

In particular, a strong bond results in a certain brittleness of the material, which leads to failure without multiple crack formation. On the contrary, a bond which is too weak results in a large deformation and low ultimate tensile strength [86]. Indeed, the interphase, has an important role on the global mechanical behaviour of the material. It has several functions. First of all, it has the task of deflecting the cracks initially formed in the matrix to prevent them from propagating into the fibres. As the interphase has two interfaces, i.e. interphase/matrix and interphase/fibre, the deviation can occur either along one of these two interfaces which is referred to as adhesive fracture, or the deviation can occur within the interphase itself. The latter mode is known as cohesive rupture [78]. In addition, the interphase has to enable the load transfer from the matrix to the fibres,

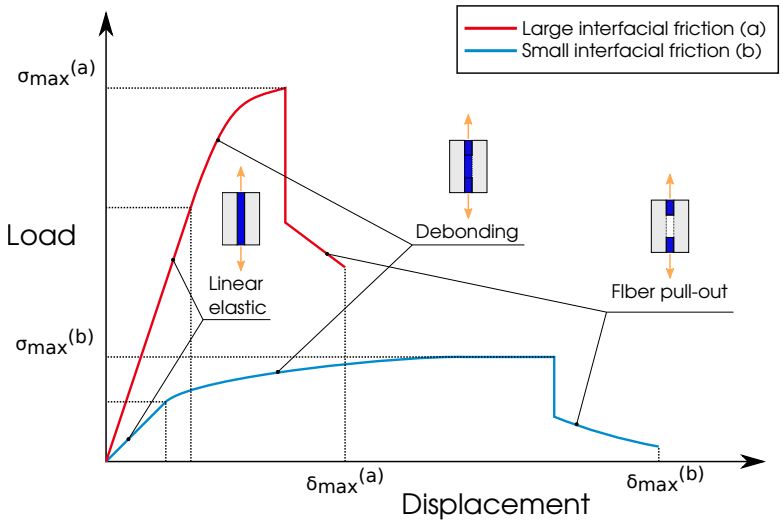

Figure 2.1: Load-displacement behavior in tensile test considering strong and weak interphase bond based on [93].

which is what gives the material its pseudo-plastic (damageable) behaviour. In addition, the interphase may help limiting the local stresses resulting from thermal residual deformations due to different values of thermal expansion coefficients between fibre and matrix. A good interphase material is chosen by making a compromise in achieving the above properties.

The morphology of the cracks scenario is well known [89]. Mainly two types of cracks can be identified in the material: inter-yarns cracks and intra-yarns cracks. The inter-yarns cracks occur first as the matrix in these areas is stiffer (and therefore more brittle) containing generally larger pores. These cracks develop orthogonally to the main load direction. As the material reaches the cracks network saturation, new cracks are formed in the matrix inside the yarns. Assuming a longitudinal load, the intra-yarns cracks are orthogonal to the longitudinal fibre bundles and parallel to the transverse fibre bundles. A typical illustration is shown in Fig. 2.2.

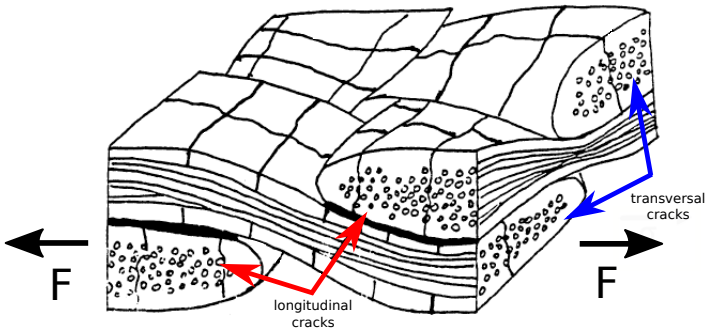

Figure 2.2: Transversal and longitudinal cracks in woven CMC.

This last type of cracks is crucial because oxygen can diffuse through them, reaching the

fibres and causing their sub-critical crack growth. In addition, further degradation occurs when, as a result of oxygen diffusion through the crack, an oxide that fills the space between the fibre and the matrix is formed, causing an excessive reinforcement of the shear stress and the consequent local weakening of the material. For this reason, this thesis focuses the attention on the description of the effects caused by an oxidising environment in transverse cracks. For this purpose, self-healing matrices have been developed to ensure extremely long service lifetimes [14, 15] minimising oxgen diffusion in the material as much as possible to avoid its degradation and the consequent rapid failure [49]. SH-CMCs (Self-Healing CMCs) contain layers of reactive matrix added to take advantage of the passive action of the oxide produced to seal the crack. As a result, oxygen diffusion is reduced [41], and the fibres are protected from excessive oxidation.

2.3 Self-healing process

The general oxidation process implies a change in mass Δm in time which is closely related to the oxidation rate k by means of a coefficient n that defines its behavior:

$$\Delta m = k \cdot t^n \tag{2.1}$$

Notably, this relation has as limit the range of values that can assume n $\in]0.5 - 1[$ [86]. For values of n that do not fall within this range, a simple analytical model describing the oxidation process does not exist [86]. As regards ceramic materials, the oxidation mechanism produces a layer of protective oxides and gaseous species. In the case of a growing protective solid oxide scale, the law governing this type of oxidation is parabolic and is shaped as follows:

$$e^2 = k_p \cdot t \tag{2.2}$$

where k_p represents the parabolic rate constant, e is the thickness of the oxide scale generated and t the time. The quantification of the oxide production, and therefore of the reaction rate of the considered material, is a relevant aspect. In fact, the scale strongly limits the diffusion of oxidizing gaseous species and, at the same time, the consumption of the material. It is worth to notice that the parabolic rate constant depends on the diffusion coefficient of the oxidizing species through the oxide layer D_{ox}, which is a function of the nature of the oxide as well as its degree of crystallization and its composition, according to the following equation:

$$k_p = \frac{2D_{ox}C_{ox}}{N} \tag{2.3}$$

where N is the number of moles of the oxidizing species incorporated into the oxide. On the other hand, an order 1 kinetic law (linear rate law) is obtained when the reaction product is gaseous or at least so porous that it does not bring limitation to diffusion towards the reaction surface :

$$\frac{dh}{dt} = -k_l \tag{2.4}$$

where $\frac{dh}{dt}$ represents the surface recession rate and k_l is a linear reaction rate constant $(m.s^{-1})$.
Linear kinetics occurs in several cases :

- active oxidation, ie. oxidation yielding a non-protective product like carbon oxidation :

$$C_{(s)} + O_{2(g)} \quad \rightleftharpoons \quad CO_{2(g)} \tag{2.5}$$

- water vapor corrosion, turning a solid into gaseous hydroxide, like for example :

$$SiO_{2(l/s)} + 2H_2O_{(g)} \quad \rightleftharpoons \quad Si(OH)_{4(g)} \tag{2.6}$$

In the latter case, competition between oxide creation and oxide volatilization exists. At the material level, it occurs that while the oxide layer grows over time until its oxidation rate decreases according to the previously mentioned model, while the volatilisation rate remains constant. For this reason a characteristic time $t^\star$ at which the two reaction rates, i.e. oxidation and volatilisation, are equal exists. At this point the stable recession phase of the material begins, and it is characterised by a linear loss of mass over time as shown in Fig. 2.3.
The latter situation will not be fully treated in the present work, though the developed numerical tools and approaches are capable of addressing it.

2.4 The constituents of the studied material

The investigated mini-composite is made up of Hi-Nicalon fibres surrounded by a pyrocarbon (pyC) interfacial coating and immersed in a multi-layered matrix [41, 62] as represented in Fig. 2.4. The matrix includes concentric layers of SiC and B_4C deposited

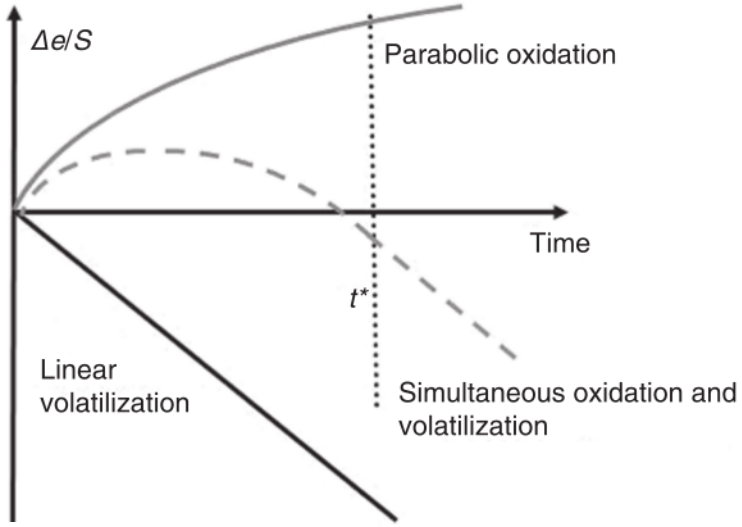

Figure 2.3: Para-linear kinetics oxidation [86].

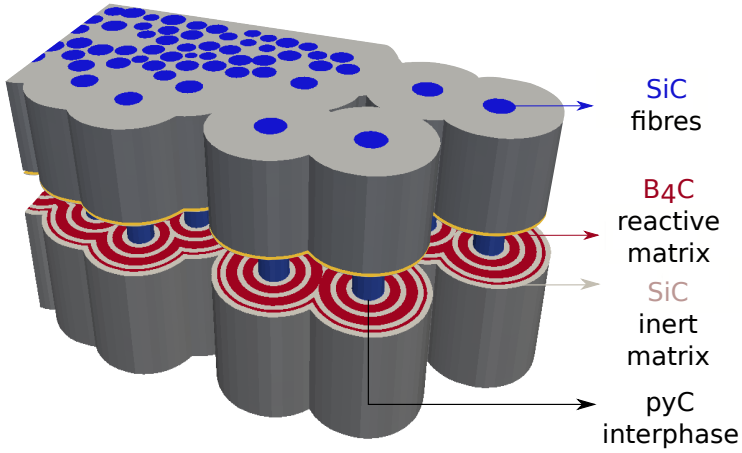

Figure 2.4: Minicomposite elementary consituents: fibres and matrix layers materials.

via CVI. The sequence of these matrix layers gives the "self-healing" character to the material. In particular, the introduction of reactive matrix layers protects the pyC interphase placed around the fibres from oxidation up to 1400°C. The B_4C layers oxidation consumes part of the oxygen and the microcrack is sealed with a B_2O_3 liquid oxide (also called boria glass) above 450°C. This process creates a barrier to the diffusion of oxygen in the crack [41]. The boria glass, in contact with silicon-containing species like SiC or Si_xB_yC, is capable of partially dissolving Si atoms, turning itself into a borosilicate (B_2O_3 — SiO_2) glass. On the other hand, the reactivity of crystallized SiC

being low at intermediate temperatures (treated in this work), and therefore in the self-healing process, only B_2O_3 oxide is considered. A complete description of the material morphology and the reaction kinetics are reported in this section.

2.4.1 Hi-Nicalon fibres

The fibres constitute the reinforcing material of the composite, hence they must exhibit high mechanical properties, be well embedded between the interphase and the matrix and show an appropriate resistance to environmental conditions. The investigated material is composed of SiC Hi-Nicalon type fibres, which are generally grouped as yarns (each one containing 500 fibres), woven in order to obtain the fibrous preform. The fibres belonging to this generation, i.e. fibres of the Nicalon and Hi-Nicalon type, have good mechanical strength, providing good stiffness and high strength even at high temperatures.

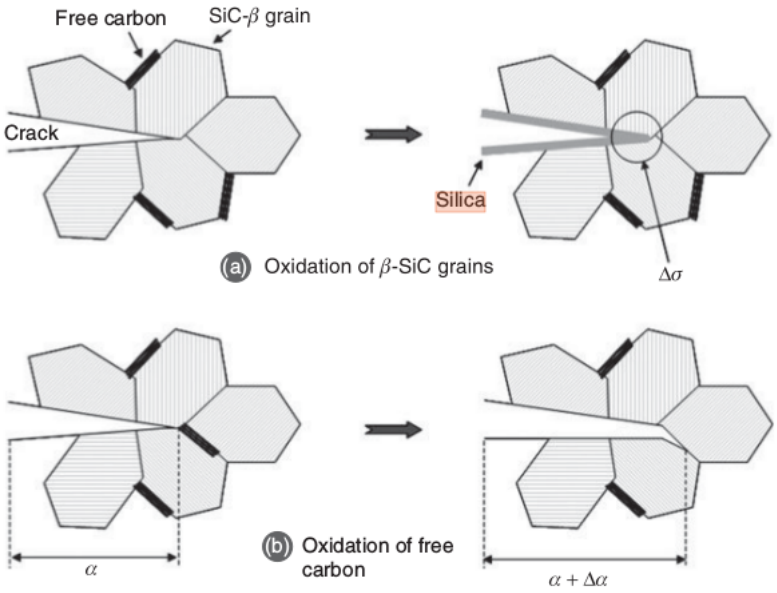

Figure 2.5: Schematic representation of the slow crack growth mechanism [39].

It has been demonstrated [38] that Hi-Nicalon-type fibres exposed in an oxidising environment are subject to the phenomenon of sub-critical crack propagation at intermediate temperatures (such as $T < 1000$ °C). Indeed, the delayed failure of SiC-based fibres is caused by the oxidation of free carbon at grain boundaries and SiC nanograins or silicon oxycarbide at crack tips [37], which in turn generates subcritical crack propagation of surface defect (see Fig. 2.5).
Furthermore, it has been shown that under these environmental conditions the oxidation of SiC-based fibres leads to the formation of a silica layer oxide [37] at the fibre surface

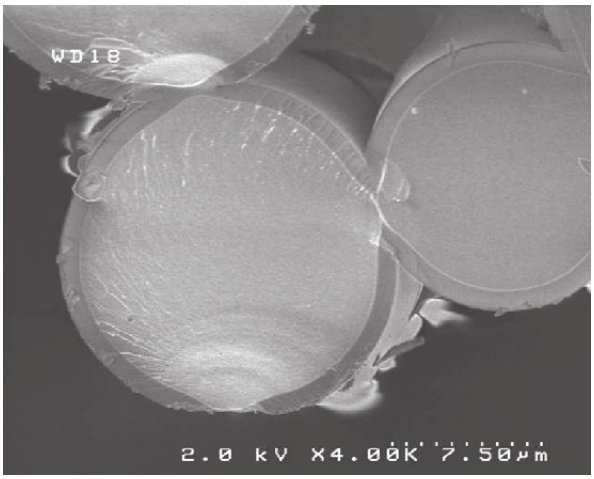

Figure 2.6: Slow crack growth and oxide layer in Hi-Nicalon fibres after static fatigue [58].

(see Fig. 2.6) according to the relation given below:

$$SiC_{(s)} + O_{2(g)} \quad \rightleftharpoons \quad SiO_{2(s)} \tag{2.7}$$

It should be noted, however, that the growth of silica layer is not responsible for fracture but acts as a barrier for the oxidising agent, which must first diffuse through this oxide layer before reaching the fibre surface.
A deeper analysis of the characteristics and performance of SiC-based fibres will be discussed in chapter 3.

2.4.2 SiC matrix layers

The SiC matrix form is crystallographically of β variety. It is a matrix made by CVI (Chemical Vapour Infiltration) process and is frequently used in CMC. Densification in liquid form is also possible but this procedure requires various heat treatments and impregnation of the fibrous preform with a pre-ceramic resin. When subjected to the environment, the SiC matrix can be considered inert up to 1000°C. However, as for all carbides, its oxidation can be passive or active according to the atmospheric pressure. In particular, in the case of SiC, oxidation is active when the partial pressure of oxygen is too low [92]. The transition temperature between passive and active oxidation of SiC depends on its microstructure, impurities and oxygen partial pressure. The oxidation process follows the relation

$$SiC_{(s)} + O_{2(g)} \quad \rightleftharpoons \quad SiO_{(g)} + CO_{(g)} \tag{2.8}$$

and causes a transport of $SiO_{(g)}$ and $CO_{(g)}$ and a loss of mass of the material. Conversely,

oxidation will be passive if the partial pressure of oxygen is greater than 100 Pa for temperatures in range 800 °C -1200 °C [97] and it will result in the formation of silica (SiO_2) with consequent weight increase of the material according to the following relations:

$$\begin{aligned} a) \quad SiC_{(s)} + \tfrac{3}{2}O_{2(g)} &\rightleftharpoons SiO_{2(g)} + CO_{(g)} \\ b) \quad SiC_{(s)} + 2O_{2(g)} &\rightleftharpoons SiO_{2(g)} + CO_{(g)} \end{aligned} \tag{2.9}$$

Silica (SiO_2) has a larger molar volume and is less dense than silicon carbide(SiC) [73] and acts as a protective oxide for the material, providing a barrier to oxygen diffusion. However, it should be noted that the growth of the oxide layer and the transition between the active and passive regimes is still controlled by the oxygen itself according to Fig. 2.7.

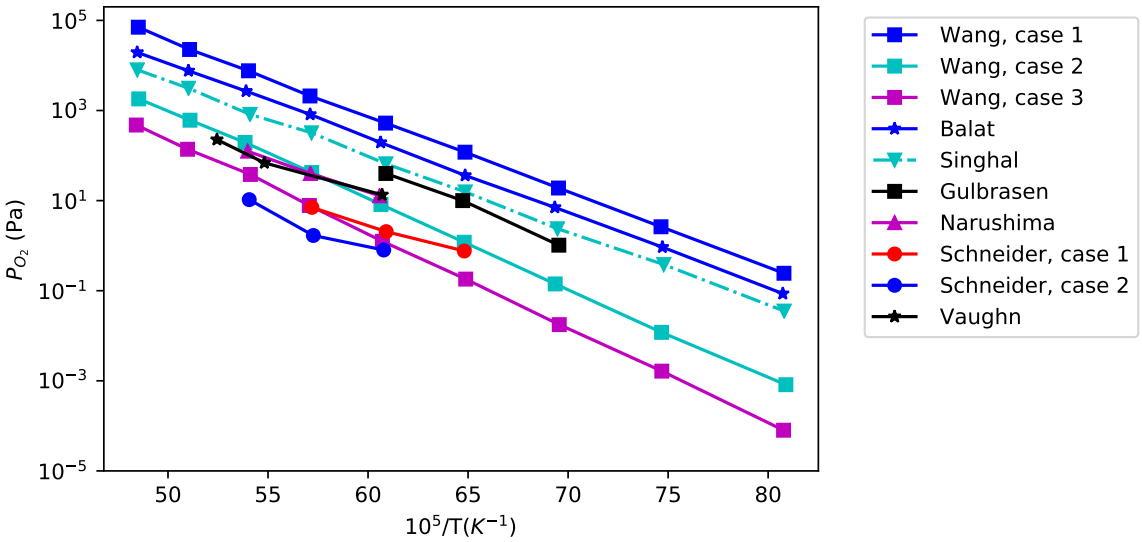

Figure 2.7: Transition between active and passive regime of silicon carbide oxidation depending on oxygen partial pressure and reciprocal temperature evaluated in different works (based on [99]).

Since the temperatures considered in this work are lower than 1000 °C, the SiC matrix layers will be considered as inert layers.

2.4.3 B_4C matrix layers

The boron carbide matrix layers (B_4C) are those which provide the self-healing property of the composite material under investigation. Indeed, when the temperature is over 450°C, these layers react with dioxygen producing B_2O_3 in liquid form according to the following reactions [34, 73]:

$$
\begin{aligned}
a) \quad & B_4C_{(s)} + 4O_{2(g)} \quad \rightleftharpoons \quad 2B_2O_{3(s,l)} + CO_{2(g)} \\
b) \quad & B_4C_{(s)} + \tfrac{7}{2}O_{2(g)} \quad \rightleftharpoons \quad 2B_2O_{3(s,l)} + CO_{(g)} \\
c) \quad & B_4C_{(s)} + 3O_{2(g)} \quad \rightleftharpoons \quad 2B_2O_{3(s,l)} + C_{(s)}
\end{aligned}
\tag{2.10}
$$

However, for temperatures above 900°C , the boron oxide formed is subject to vaporisation according to [73]. Whereas in humid air conditions the boron oxide can be significantly volatilized, in dry air conditions and temperatures under 1000°C, the volatilisation can be neglected. Indeed, as shown in [21], the values of the volatilisation constants are small in this range of temperature.

2.4.4 *pyC* interphase

One of the most widely used interphase materials in CMC is pyrocarbon (pyC). Since it is characterized by a low shear strength, it performs well as a mechanical fuse, deflecting the cracks within it along parallel paths to its stacking planes. However, pyrocarbon is subject to significant oxidation above 400 °C [31]. For temperatures below 700°C the oxidation of carbon produces carbon dioxide ((2.11)(a)), while carbon monoxide is produced for temperatures above 700°C ((2.11)(b)) according to the following reactions:

$$
\begin{aligned}
(a) \quad & C_{(s)} + O_{2(g)} \quad \rightleftharpoons \quad CO_{2(g)} \\
(b) \quad & 2C_{(s)} + O_{2(g)} \quad \rightleftharpoons \quad 2CO_{(g)}
\end{aligned}
\tag{2.11}
$$

2.5 Model description

In order to consider the processes activated by the diffusion of oxygen into the material, a bundle of fibres oriented longitudinally with respect to the direction of the applied load was considered. In this configuration we can assume that, if the applied stress is higher than the ultimate matrix stress, a crack will propagate transversally through the matrix, as illustrated in Fig. 2.8.

In the following section we provide a description as well as a set of PDEs/ODEs for the main modeled phenomena, oxygen diffusion through the crack, and evolution of the chemical species produced and consumed during oxidation, is provided in the following section together with the established PDE model.

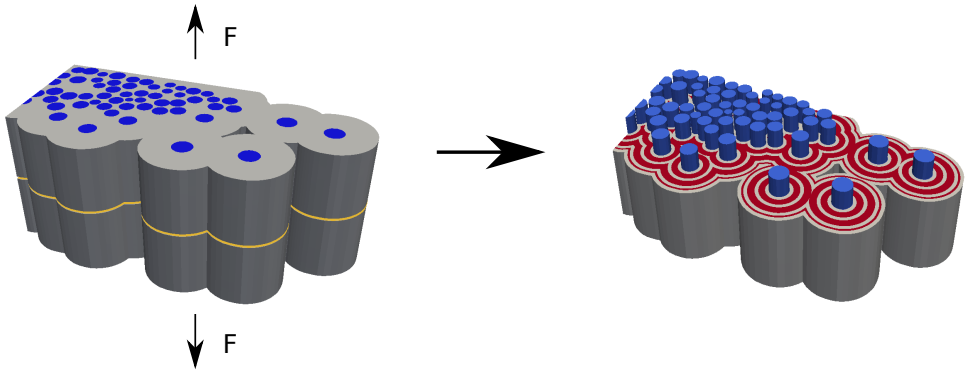

Figure 2.8: Mini-composite with a transverse crack under a tensile load.

2.5.1 Modeling diffusion and oxidation in SH-CMCs cracks

Oxygen diffusion through the crack

As the crack develops in the composite, it starts from a macro-pore in which oxygen concentration can be assumed to be equal to the oxygen concentration on the surface of the composite. The description of the diffusion of oxygen through the crack passes through the definition of the diffusion coefficient. Its definition is fundamental as it gives us an idea of the rate of diffusion through a medium, which is strongly dependent on its nature and state. Two phases of the process are distinguished due to the progressive creation of protective oxide in the crack. In fact, at the first stage, the diffusion of the oxygen takes place through a gaseous medium and successively in a liquid medium such as the oxyde. For each of these states, the diffusion of oxygen can be described by Fick's law considering the flux of oxygen directly proportional to the oxygen concentration gradient through the appropriate diffusion coefficient depending on where the diffusion takes place, as written below:

$$\begin{aligned} \mathbf{J}_{O_2} &= -{D^g}_{O_2} \cdot \nabla C_{O_2} \\ \mathbf{J}_{O_2} &= -{D^l}_{O_2} \cdot \nabla C_{O_2} \end{aligned} \tag{2.12}$$

The diffusion coefficient through the B_2O_3 layer has been modelled in dependence on temperature and activation energy via an Arrhenius-type law determined in [42] for temperatures between 710 and 1200 K. Given a characteristic length L, it is therefore possible to determine characteristic oxygen diffusion times for the two above-mentioned phases through the following relations:

$$\begin{aligned} t_{\text{diff}}^{\text{gas}} &= \frac{L^2}{D^g{}_{O_2}} \\ t_{\text{diff}}^{B_2O_3} &= \frac{L^2}{D^l{}_{O_2}} \end{aligned} \tag{2.13}$$

Considering as reference length L the crack length, at $T = 700°\text{C}$ it is possible to compute the two characteristic diffusion times as follows:

$$\begin{aligned} t_{\text{diff}}^{\text{gas}} &= \frac{L^2}{D^g{}_{O_2}} \approx \frac{1 \cdot (10^{-7})^2}{1 \cdot (10^{-4})} \approx 10^{10} \\ t_{\text{diff}}^{B_2O_3} &= \frac{L^2}{D^l{}_{O_2}} \approx \frac{1 \cdot (10^{-7})^2}{1 \cdot (10^{-10})} \approx 10^{4} \end{aligned} \tag{2.14}$$

It is clear that these relations play a key role in the formation of the oxide in the crack: as soon as the protective plug heals the crack, the characteristic time for oxygen diffusion is greatly reduced and thus fibre degradation is delayed.

Oxydation/production of the chemical species

The oxygen diffusion through the crack also allows the activation of the oxidation phenomenon of the reactive matrix layers, with the consequent production of the liquid oxide, and the recession of the interphase around the fibres. In order to describe the oxidation mechanism of the treated components, the model proposed in [23] was considered. This model assumes that the oxidation reaction occurs at the interface between the liquid oxide layer and the substrate material as is illustrated in Fig. 2.9. Thus, oxygen diffuses from the bulk of the ambient gas to the reactive matrix surface, then diffuses through a liquid layer to reach the oxide-matrix interface, and finally reacts with the substrate.

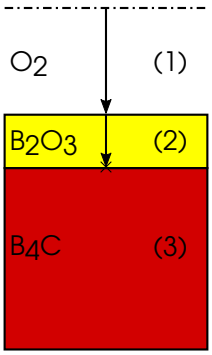

Figure 2.9: Oxidation/reaction model scheme for Eq. 2.15a.

The model also assumes that each of these stages proceeds at a rate proportional to the

oxidant's concentration and in steady-state condition. Thus, denoting as h_l and h_p the height of the layer through which the oxygen must diffuse, the reaction rate constants have the following expressions:

$$\begin{aligned} \frac{1}{k_l} &= \frac{1}{k_{B_2O_3}} + \frac{h_l}{D^l_{O_2}} \\ \frac{1}{k_p} &= \frac{1}{k_{PyC}} + \frac{h_p}{D_{O_2}} \end{aligned} \tag{2.15}$$

in which k_{pyC} and $k_{B_2O_3}$ represent the interfacial rate constant for pyC and B_2O_3.

2.5.2 Oxygen balance equation in the crack

Considering the domain illustrated in Fig. 2.10, a vertically (perpendicularly with respect to the domain) averaged model of oxidation processes in thin cracks, reported in Appendix A.1 for sake of simplicity, enables to write the following system of equations (originally introduced in [81]) for the balance of oxygen concentration in the crack:

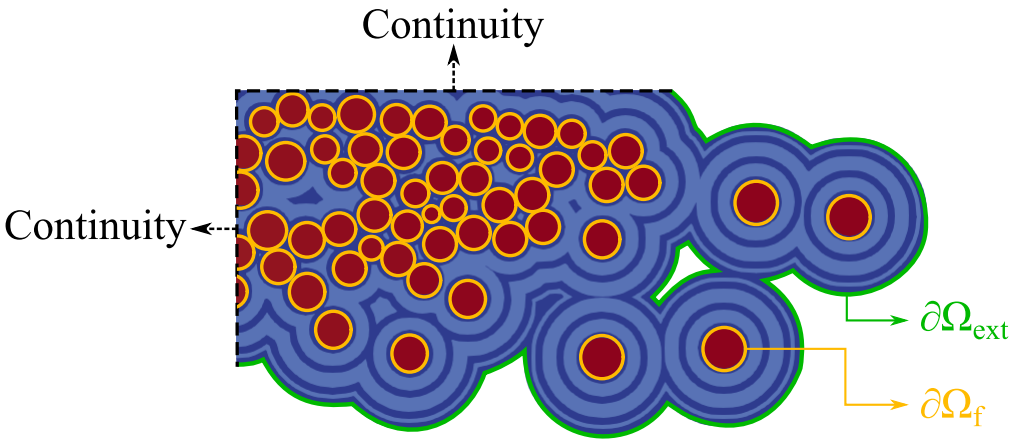

Figure 2.10: Illustration of the considered domain.

The resolution domain consists in a 2D FE mesh directly obtained from the fibre-scale mesh generation tools provided in [17].

$$\begin{cases} \dfrac{\partial}{\partial t}(hC_{O_2}) - \nabla \cdot (D_{O_2} h \nabla C_{O_2}) = -\phi_R \dfrac{C_{O_2} k_l}{4.6} & in \quad \Omega \\ C_{O_2}(t=0) = {C_{O_2}}^{ext} & in \quad \Omega \\ C_{O_2}(t>0) = {C_{O_2}}^{ext} & on \quad \partial\Omega_{ext} \\ -D_{O_2} h \nabla C_{O_2} \cdot \boldsymbol{n_f} = e_p k_p C_{O_2} & on \quad \partial\Omega_f \end{cases} \tag{2.16}$$

In Eq. (2.16) the time-dependent crack-averaged oxygen concentration is expressed as a

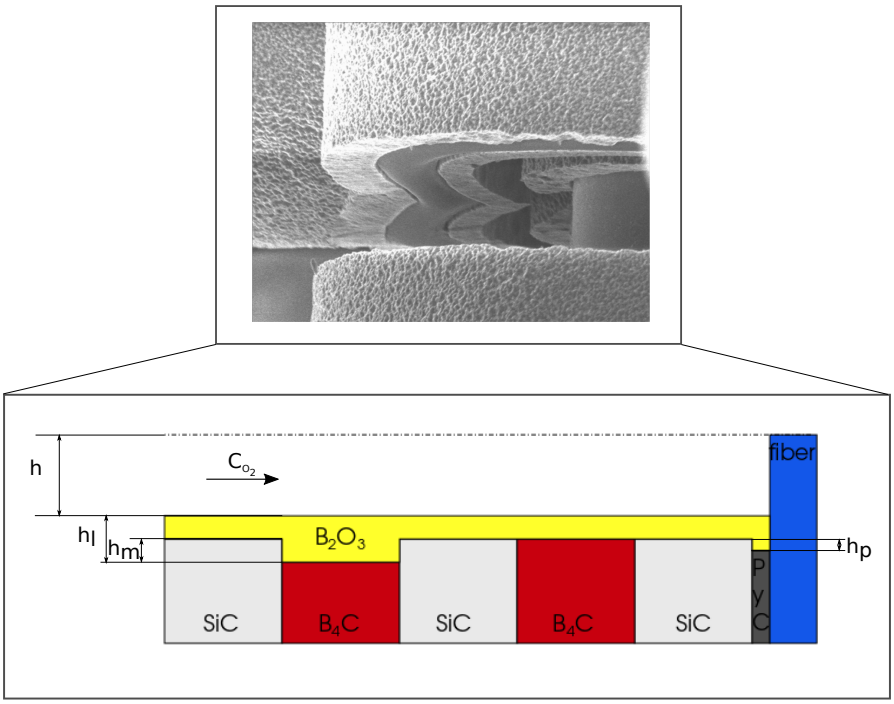

Figure 2.11: Representation of the variables of the system 2.16.

balance between oxygen diffusion and the oxide formation through the crack. The variables expressed in the system (2.16) are represented in Fig. 2.11.

Considering e the crack width, we assume the height h_g as the space occupied by gas, while we denote by h_l the width occupied by the liquid oxide resulting from the matrix oxidation h_m. The height h is then given by $h = e + h_m - h_l$, when the plug has not totally filled the crack, and $h = e$ otherwise. The oxygen diffusion flux in the crack is modelled by Fick's law. In particular, $D^g_{O_2}$ represents the (constant) diffusivity of oxygen in the gaseous phase. The source term in Eq. (2.16) describes the oxidation of the B_4C matrix layers through a reaction rate k_l defined using the model proposed in [23]. The diffusion and the reaction term in the system (2.16) are closely related because, once the oxide fills the crack, oxygen diffusion becomes extremely slow due to the different order of magnitude of the diffusion coefficient. A Dirichlet boundary condition in Eqs. (2.16) is applied on the external domain considering that, at intermediate temperatures, the oxygen concentration in the pores is almost equal to that on the surface of the composite. At the beginning, when the plug is not effective yet, the oxygen concentration is related to the oxygen partial pressure by $C_{O_2} = p_{O_2}/RT$. The other boundary condition is of Robin-type. It establishes a correlation between the oxygen flux reaching the pyC interphase and its oxidation. Once again, the k_p reaction rate is defined by the model proposed in [23].

2.5.3 Evolution of the consumed/produced species

Eqs. 2.16 and 2.15 are completed by the following system, which describes the evolution over time of the growth of the generated oxide layer and the parallel consumption of the B_4C matrix layer and the pyrocarbon interphase:

$$\begin{cases} \dfrac{\partial h_l}{\partial t} = \dfrac{2V^m_{B_2O_3}}{4.6}\phi_R k_l C_{O_2} \\ \dfrac{\partial h_m}{\partial t} = \dfrac{V^m_{B_4C}}{4.6}\phi_R k_l C_{O_2} \\ \dfrac{\partial h_p}{\partial t} = V_{PyC} k_p C_{O_2} \end{cases} \tag{2.17}$$

where h_l is the height of liquid oxide, while h_p and h_m denote the local consumed heights of pyC and matrix reactive respectively. In particular, in correspondence of the inert matrix phases note that $h_l + h_g = e$, the crack width. Otherwise, we have $h_l + h_g = e + h_m$. The above system consists of ordinary linear and homogeneous differential equations of the first order, whose solution is obtained analytically by solving the corresponding problem according to [23].
In the present formulation, an instantaneous spreading of the produced oxide has been considered, as is illustrated in Fig. 2.13; it represents the unit cell of the fibres' bundle in axial-symmetric crack assumption.

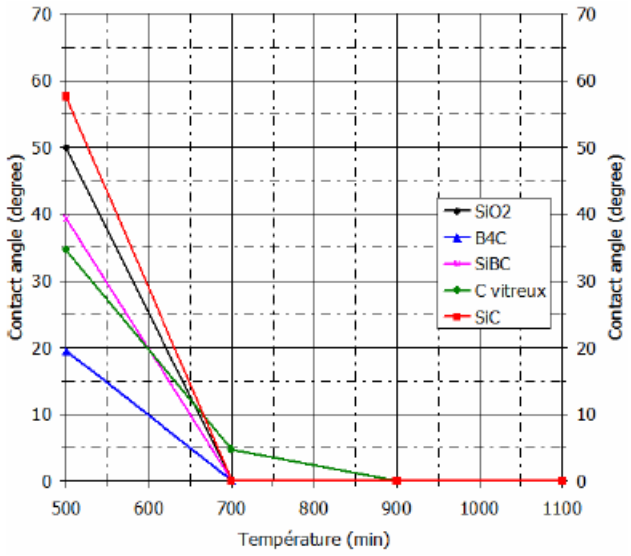

Figure 2.12: Evolution of the contact angle as a function of matrix surface and temperature [101].

This assumption is reasonable considering that at temperatures higher than 700°C it has been demonstrated that the contact angle of the B_2O_3 liquid oxide at the interface with

the matrix is zero [101] as shown in Fig. 2.12.

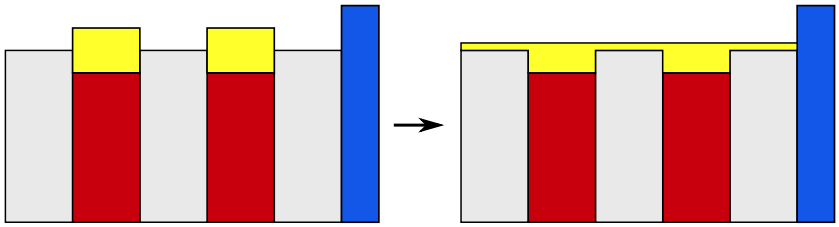

Figure 2.13: A simplified scheme for an instantaneous spreading in a SH-CMC crack.

When the height of the crack is filled by oxide (plug formation), a system equivalent to (2.16) can be written for the concentration of oxygen in the liquid phase, of width h_l, and diffusivity $D^l_{O_2}$.

2.6 Dimensional analysis and optimal time step/scale determination

Dimensional analysis is used to estimate the order of magnitude of the time-scales associated to each process. The final aim is to investigate the correct choice of the simulation time step to correctly track every aspect of the problem, i.e. the oxygen diffusion, the oxide production, the oxygen concentration variation over time, and simultaneously reducing the calculation time required. Indeed, the complete resolution of the system for a 2D domain discretized with finite elements may become computationally heavy. The temporal evolution of the 2D model is performed with A-stable implicit discretizations in time such as implicit Euler or the classical second order implicit backward differencing scheme. This leaves a lot of freedom for the choice of the time step. This choice can account for both physical and computational constraints. In the 2D computations performed in [81], the choice of the time step has been based on a compromise between the characteristic times of diffusion in the process, i.e. oxygen diffusion through a gaseous phase and then through a liquid one. The resulting model has however a computational cost making its use unfeasible for parametric studies of practical interest. In this work, we opted to carry out a proper dimensional study at the micro-scale level to quantify each phenomenon and formally adopt the appropriate choice in terms of time-scales to be accounted for in the simulations. Considering a general variable G, we denote the corresponding non-dimensional variable by G^* given by:

$$G^* = \frac{G}{G_{\text{ref}}} \tag{2.18}$$

The choice of the reference value G_{ref} is fundamental to obtain the correct scaling for the dimensionless model. In particular, this strategy allows the dimensionless groups formed in the equations to assume a physical meaning. The variables and parameters orders of magnitude involved in this study are shown in the Tab.2.1 together with the chosen reference values. The geometric parameters of the crack are representative of a realistic case [86]. The oxygen diffusion coefficient in air is estimated considering the Chapman-Enskog relations [88].

Table 2.1: Orders of magnitude and reference parameters involved in self-healing problem.

Parameter	Order of magnitude	Reference parameter	Order of magnitude
C_{O_2}	1 $[mol/m^3]$	C_{ext}	1 $[mol/m^3]$
h_g	10^{-6} $[m]$	e	10^{-6} $[m]$
h_l	10^{-6} $[m]$	e	10^{-6} $[m]$
h_p	10^{-6} $[m]$	e	10^{-6} $[m]$
t	t_{ref} $[s]$	t	t_{ref} $[s]$
$D^g_{O_2}$	10^{-4} $[m^2/s]$	$D^g_{O_2}$	D_{ref} $[m^2/s]$
$D^l_{O_2}$	10^{-10} $[m^2/s]$	$D^l_{O_2}$	D_{ref} $[m^2/s]$
(x,y)	10^{-7} $[m]$	L	10^{-7} $[m]$
$V^m_{B_4C}$	10^{-5} $[m^3/mol]$	$V^m_{B_4C}$	10^{-5} $[m^3/mol]$
$V^m_{B_2O_3}$	10^{-5} $[m^3/mol]$	$V^m_{B_4C}$	10^{-5} $[m^3/mol]$
V^m_{PyC}	10^{-6} $[m^3/mol]$	V^m_{PyC}	10^{-6} $[m^3/mol]$

Let us consider the unsteady diffusion system (2.16). Dividing each term by the reference parameters linked to the unsteady term, the dimensionless equation assumes the following form:

$$\frac{\partial^*}{\partial t^*}(h^* {C_{O_2}}^*) - \left(\frac{D_{ref} t_{ref}}{L^2}\right) \nabla^* \cdot (D^*_{O_2} h^* \nabla^* {C_{O_2}}^*) = -\left(\frac{D_l t_{ref}}{e^2}\right) \phi_R \frac{C^*_{O_2} k^*_l}{4.6} \tag{2.19}$$

The study is performed by treating the two phases of the self-healing process separately. As stated above, depending on whether the diffusion problem is solved or not in the presence of protective oxide, the dimensional analysis must consider two different diffusion coefficients $D^g_{O_2}$ and $D^l_{O_2}$, which differ by several orders of magnitude. The characteristic oxygen diffusion time in the gaseous and liquid medium are defined as follows:

$$\begin{aligned} t_{gas} &= \frac{L^2}{D^g_{O_2}} = 10^{-10} \\ t_{liquid} &= \frac{L^2}{D^l_{O_2}} = 10^{-4} \end{aligned} \tag{2.20}$$

As a consequence of Eqs. 2.20, oxygen diffusion in air occurs much faster than in the oxide. By substituting the reference values given in Tab.2.1, we can rewrite the Eq. (2.19)

for the two stages of the material healing process as:

$$\frac{\partial^*}{\partial t^*}(h^* C^*_{O_2}) - \left(t_{ref} \cdot 10^{10}\right) \nabla^* \cdot (D^{g*}_{O_2} h^* \nabla^* C^*_{O_2}) = -\left(t_{ref} \cdot 10^4\right) \phi_R \frac{C^*_{O_2} k^*_l}{4.6} \,, \tag{2.21}$$

when the crack is not sealed by the oxide, and as:

$$\frac{\partial^*}{\partial t^*}(h^* C^*_{O_2}) - \left(t_{ref} \cdot 10^4\right) \nabla^* \cdot (D^{l*}_{O_2} h^* \nabla^* C^*_{O_2}) = -\left(t_{ref} \cdot 10^4\right) \phi_R \frac{C^*_{O_2} k^*_l}{4.6} \,, \tag{2.22}$$

after the formation of the liquid plug. In both Eqs. (2.21) and (2.22) it is possible to highlight two dimensionless groups. The first represents the relative importance of the diffusion term with respect to the unsteady term. This group can also be interpreted as the ratio between two characteristic times: the reference time t_{ref}, which is related to the variation of the oxygen concentration over time, and the characteristic time of the oxygen diffusion. The second group defines the time scale of the source term compared to the time scale of oxygen concentration variation in the crack. It is evident that in both phases of the problem, the two dimensionless numbers assume high values. This suggests that the transient plays a minor role in the process, which may as well be considered as stationary. In other words, we will choose the reference time that does not explicitly depend on the characteristic times of diffusion and production. We can also highlight a different aspect related to geometrical considerations by dividing the Eq. (2.19) by the dimensional units of the production term:

$$\left(\frac{e^2}{t_{ref} D_l}\right) \frac{\partial^*}{\partial t^*}(h^* C^*_{O_2}) - \left(\frac{e^2 D_{ref}}{L^2 D_l}\right) \nabla^* \cdot (D^*_{O_2} h^* \nabla^* C^*_{O_2}) = -\phi_R \frac{C^*_{O_2} k^*_l}{4.6} \tag{2.23}$$

We can notice the appearance of the ratio of crack height and on crack length. In particular, the more the considered crack has a high aspect ratio L/e, the less important the diffusion, and the closer this ratio is to unity, the more important will be diffusion compared to production. As before, we can use the reference values of Tab.2.1, and distinguish the cases without and with liquid plug. We obtain

$$\left(t_{ref} \cdot 10^{-2}\right) \frac{\partial^*}{\partial t^*}(h^* {C_{O_2}}^*) - \left(10^8\right) \nabla^* \cdot (D^{g*}_{O_2} h^* \nabla^* {C_{O_2}}^*) = -\phi_R \frac{{C_{O_2}}^* {k_l}^*}{4.6} \,, \tag{2.24}$$

in the gas, and

$$\left(t_{ref} \cdot 10^{-2}\right) \frac{\partial^*}{\partial t^*}(h^* {C_{O_2}}^*) - \left(10^2\right) \nabla^* \cdot (D^{l*}_{O_2} h^* \nabla^* {C_{O_2}}^*) = -\phi_R \frac{{C_{O_2}}^* {k_l}^*}{4.6} \,, \tag{2.25}$$

in the liquid oxide. It is evident that in the gas the reaction term does not significantly influence the diffusion of the oxide. Therefore, it is reasonable to split these two effects in

the simulations. Let us now consider system (2.17) modelling the evolution of heights.

Proceeding as before we obtain the following dimensionless system:

$$\begin{cases} \dfrac{\partial^* h_l^*}{\partial t^*} = \left(\dfrac{t_{ref} V_{B_4C}^m D_{O_2}^l C^{ext}}{e^2}\right) \dfrac{2(V_{B_2O_3}^m)^*}{4.6} \phi_R k_l^* C_{O_2}^* \\ \dfrac{\partial^* h_m^*}{\partial t^*} = \left(\dfrac{t_{ref} V_{B_4C}^m D_{O_2}^l C^{ext}}{e^2}\right) \dfrac{(V_{B_4C}^m)^*}{4.6} \phi_R k_l^* C_{O_2}^* \\ \dfrac{\partial^* h_p^*}{\partial t^*} = \left(\dfrac{t_{ref} V_{B_4C}^m D_{ref} C^{ext}}{e^2}\right) V_{PyC}^* k_p^* C_{O_2}^* \end{cases} \tag{2.26}$$

First, we consider the two equations related to the variation in time of the oxide height and oxidation of the reactive matrix layers. We can see that both equations have the same dimensionless group that depends proportionally on the oxygen concentration, on the interfacial velocity constants, and, consequently, on the evolution of the oxide height (according to the model in [23]). By substituting the values listed in Tab.2.1 we obtain the following system:

$$\begin{cases} \dfrac{\partial^* h_l^*}{\partial t^*} = (t_{ref} \cdot 10^{-3}) \dfrac{2(V_{B_2O_3}^m)^*}{4.6} \phi_R k_l^* C_{O_2}^* \\ \dfrac{\partial^* h_m^*}{\partial t^*} = (t_{ref} \cdot 10^{-3}) \dfrac{(V_{B_4C}^m)^*}{4.6} \phi_R k_l^* C_{O_2}^* \end{cases} \tag{2.27}$$

Since the diffusion/reaction process for the oxygen concentration can be assumed quasi-stationary, it is possible to adapt the time step of the complete self-healing problem to follow the evolution of the oxide height. In practice, an adaptive time step has been chosen in this sense. As a result, we have reduced the computational time required to simulate 1000 hours of the material lifetime to a few minutes on a laptop, making the implementation of the model a lot more interesting for practical applications compared to the one of [81].

The modelling of the interphase oxidation around the fibres has been then considered. Fig. 2.14 shows two boundary cases: the first case shows the interphase in direct contact with the oxide (Fig. 2.14(a)), in the second, the interphase oxidizes as a result of the diffusion of oxygen in the air (Fig. 2.14(b)). The actual configuration is, in fact, a function of the viscosity of the oxide and its ability to penetrate and fill the thin interfacial layer.

Therefore, the dimensionless form of the equation related to pyC oxidation in Eqs. 2.26 can be written by referring to the above cases, respectively related to configuration (a) and (b):

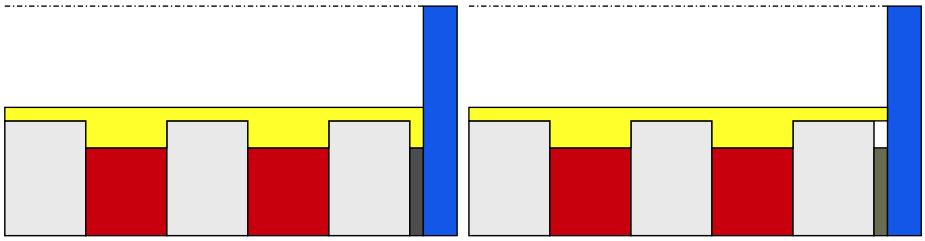

(a) (b)

Figure 2.14: Interphase oxidation models around the fibre.

$$\begin{cases} \dfrac{\partial^* {h_p}^*}{\partial t^*} = (t_{ref} \cdot 10^3)\, {V_{PyC}}^* {k_p}^* {C_{O_2}}^* \\ \dfrac{\partial^* {h_p}^*}{\partial t^*} = (t_{ref} \cdot 10^{-3})\, {V_{PyC}}^* {k_p}^* {C_{O_2}}^* \end{cases} \tag{2.28}$$

The interphase oxidation rate in the two cases differs by the same amount as the difference in the characteristic diffusion times orders of magnitude related to the two phases considered as we expect.

For a better insight, the one-dimensional model presented above has been studied. The simulation of self-healing has been carried out considering the two different boundary conditions applied to the fibre's boundary. In Tab. 2.2 the respective consumed pyrocarbon height is reported for different simulation time.

Table 2.2: Pyrocarbon consumed height at T = 700°C for different boundaries condition applied on the fibre at different times in one-dimensional SH problem.

Time	h_p (case a) $[\mu m]$	h_p (case b) $[\mu m]$
21 s	0.6651	0.6651
267 s	7.5083	7.5090
28 hr	7.5550	9.1612
9696 hr	129.67	37675

The consumed pyrocarbon interphase is almost the same in the first hours of simulation. The major difference lies in its final value, and, in particular, in case (b) the discrepancy is more than one order of magnitude after $\sim$ 10000 hours. This can be explained by the fact that at that time, the oxygen, which was previously consumed by the reactive matrices, reaches the fibre's boundary and then spreads into the gas more rapidly than in case (a).

2.6.1 Boundary conditions and their influence on the model

To understand the influence of this choice on the system evolution, the variational formulation of the global problem in the dimensionless form has been studied. Denoting

by ν a generic test function the variational formulation reads:

$$\iint_{\Omega} \nu \partial_t(hC)d\Omega + \iint_{\Omega} Dh\nabla\nu \cdot \nabla C d\Omega - \int_{\partial\Omega_f} \nu F_n d\gamma - \int_{\partial\Omega_{ext}} \nu F_n d\gamma + \iint_{\Omega} \nu \frac{\phi_R k_l C}{4.6} d\Omega = 0 \quad (2.29)$$

The normal flux of oxygen at the fibres' boundary is defined by the expression below (cf Eq. (2.16)c):

$$F_n = e_p k_p C_{O_2} \qquad on \quad \partial\Omega_f \quad (2.30)$$

At the external boundary, a weak approximation of the Dirichlet condition is obtained by computing the oxygen normal flux through a layer of thickness equal to δ is proportional to the difference between the oxygen concentration inside and outside the boundary (for δ tending to zero this means applying a Dirichlet condition $C_{O_2} = C^{ext}_{O_2}$, see also [3] and references therein):

$$F_n = \frac{eD}{\delta}(C_{O_2} - C^{ext}_{O_2}) \qquad on \quad \partial\Omega_{ext} \quad (2.31)$$

By inserting Eq. (2.30) and Eq. (2.31) into Eq. (2.29), the variational formulation can be rewritten with the appropriate boundary condition:

$$\begin{aligned} \iint_{\Omega} \nu \partial_t(hC)d\Omega + \iint_{\Omega} Dh\nabla\nu \cdot \nabla C d\Omega - \int_{\partial\Omega_f} \nu e_p k_p C_{O_2} d\gamma \\ - \int_{\partial\Omega_{ext}} \nu \frac{eD}{\delta}(C_{O_2} - C^{ext}_{O_2})d\gamma + \iint_{\Omega} \nu \frac{\phi_R k_l C}{4.6} d\Omega = 0 \end{aligned} \quad (2.32)$$

By resizing each term considering the reference values in the Tab.2.1 and reporting the respective order of magnitude, we obtain:

$$\begin{aligned} \iint_{\Omega} \left(\frac{h_{ref}C_{ref}}{t_{ref}}\right) \nu \partial_t(hC)d\Omega + \iint_{\Omega} \left(\frac{D_{ref}h_{ref}C_{ref}}{L^2{}_{ref}}\right) Dh\nabla\nu \cdot \nabla C d\Omega \\ - \int_{\partial\Omega_f} (D_{ref}C_{ref})\nu e_p k_p C_{O_2} d\gamma - \int_{\partial\Omega_{ext}} \left(\frac{D_g h_{ref}C_{ref}}{\delta_{ref}}\right) \nu \frac{eD}{\delta}(C_{O_2} - C^{ext}_{O_2})d\gamma \\ + \iint_{\Omega} \left(\frac{D_l h_{ref}C_{ref}}{h_{ref}}\right) \nu \frac{\phi_R k_l C}{4.6} d\Omega = 0 \end{aligned} \quad (2.33)$$

Dividing through by the transient term results in the following formulation for the

gas-diffusion stage

$$\iint_{\Omega} \nu\partial_t(hC)d\Omega + (10^{10}\cdot t_{ref})\iint_{\Omega} Dh\nabla\nu\cdot\nabla C d\Omega - (10^{2}\cdot t_{ref})\int_{\partial\Omega_f} \nu e_p k_p C_{O_2} d\gamma \\ -\left(\frac{10^{-2}}{\delta_{ref}}\cdot t_{ref}\right)\int_{\partial\Omega_{ext}} \nu\frac{eD}{\delta}(C_{O_2}-C_{O_2}^{ext})d\gamma + (10^{3}\cdot t_{ref})\iint_{\Omega}\nu\frac{\phi_R k_l C}{4.6}d\Omega = 0\ . \tag{2.34}$$

For the oxide-diffusion stage we have

$$\iint_{\Omega} \nu\partial_t(hC)d\Omega + (10^{4}\cdot t_{ref})\iint_{\Omega} Dh\nabla\nu\cdot\nabla C d\Omega - (10^{-4}\cdot t_{ref})\int_{\partial\Omega_f} \nu e_p k_p C_{O_2} d\gamma \\ -\left(\frac{10^{-4}}{\delta_{ref}}\cdot t_{ref}\right)\int_{\partial\Omega_{ext}} \nu\frac{eD}{\delta}(C_{O_2}-C_{O_2}^{ext})d\gamma + (10^{3}\cdot t_{ref})\iint_{\Omega}\nu\frac{\phi_R k_l C}{4.6}d\Omega = 0 \tag{2.35}$$

We can clearly see that for both stages the importance of the external boundary condition is very limited compared to the other phenomena, and in particular compared to the boundary condition on the fibres. Therefore, it is expected that a change in the parameters' values in boundary condition does not substantially affect the global self-healing process behaviour. In this work we assumed as boundary conditions on the fibres the situation shown in Fig 2.14a, i.e. the case in which the oxide is in direct contact with the pyC interphase, as the temperatures considered are higher than 700°C.

2.6.2 Numerical discretization and implementation

The numerical resolution of system (2.16) is achieved using a developed finite element scheme which consists of discretization over a basis functions set of the proposed variational formulation in (2.32) [106]. The algebraic system obtained is then solved considering the basis function parameters as the variable values at the integration points of the elements. In particular, triangular P1 elements are used in this study. For the discretization over time a first-order implicit Euler scheme is used. The solution for each time step is then coupled with the resulting calculation of the heights evolution (2.17) system which can be obtained analytically as demonstrated in [23]. However, a complete description of the numerical formulation of the system is given in [80].

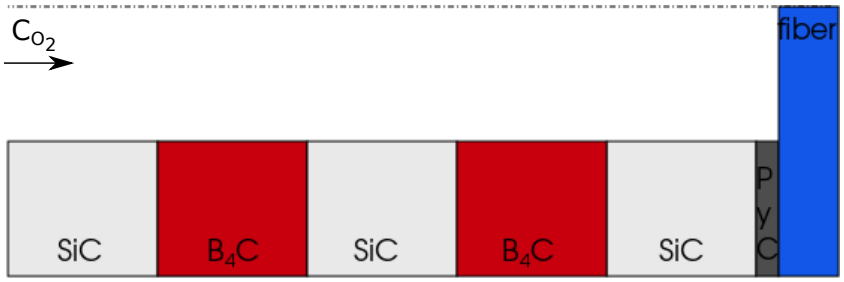

Figure 2.15: One-fibre 1D scheme for transverse crack in SH-CMC.

2.7 Model results

2.7.1 1D Results

The domain consists in $SiC/B_4C/SiC/B_4C/SiC$ matrix layers, pyC interphase, Hi-Nicalon fibre and it is illustrated in Fig. 2.15.
In the Fig.2.16 are represented the successive phases of the self-healing simulation on the one-dimensional scheme problem. At the beginning the oxygen concentration is constant throughout the crack and is equal to the value chosen as a boundary condition on the external domain (Fig.2.16(a)). This value remains constant until the oxide completely fills the crack. At that time the oxygen concentration has a drop, due to the fact that the oxygen spreads slowly in the gas than in the oxide which is in the liquid state (Fig.2.16(b)). The reactive matrix layers are then oxidized in function of the amount of oxygen present along the crack. For this reason, the reactive matrix layer closest to the outer domain will be consumed first (Fig.2.16(c)). The consumption of the interphase that protects the fibre, remains almost constant as soon as the crack has been filled by the oxide, and then increases when the oxygen oxidize the available matrix and reaches the fibre tip. Finally, the oxygen concentration along the crack assumes steady-state conditions (Fig.2.16(d)).

2.7.2 2D Results

The self-healing problem was then performed on a two-dimensional mesh considering the tow represented in Fig. 2.10.
The variation of the problem's variables, such as the oxygen concentration, the height of the liquid oxide together with the consumed matrix value, and the interphase consumption, are recorded during the time simulation. As well as done for the one-dimensional case, the same phases have been reported in Fig. 2.17, Fig. 2.18, Fig. 2.19, Fig. 2.20 for each of the above-mentioned variables.
It is evident that, also in this case, the produced oxide fills the entire cracked tow in a few

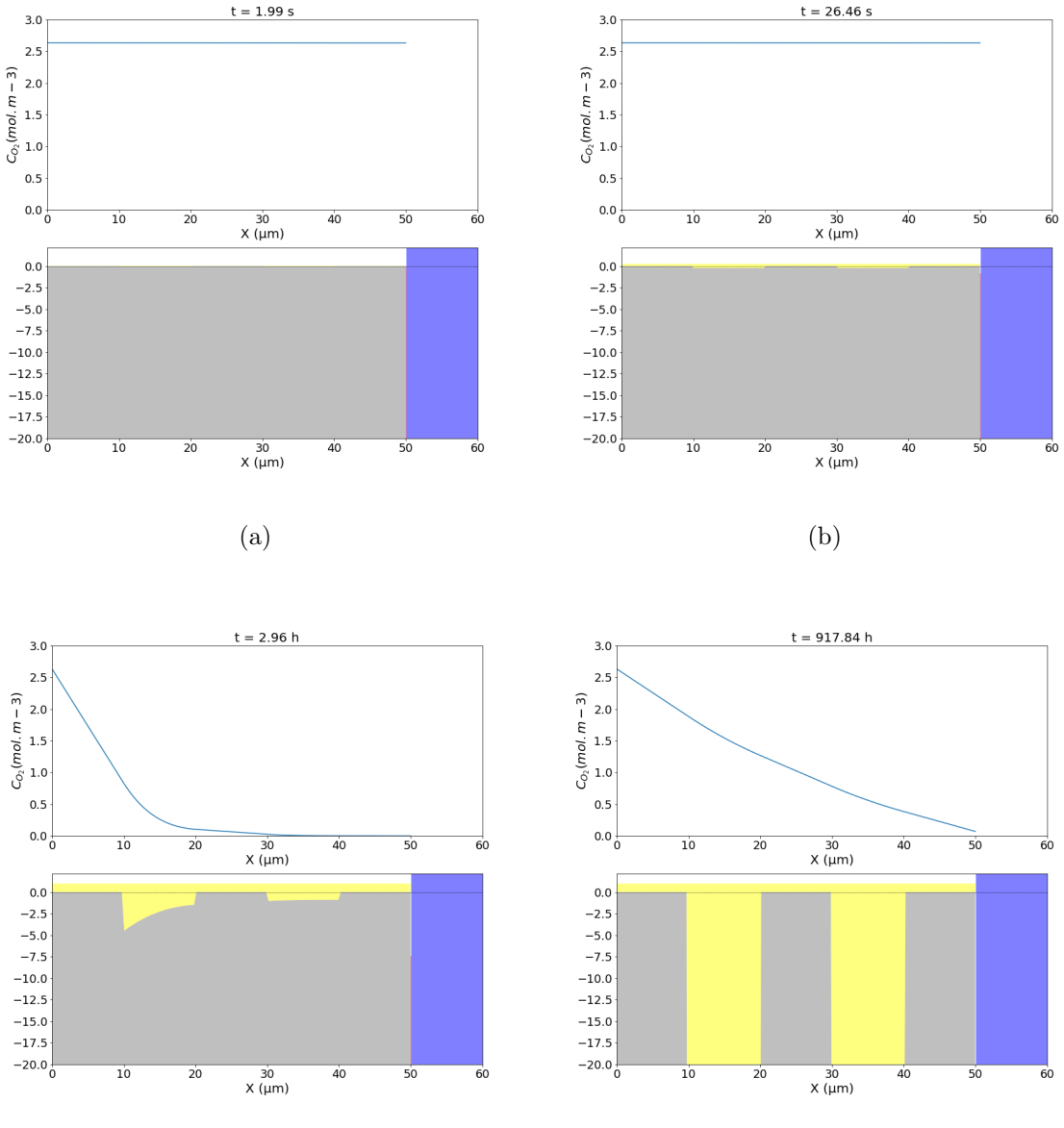

(a) (b)

(c) (d)

Figure 2.16: Different phases of the self-healing simulation on the one-dimensional scheme problem.

seconds (29 sec). The oxygen concentration diffuses from the outer to the inner part of the bundle and, as a direct consequence, the consumption of the oxidized species, such as the reactive matrix layers and the pyrocarbon interphases, follows the direction of the oxygen diffusion gradient. The final interphase consumption for each fibre as a function of oxygen concentration is shown in Fig. 2.21. Fibres with the highest oxygen concentration are the ones around which the pyC interphase is most consumed. The data points can be well fitted by a power law with exponent 0.6103, which is higher than the naively

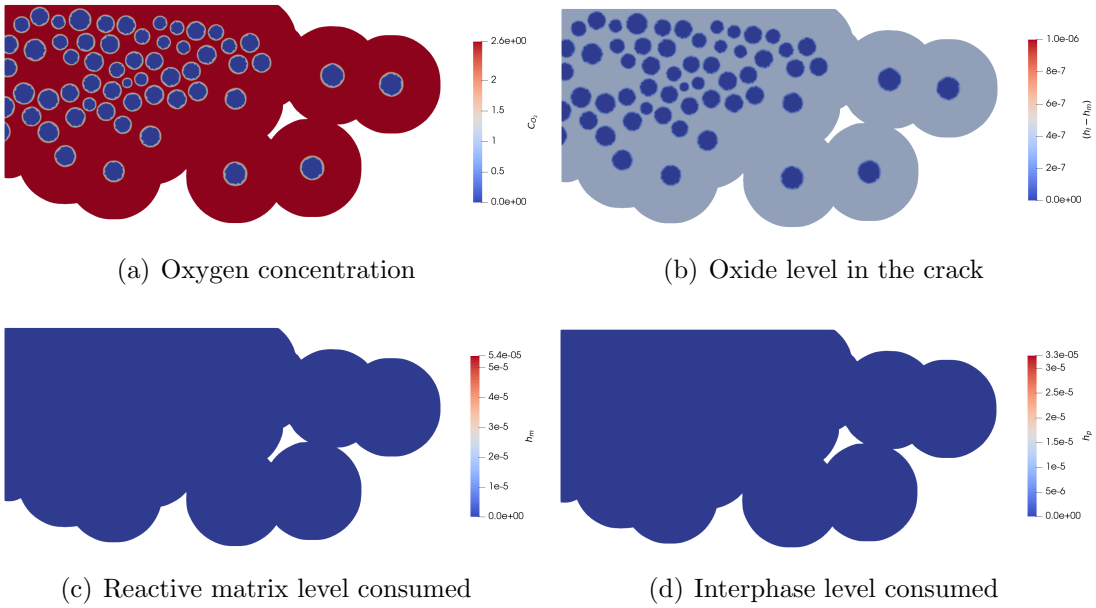

(a) Oxygen concentration (b) Oxide level in the crack

(c) Reactive matrix level consumed (d) Interphase level consumed

Figure 2.17: Two-dimensional self-healing simulation at $t = 29$ sec.

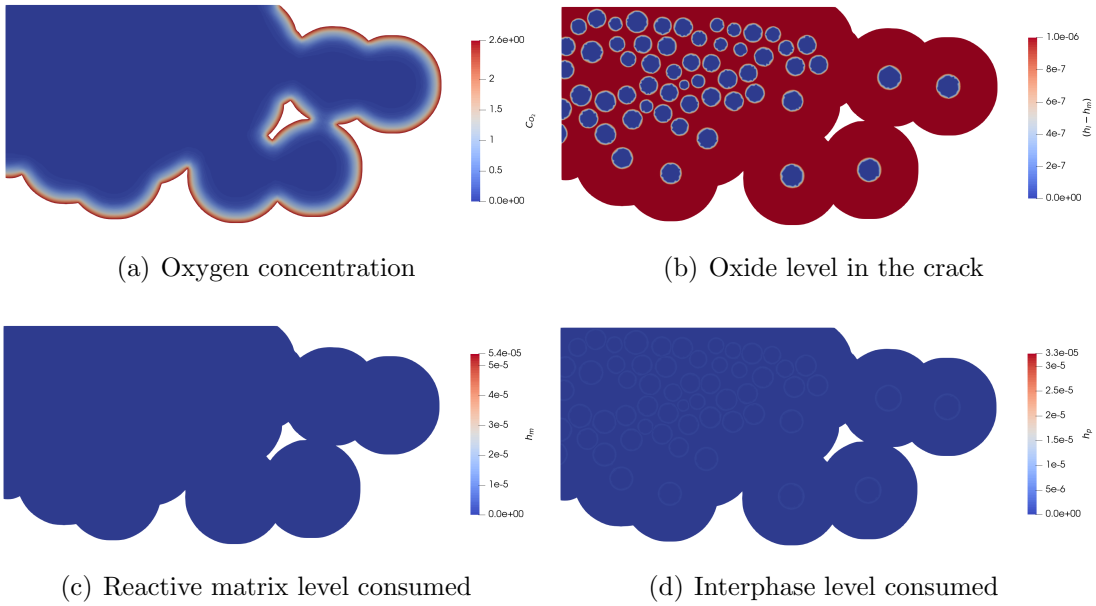

(a) Oxygen concentration (b) Oxide level in the crack

(c) Reactive matrix level consumed (d) Interphase level consumed

Figure 2.18: Two-dimensional self-healing simulation at $t = 4$ min .

expected 1/2 exponent arising from a classical parabolic oxidation model.

2.8 Chapter summary

In this chapter, the modelling strategy for oxidation and healing mechanism of cracks in CMCs has been presented and discussed. In particular, the two-dimensional section

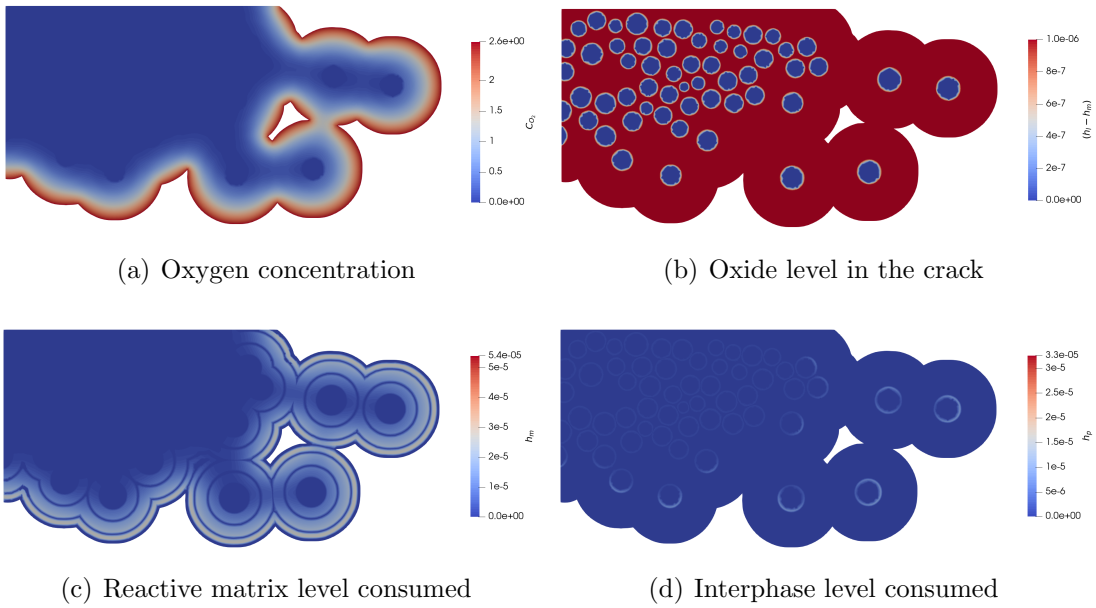

(a) Oxygen concentration

(b) Oxide level in the crack

(c) Reactive matrix level consumed

(d) Interphase level consumed

Figure 2.19: Two-dimensional self-healing simulation at $t = 28$ hr .

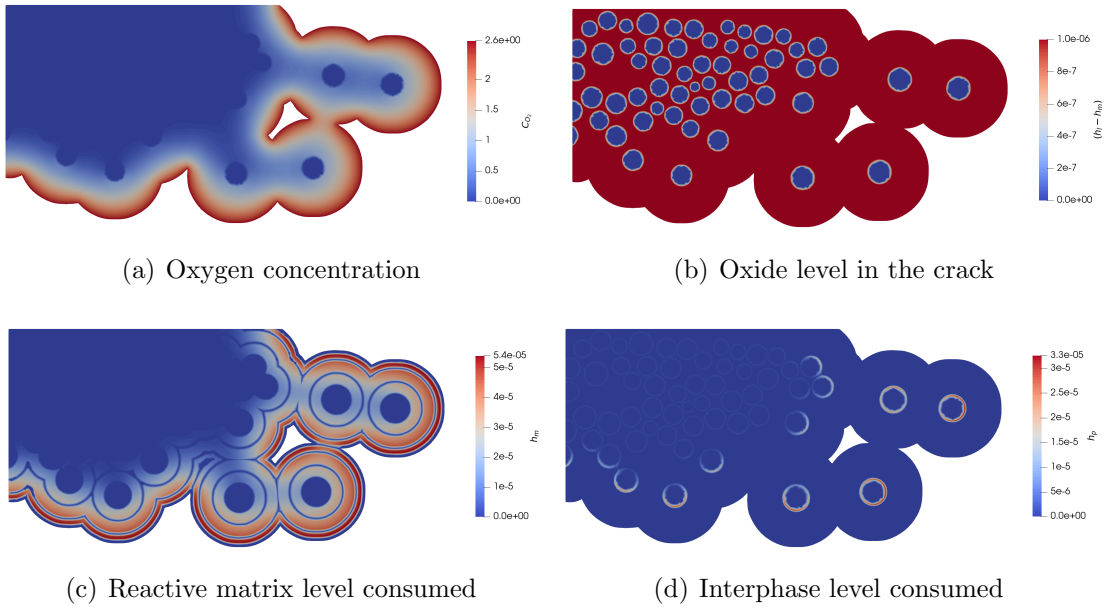

(a) Oxygen concentration

(b) Oxide level in the crack

(c) Reactive matrix level consumed

(d) Interphase level consumed

Figure 2.20: Two-dimensional self-healing simulation at $t = 4$ days .

averaged model for the diffusive-reactive processes in the transverse crack has been presented. The model can accurately describe the physical/chemical phenomena occurring in the crack over time, particularly the oxygen concentration field, the regression of the reactive matrix layers and the related oxide production, and the oxidation of the interphase around the fibres. This version is modified with respect to the work in [81] since, thanks to a dimensional analysis of the PDE describing the system, it was possible

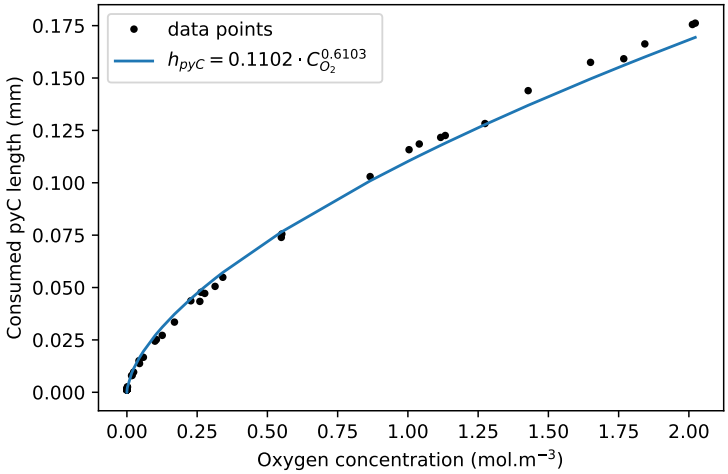

Figure 2.21: Ultimate pyC interphase consumed w.r.t. oxygen concentration at fibres' tip at $T = 973$ K.

to make a suitable choice on the integration step. In particular, considering that diffusion/reaction process for the oxygen concentration can be assumed quasi-stationary, the time step of the complete self-healing problem can be adapted following the evolution of the oxide height. This choice solves a significant problem of the two-dimensional description of the self-healing process, i.e. the computational time required. Furthermore, the variational formulation in the weak and dimensionless form of the above-written system of equations made it possible to highlight the influence of the boundary conditions corresponding to two extreme cases. In particular, this system is globally unaffected by major variations in boundary parameter values. The results generated by the proposed model were then analysed first by considering a one-dimensional formulation, and thus a one-dimensional domain ($SiC/B_4C/SiC/B_4C/SiC$ matrix layers, pyC interphase, Hi-Nicalon fibre) and finally for a two-dimensional configuration representing a cross-section of a mini-composite consisting of 58 fibres. The results have shown the direct correlation between oxidation of the reactive matrix layers and the concentration of oxygen present in the crack. In particular, the evolution of the oxygen concentration over time was determined. The oxygen concentration levels in the crack are constant until the produced oxide fully heals the crack. Subsequently, the diffusion of oxygen is slowed down due to the difference in the diffusion coefficients of air and boron dioxide. The oxygen then diffuses slowly through the crack until it reaches a steady-state. The pattern of oxygen diffusion in the crack is radial; oxygen diffuses from the outer edge towards the inner part of the composite, resulting in different oxidation of matrix layers, interphase (and as we will discuss in more detail below, fibres) depending on the position of these

elements within the composite. This concept brings out the importance of modelling this phenomenon in 2D taking into account the topology of the mini-composite. This formulation of the problem can also be applied in humid air conditions, as proposed in [81]. In such conditions, it would indeed be interesting to analyse the different scenarios and the healing times of the crack in the presence of oxide volatilisation.

Chapter 3

Slow crack growth model for fibre degradation

Contents

3.1 Introduction

Unfortunately, despite the introduction of reactive matrices and the resulting crack healing, the fibres' protection from the environment is not complete. In particular, fibres are attacked by an aggressive environment, such as air, and are damaged through an oxidation process [27, 33]. Consequently, the degradation mechanisms of the fibres are the most critical factors in the operational life of the material [15, 37]. For this reason, a general overview of degradation mechanisms for SiC based ceramic fibres is presented in the first part of this chapter. The second part of the chapter is consecrated to the description of the sub-critical propagation of defects in ceramic fibres and to the illustration of adopted the model in order to quantify the degradation of the fibres' strength and their lifetimes. However, the sub-critical crack propagation model presented contains variables and parameters that can reflect varying conditions, both in terms of the material and operating environment, and has a certain degree of statistical dispersion in the data. In addition, the model defines parameters that are calibrated on experimental data. Consequently, there is a question mark over how the uncertainty of the input parameters can be propagated throughout the model, giving a solid contribution to the variability of the model response. In particular, the model results can be as highly correlated to an input parameter as small changes in the input cause significant output changes. Therefore a sensitivity analysis of the proposed model is performed in the last part of the chapter to investigate the degree of the related variability ensuring the model stability.

3.2 Hi-Nicalon ceramic fibres

Most of the studies on SiC/SiC composites have been done considering Nicalon and Hi-Nicalon fibres as they exhibit good mechanical strength (good stiffness and high tensile strength) even at high temperatures.

However, the second-generation fibres mentioned above contain some impurities due to their composition and therefore undergo a significant degradation of their properties when exposed to irradiation. There is currently a third generation of SiC fibres, such as the Hi-Nicalon S fibres and the Tyranno SA3 fibres, which show an improved resistance to oxidation compared to the previous generation [48, 79]. Fig. 3.1 shows the different types of fibres belonging to the Nicalon family, highlighting their composition and manufacturing processes. Cross-linking through irradiation instead of oxidation (as is the case for the manufacture of Nicalon fibres) allows reducing the amount of oxygen within

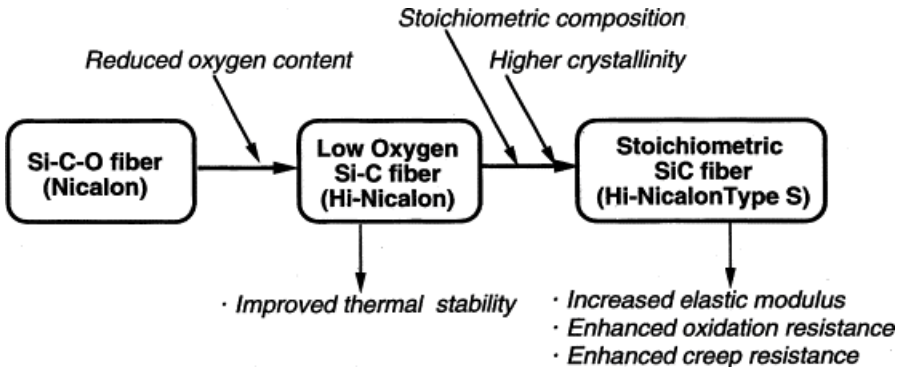

Figure 3.1: Schematic historical flowchart of Nicalon fibres development [96].

the Hi-Nicalon and Hi-Nicalon S fibres. Furthermore, the improved pyrolysis process allows Hi-Nicalon S fibres to have almost stoichiometric proportions and a largely crystalline structure (SiC_α and SiC_β forms).

	d (μm)	E (GPa)	$\overline{\sigma_R}$ (GPa)	$\overline{\epsilon_R}$ $(\%)$
Nicalon NLM-202	14	190	2	1.05
Nicalon NL-202	14	220	3	1.35
Hi-Nicalon	14	260	2.6	1.00
Hi-Nicalon S	13	375	2.5	0.65

Figure 3.2: Initial mechanical properties for Nicalon fibres [96].

Concerning the mechanical properties of the different fibre types mentioned above, Tab. 3.2 shows the main initial characteristic values. According to the latter, it is evident that irradiation cross-linking increases the stiffness and tensile strength of Hi-Nicalon and Hi-Nicalon S fibres compared to Nicalon by suppressing the $Si-C-O$ phase and reducing the defect size. Furthermore, the stiffness of Hi-Nicalon S fibres is better than that of Hi-Nicalon fibres as the improved pyrolysis process increases the SiC_β phase but reduces the strain at break.

3.2.1 Degradation mechanisms for ceramic fibres

The following section outlines the main chemical and physical/chemical degradation mechanisms for the Nicalon fibre family.

Chemical degradation

There is an auto-oxidation of Si-C-O which generates new defects within the fibres and which reduces the thermal stability of Nicalon fibres compared to Hi-Nicalon and

Hi-Nicalon S. In an inert atmosphere all these fibres have a reduction in tensile strength at temperatures above 1400°C as shown in Fig. 3.3.

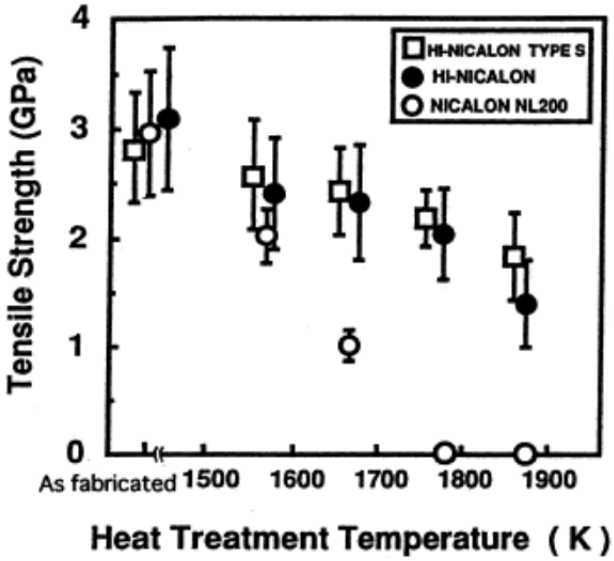

Figure 3.3: Tensile strength of SiC fibres exposed at different temperatures in argon after 10 hours [96].

However, the oxidation of SiC by O_2 generates defects in the periphery of the fibres that reduce the chemical stability more rapidly than the auto-oxidation of $Si - C - O$ regardless of the crystal structure [96]. In Fig. 3.4, a decrease in the tensile strength of all Nicalon types fibres can be observed for temperatures above 1200°C in an oxidising atmosphere.
A further evidence of the independence of this mechanism from the crystalline structure is given by the equal growth of the SiO_2 layer on the surface of the fibres (see Fig. 3.5). The ultimate tensile strength of fibres belonging to the Nicalon family is constant up to 1000°C.

Physico-chemical degradation

In laboratory tests, fibre failures have been observed when subjected to a load that was lower than their ultimate tensile strength and in an oxidising atmosphere for temperatures below 1000°C [38]. Under these conditions, fibre failure is due to the sub-critical propagation (or slow propagation) of defects on the fibre surface by oxidation. It is due to the chemical reaction that occurs on the crack front, which, being also subjected to a certain load, opens up by spreading the grains of the material. As a result, the crack propagates even if the intensity of the load is less than that of the critical load. This is therefore referred to as sub-critical carck growth (SCG). Sub-critical propagation

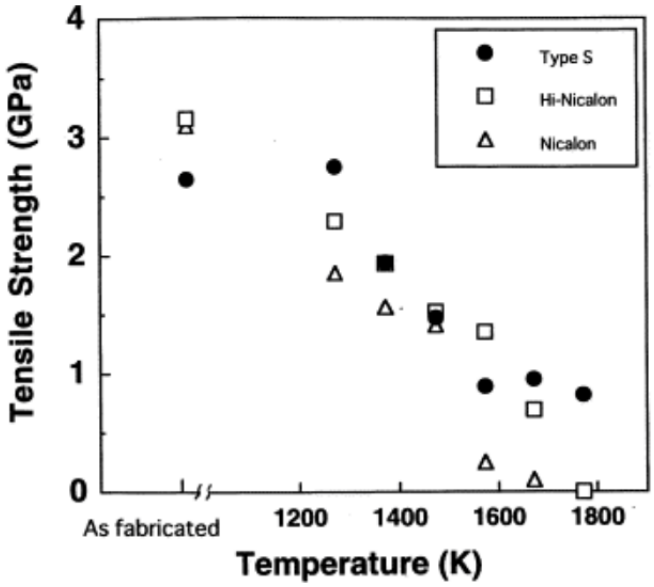

Figure 3.4: Tensile strength of SiC fibres exposed at different temperatures in air after 10 hours [96].

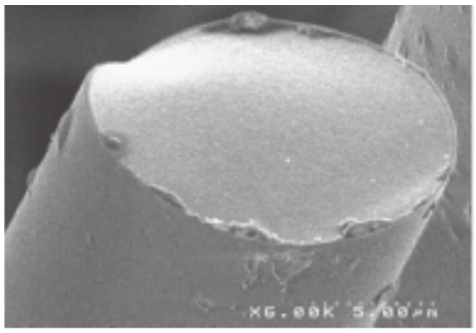

Figure 3.5: SiO_2 oxide layer on a Hi-Nicalon fibre [37].

occurs in two phases: in the first phase, called reaction controlled, the defect size increases due to the oxidation reaction as oxygen is in excess on the fibre surface. The second phase is called diffusion controlled in that the oxygen supply on the surface of the defect is slowed down by its diffusion through the oxide layer that forms around the fibre. An SEM representation of a flaw and of the silica layer on the fracture surface of Nicalon fibre is given in Fig. 3.6.

3.3 Lifetime of SiC fibres - sub-critical propagation

The slow crack growth phenomenon, also called static fatigue, has experimental and fractographical bases [38]. The diffusion of oxygen controls the oxidation of the fibres through the oxide layer. Many existing works use a the Paris-Erdogan law for its

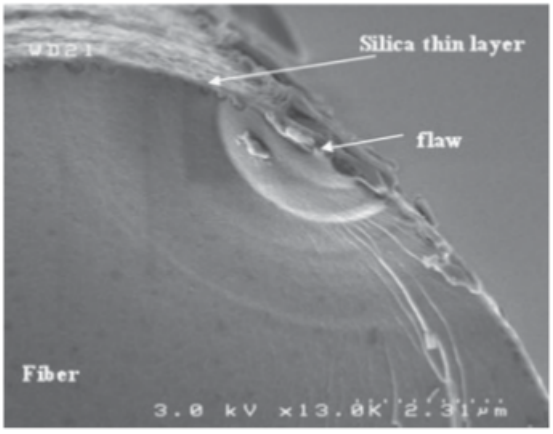

Figure 3.6: Defect and silica oxide layer in Nicalon fibre at 700 °C [59].

description [27, 37, 98, 104] that correlates crack velocity with the crack stress intensity factor K computed under the assumption of elastic behaviour:

$$\frac{da}{dt} = C \cdot (\Delta K)^n \tag{3.1}$$

where a is the defect size, C and n represent the material coefficients dependent on environmental effects, stress ratio and specimen size. The stress intensity factor K depends on the sample geometry, the crack position, and the load applied to the material. The dependence on the environment is ensured via the coefficients C and n obtained experimentally. This indirect dependence on the external condition, as e.g. variable oxygen concentration as it is the case within the crack, is the main limitation of this law. Moreover, the formation of a thin, uniform layer of silica (silicon dioxide) on the surface of the fibres between 650°C and 730°C is observed. The tests show that the growth of the silica layer on the surface of the fibres is not responsible for the fracture.

3.3.1 Weibull theory for fibre failure

To deal with the failure of ceramic materials many works [18, 25, 44, 45, 60] consider the theory formulated by Weibull [100]. This theory assumes that there is only one population of defects, differing only in size and position, whose distribution is defined by a Poisson process. Therefore the probability p^k of finding a defect with rank k depends on the intensity of the process λ according to the following relation:

$$p^k(\lambda) = \frac{e^{-\lambda}\lambda^k}{k!} \tag{3.2}$$

In particular, the intensity λ of the process depends on the size of the domain Ω according

to the following:

$$\lambda(\Omega, \sigma) = \frac{|\Omega|}{|\Omega_0|} \left(\frac{\sigma}{\sigma_0} \right)^m \tag{3.3}$$

where Ω_0 is a fixed reference value and σ_0 and m are experimentally determined parameters that define the mean and dispersion of the distribution. Considering that the theory assumes that as soon as a defect is activated within a volume, the volume is broken, its probability of failure p_R is written as:

$$p_R(\lambda) = p^{k>=1}(\lambda) = \sum_{k=1}^{+\infty} p^k(\lambda) = 1 - p^0(\lambda) = 1 - e^{-\lambda} \tag{3.4}$$

3.3.2 Slow crack growth model

In this work we have followed the approach formulated in [56]. In this approach, the environment modifies the damage zone only at the cracks tip, and it does not depend explicitly on temperature but depends only on the total oxygen flux reacting at the crack tip (which, in turn, depends on the temperature and the oxygen pressure). Consequently, the model is valid for any temperature or oxygen pressure, which can be functions of time. The growth of surface defects is assumed to be a one-dimensional problem in which a scalar parameter describes the size of a defect. Thus, the Stress Intensity Factor (SIF), denoted with K, is approximately uniform along the crack tip and considering that the impact of the environmental conditions on the elasticity coefficients is limited. In ceramics fracture starts in general from small flaws, which are discontinuities in the micro-structure and which, for simplicity, can be assumed to be small cracks distributed in the surface or volume. Strength then depends on the size of the largest (or critical) defect in a specimen, and it varies from component to component. Due to this reason, design with ceramics has to be approached statistically. In the Weibull theory, the strength of a fibre of length L, denoted with σ_R, follows the cumulative density function obtained by collecting together Eqs. (3.3) and (3.4):

$$P(\sigma_R < \sigma) = 1 - \exp\left(-\frac{L}{L_0} \left(\frac{\sigma}{\sigma_0} \right)^{m_\sigma} \right) \tag{3.5}$$

where L_0 , m_σ and σ_0 are the classical Weibull coefficients. In particular, the Weibull modulus m_σ describes the scatter of the strength data, the characteristic strength σ_0 is the stress at which, for specimens of volume $V = V_0$, the failure probability is equal to $1 - \exp(-1) = 63\%$. For Hi-Nicalon fibres, such parameters were estimated in the work [38] and reported in Tab. 3.1.

Table 3.1: Weibull coefficients for Hi-Nicalon fibres.

L_0 (mm)	σ_0 (MPa)	m_σ
1	3640	8.5

Thus, the SIF induced by a surface defect of size a in a fibre subjected to a stress σ can be calculated using classical elasticity theory:

$$K = \sigma \cdot Y\sqrt{a(t)} \tag{3.6}$$

where Y is the shape coefficient associated with the crack assumed to be constant throughout the propagation. It is considered that $Y = \sqrt{2\pi}$ for penny-shaped crack with small extension as compared to the system size. The largest surface defect (whose initial size is denoted with a_0) is responsible for fibre failure in quasi-static tensile testing as well as in static fatigue. During quasi-static loading, the SIF reaches the Critical Stress Intensity Factor (CSIF), denoted with K_c, at the largest surface defect when the applied stress reaches the strength of the fibres, denoted as σ_R. Therefore, the initial size of the largest surface defect is obtained, for any given strength, by:

$$a_0 = \left(\frac{K_c}{\sigma_R Y}\right)^2 \tag{3.7}$$

Similarly, if the fibre is stressed at $\sigma < \sigma_R$, there exists a critical defect size $a_c > a_0$ for which the SIF reaches the CSIF:

$$a_c = \left(\frac{K_c}{\sigma Y}\right)^2 \tag{3.8}$$

In Fig.3.7 is represented the adopted scheme for the defect growth in the fibre and in Fig.3.8 the silica growth representation under unidirectional problem assumption.

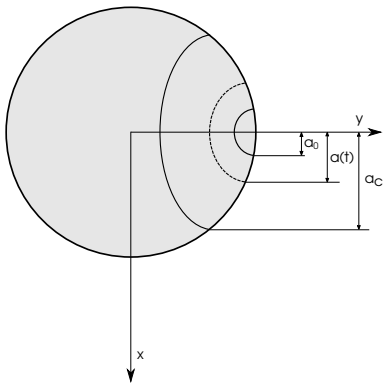

Figure 3.7: Scheme for the SCG in fibres.

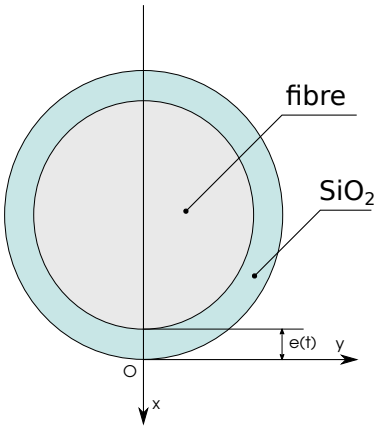

Figure 3.8: Unidirectional problem illustration of silica layer growth for fibres.

By defining the correlation between CSIF and a sub-critical stress intensity factor (SCSIF), which depends on temperature and reaction rate, and by solving the relative diffusion-reaction problem at the crack tip of the fibres, the following differential problem is obtained whose solution is the fibre break time denoted here as t_R [56]:

$$\begin{cases} \dot{a}(t) = \dfrac{1}{(\lambda K_c)^{1/n}} \cdot \dfrac{k \cdot C}{(1 + k \cdot e(t)/D)} \cdot \sigma^{1/n} Y^{1/n} \sqrt{a(t)}^{1/n} \\ \dfrac{de}{dt} = -\dfrac{\rho}{M} \cdot \dfrac{k \cdot C(t)}{(1 + k \cdot e(t)/D)} \\ e(t=0) = 0 \\ a(t=0) = a_0(\sigma_R) \\ a(t=t_R) = a_c(\sigma) \end{cases} \tag{3.9}$$

The two differential equations respectively describe the evolution of the defect size and the silica layer over time. The diffusion coefficient of oxygen in silica is assumed to be Arrhenius-dependent in temperature, as well as the reaction rate coefficient:

$$D_{O_2/SiO_2} = D_0 \cdot exp\left(-\frac{{E^d}_a}{RT}\right); \qquad k = k_0 \cdot exp\left(-\frac{{E^k}_a}{RT}\right); \tag{3.10}$$

where ${E^d}_a$ and ${E^k}_a$ are the activation energies. C represents the oxygen concentration at the crack's tip, σ is the load applied on the fibre, and ρ and M are respectively the density and the mass of silica. In this model (Eqs. (3.9)), there are two parameters for calibration, λ and k. In [56], these parameters were calibrated using the experimental data shown in [37] regarding Hi-Nicalon fibres. Moreover, in [56] only constant loading and environmental conditions have been investigated.

Calibration of the model

The sub-critical crack model described has been coded, revealing some inconsistency concerning the treatment of dimensions in the original publication. An incongruity of the unit of measure adopted in the original paper has led to an inexact calibration of the parameters involved. For this reason, we have re-calibrated the model, and we report here explicitly the steps of this calibration. First of all, the analytical solution of the problem has been derived in case of constant oxygen concentration (for more details see Appendix A.2). In this particular case, the rupture time is:

$$t_R = \left(\frac{M}{2D\rho C}\right)\left[\left(\frac{2n}{2n-1}\left(a_c^{\frac{2n-1}{2n}} - a_0^{\frac{2n-1}{2n}}\right)\frac{\rho}{M(\frac{\sigma Y}{\lambda K_c})^{1/n}} + \frac{D}{k}\right)^2 - \left(\frac{D}{k}\right)^2\right] \tag{3.11}$$

with $C = \frac{p_{O_2}}{RT}$. The analytical solution has been then used to re-parametrize the model with the experimental data of [37] as follows:

- It has been chosen to calibrate the problem considering only the value of λ to avoid the dimensional inconsistency found in [56]:

$$\lambda = 1.12\left[\left(\frac{mol}{m^3}\right)^n\right] \tag{3.12}$$

- The value of k_0 remains unchanged. The reaction coefficient then changes automatically with temperature through the Arrhenius-dependence.

The experimental reference data provided in [37] and used in [56] to validate the model were referring to the lifetime of Hi-Nicalon fibres in the case of constant loading and environmental condition. The same experimental data have been used to calibrate the analytical formula obtained in Eq. 3.11, as is shown in Fig.3.9.
The different calibration causes a slightly shifted curve with respect to the one obtained in the original work. Finally in Fig. 3.10 the perfect agreement between the results calculated with the newly-calibrated model analytically and numerically is shown.
Another element of comparison concerning the evolution of the layer of SiO_2 around the fibre w.r.t. the experimental results given in [5] for different temperatures , is provided in Fig. 3.11.
In [56] were also presented results concerning the lifetime of the Hi-Nicalon fibre bundle in function of the value of the oxygen partial pressure, observing that the failure time of a fibre tow is close to the one related of a particular fibre, called the critical fibre (i.e. the fibre with 5% failure probability). The comparison of the predicted and experimentally observed fibre bundle lifetimes as functions of the partial oxygen pressure is reported in

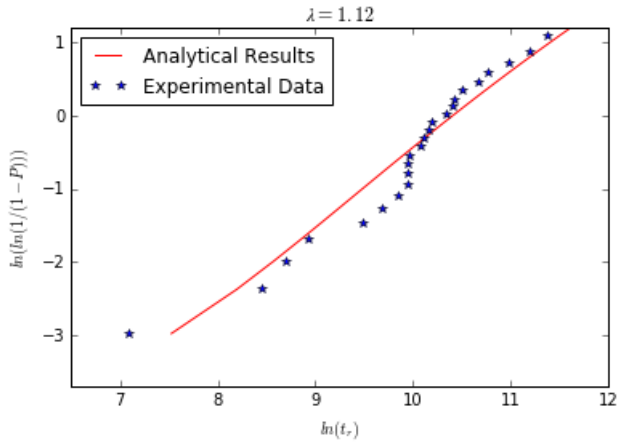

(a)

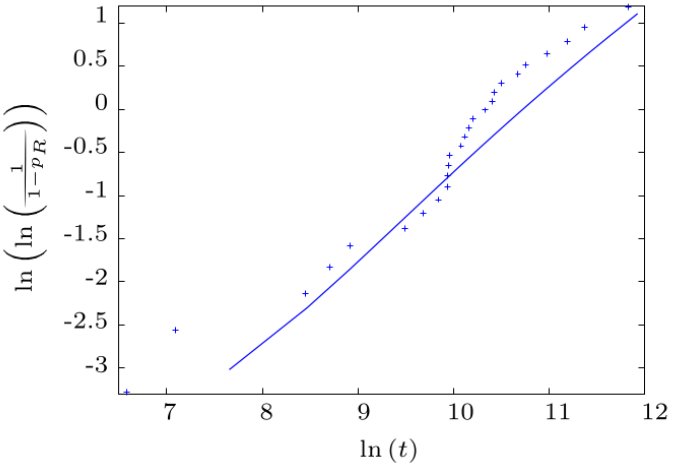

(b)

Figure 3.9: Cumulative lifetime probability distributions of the fibres under constant mechanical and environmental loading: analytical model 3.9(a) compared to experiments [56] and model in [56] 3.9(b) at $T = 773$ K and $\sigma = 1500$ MPa.

Fig. 3.12.

3.4 Sensitivity analysis

In the previous section, the model for the sub-critical propagation of defects in ceramic fibres has been described. A certain distribution of the defects along the fibre of given length had been considered subjected to a tensile stress that followed the Weibull law. From Griffith's law for the stress intensity factor (Eqs. 3.6-3.8), the initial size of the defect a_0 and critical size of the defect a_c were obtained and the sub-critical stress intensity factor was modeled as a function of the temperature, the reaction flux to the tip

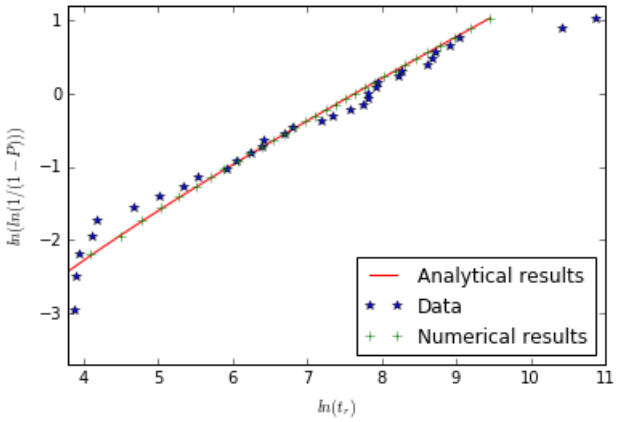

Figure 3.10: Cumulative lifetime probability distributions of the fibres: newly-calibrated analytical vs. numerical model $T = 1073$ K $\sigma = 1100$ MPa.

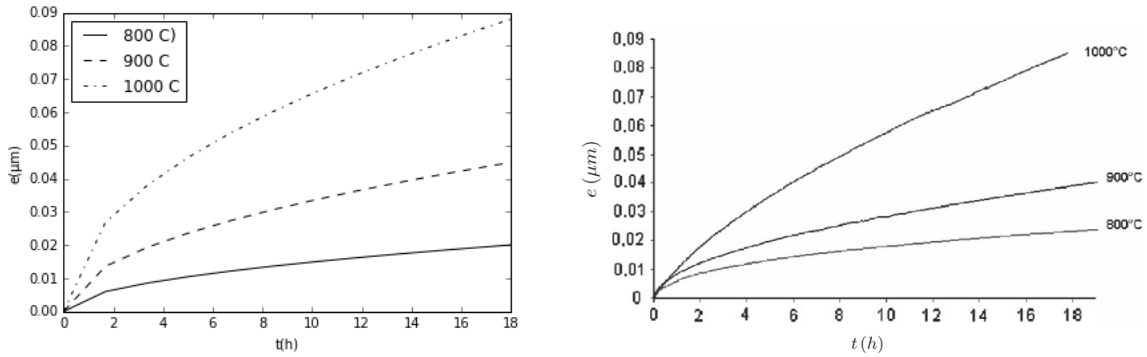

(a) Analytical model

(b) Experiments [5]

Figure 3.11: Thickness of the oxide layer as a function of time at various temperatures.

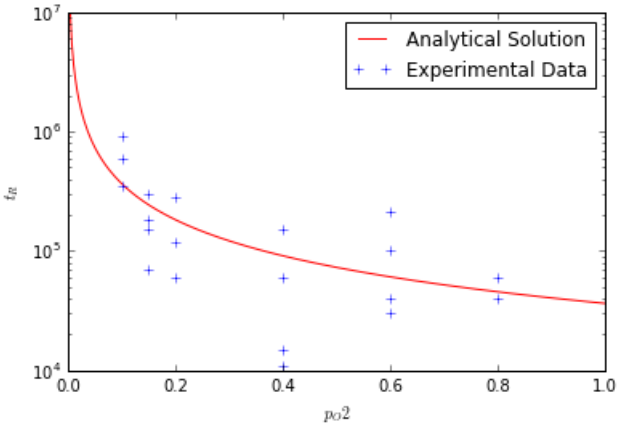

Figure 3.12: Hi-Nicalon fibre tow lifetime as a function of oxygen partial pressure at $T = 773$ K and $\sigma = 1000$ MPa.

and of course the critical stress factor. It has been started from classic fracture mechanics and solving a diffusion-reaction problem with as unknown the oxygen concentration and

the oxygen flux at the crack tip. The effect of silica oxide's growth around the fibre has been then added, and the related diffusion-reaction problem has been solved. The system of equations found is Eqs. 3.9 and has as a solution the breaking time of the fibre. It is important to highlight that this system contains two parameters, k and λ, which have been calibrated through the experimental data. If it is considered that the oxygen concentration is a constant parameter then it is possible to analytically derive the solution which is given by Eqs. 3.5, 3.7, 3.10 and 3.9. If the oxygen concentration is not constant, the solution must be obtained numerically. There is consequently a question mark over how the uncertainty of the input parameters can be propagated throughout the model, giving a strong contribution to the variability of the model's response. Let us consider a set of input variables $(x_1, x_2, ..., x_M)$ described by an input vector $\mathbf{x}$. The model response y is described defining a mathematical model $M(\mathbf{x})$ such that:

$$y = M(\mathbf{x}) \tag{3.13}$$

In particular, the model's results can be as highly correlated to an input parameter as small changes in the input cause significant output changes. Therefore a sensitivity analysis of the proposed model has become necessary to investigate the degree of the related variability and assure the stability of the model. Together with the identification of the inputs and the effects on the outputs, the sensitivity analysis leads to the possibility of neglecting the parameters detected as unimportant in order to reduce the computational cost and simplify the model. Numerous approaches are available nowadays to perform sensitivity analysis. Broadly speaking we can either look at the correlation of samples of the input parameters with samples of the output, at the value of partial derivatives of the model or at given point or directly at the distribution of the model output. More specifically, global sensitivity analysis aims at decomposing the variance of the model output in terms of contribution of each single input parameter or combinations. In particular, in this work the Morris method and to the Sobol' indices, in particular to the Sobol' indices evaluated through the Monte-Carlo method, it has been considered. Both these methods are part of the so-called screening methods, which are methods that provide a qualitative ranking of the importance of the input variables w.r.t. the model response.

3.4.1 Sobol' indices for sensitivity analysis

Sobol' indices are computed defining the expansion of the computational model into summands of increasing dimension, as reported below:

$$y = f_0 + \sum_{i=1}^{p} f_i(x_i) + \sum_i \sum_{j>i} f_{ij}(x_i, x_j) + .. + f_{1,2,..,p}(x_1, x_2, .., x_p) \tag{3.14}$$

where p represents the number of the input variables in the model. Analogously, the total variance of the model is described in terms of the sum of the variances of the summands:

$$Var(y) = \sum_{i=1}^{p} V_i(y) + \sum_i \sum_{j>i} V_{ij}(y) + .. + V_{1,2,..,p}(y) \tag{3.15}$$

The expression of $V_i(y)$ and $V_{ij}(y)$ in the Eq. 3.15 are defined as follows:

$$V_i(y) = Var[E(y|x_i)]; \qquad V_{ij}(y) = Var[E(y|x_i x_j)] - V_i - V_j, ..; \tag{3.16}$$

This variance decomposition leads to a natural definition of the sensitivity measures. In fact, looking at the relative contribution of the i^{th} variable to the total variance of the model it is possible to define the so-called first order sensitivity index:

$$S_i = \frac{V_i(y)}{Var(y)} \tag{3.17}$$

It represents the effect of the only i^{th} variable on the variation of the model's output. In the same way, considering the effect of the interaction of two or more variables on the output's response, the high-order sensitivity indices are defined. For example, the expression of the second order index, is written as below:

$$S_{ij} = \frac{V_{ij}(y)}{Var(y)} \tag{3.18}$$

Finally, considering the properties that the Sobol' indices possess, it is possible to define the so-called total sensitivity index related to the variable x_i:

$$S_i^T = \sum_{\{1,..,s \supset i\}} S_{i_1,..,i_s} \tag{3.19}$$

It is the sum of all the sensitivity indices which involve the i^{th} variable. In particular, the terms of variance described in the Eq. 3.15 can be calculated using the Monte-Carlo method using the estimators here reported:

$$\hat{f}_0 = \frac{1}{N}\sum_{n=1}^{N} f(x^n);$$

$$\widehat{Var}(y) = \frac{1}{N}\sum_{n=1}^{N} f^2(x^n) - \hat{f}_0^{\,2}; \tag{3.20}$$

$$\widehat{Var_i}(y) = \frac{1}{N}\sum_{n=1}^{N} f(x^n{}_i, x^n{}_{\sim i}) f(x^n{}_i, x'^n{}_{\sim i}) - \hat{f}_0^{\,2};$$

3.4.2 Morris sensitivity measure parameters

The idea on which the Morris method is based is the creation of a grid of dimensions equal to the number of input parameters, in which it is possible to perturb one by one its points with a certain value Δ. For sake of simplicity, let us consider two parameters, x_1 and x_2, together with the associated grid shown in Fig. 3.13.

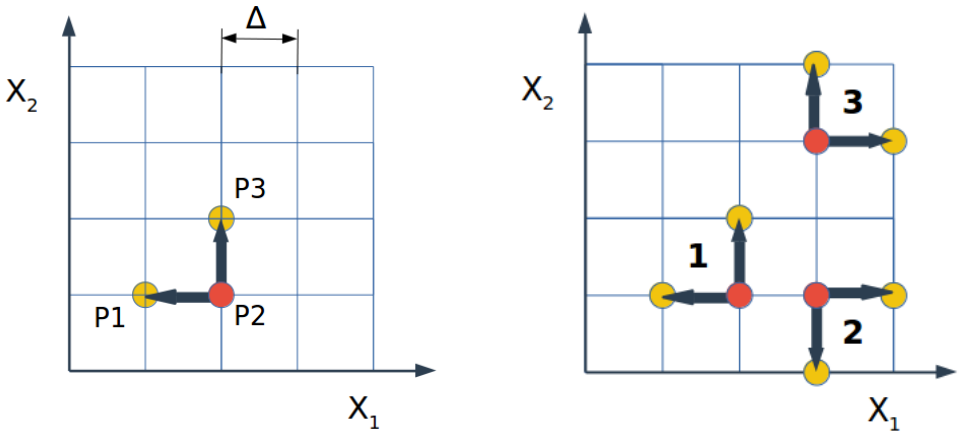

(a) Finite differences associated to a single point

(b) Three points perturbations

Figure 3.13: Two-dimensional Morris' grid scheme.

Perturbing a certain point of the grid with a Δ value both for the x_1 and x_2 parameters, it is possible to calculate the finite differences d_{x_1} and d_{x_2} associated with the respective parameter:

$$d_{x_1} = \frac{f(P2) - f(P1)}{\Delta}; \qquad d_{x_2} = \frac{f(P3) - f(P2)}{\Delta}; \tag{3.21}$$

Repeating this operation R times, with R the number of grid points, two vectors, representing the finite difference for each parameter calculated in every point of the grid, are obtained:

$$\{d^i{}_{x_1}\}_{i=1,\dots,R}; \qquad \{d^i{}_{x_2}\}_{i=1,\dots,R}; \tag{3.22}$$

From the Eq. 3.22 it is possible obtain the mean and the standard deviation values for each parameter:

$$\mu_i* = E(|d_{x_i}|); \qquad \sigma_i = \sigma(d_{x_i}); \tag{3.23}$$

The latter values, shown in Eq. 3.23, represent a sensitivity measure. In particular, high value of μ for the i^{th} parameters means that the model is extremely sensitive to the variation of such parameter. Instead, standard deviation σ measures both the interaction between the variables and non-linear effects. Unfortunately, the distinction between the two cases is impossible.

3.5 Sensitivity analysis on the slow crack growth model

In Fig. 3.14 is represented the flow chart for the adopted uncertainty quantification analysis. Starting with a certain number of input variables, the related probability density functions with specific bounds or moments are assigned. Then, the sample, which has the dimension of the number of the input variables and constituted of N design points, is constructed. For each sampling point the response of the model is calculated and, finally, the probability density function of the model response is evaluated together with the sensitivity of the model to the input parameters.

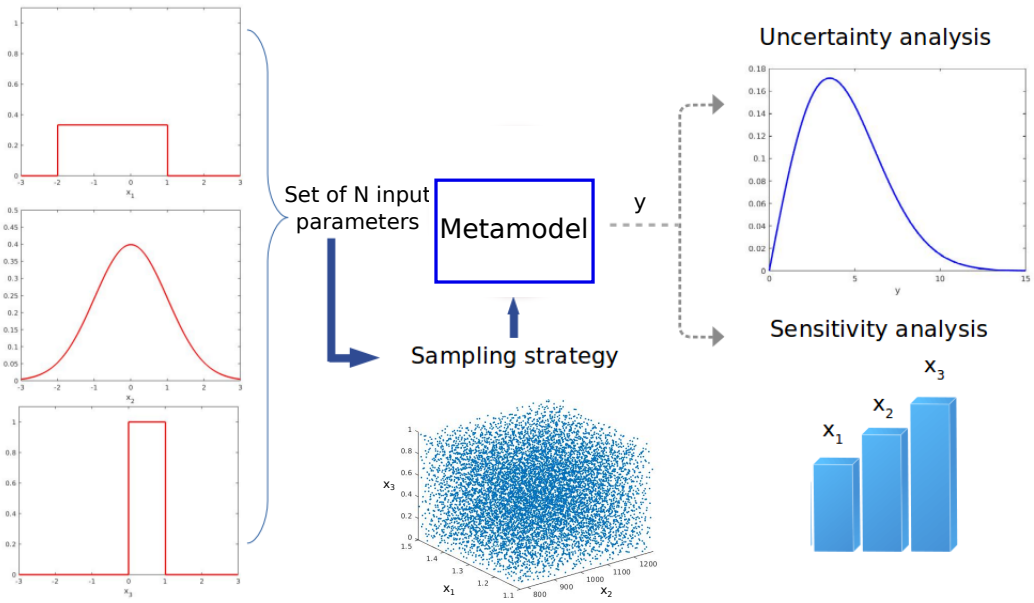

Figure 3.14: Uncertainty quantification strategy.

For this purpose, the UqLab framework [70], developed for uncertainty quantification, has

been used. First of all, the six-parameters analytical formula obtained to evaluate the time of rupture of a single fibre subject to the static-fatigue phenomenon (Eqs. 3.5, 3.7, 3.10 and 3.9) has been considered. The list of the involved parameters and their related boundary values is reported in Tab. 3.2.

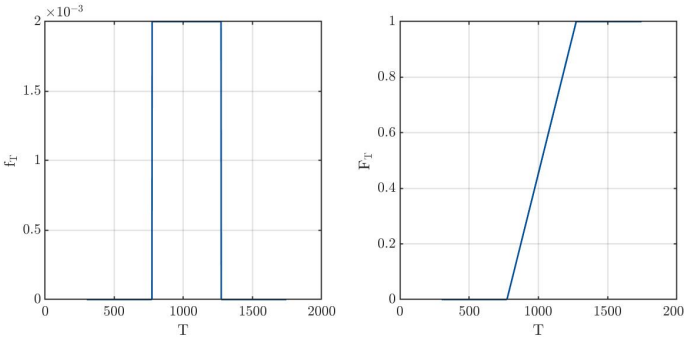

(a) PDF and CDF of temperature T

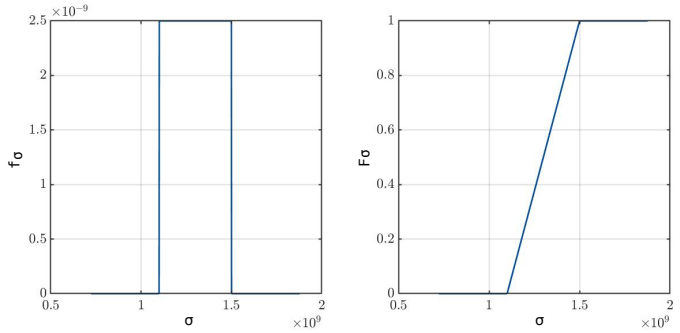

(b) PDF and CDF of applied load σ

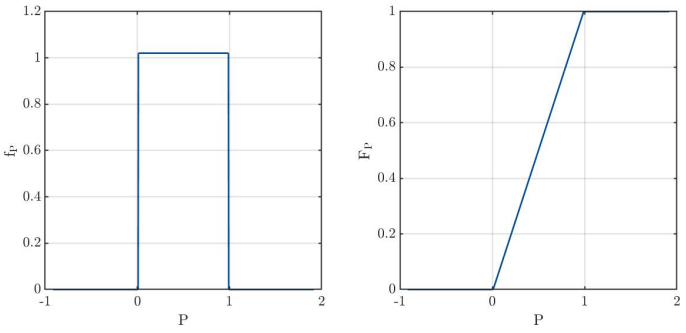

(c) PDF and CDF of failure probability P

Figure 3.15: Probability density functions f_{x_i} and cumulative distribution functions F_{x_i} of the inputs parameters.

Actually, observing the equation (3.11), the primary parameters are 17 in total (σ, M, ρ, D_0, E_a^d, k_0, E_a^k, T, P_{O_2}, n, λ, Y, L_O, L, m_σ, σ_0 and σ_R or similarly P). As can be seen from Tab. 3.2, only 6 parameters were chosen as input for the sensitivity study. This

choice was made for the following reasons:

- the effect of the fibres strength distribution with a fixed distribution was studied, therefore only one parameter of the Weibull distribution was considered, such as P (hence with m_σ, L_0, L and σ_0 constants). Furthermore, a given defect shape (Y constant) was taken into account.
- regarding D and K, which are expressed by the Arrenhius-type law, only the calibrated coefficients was changed, such as D_0 and K_0 (thus E_a^d and E_a^k constants).
- for n and λ, the calibration performed on the analytical formula (3.11) in the previous section is applicable.
- the variation of mass M and density ρ could also be evaluated, but these parameters were maintained constant in order to confine the sensitivity study to the external parameters (σ, T and p_{O_2}), fibres strength (P), diffusion (D_0) and kinetics (k_0) of the processus.

For each of the variables, uniform probability density functions f_{x_i} and the respective cumulative distribution functions F_{x_i} have been assigned, as is shown in Fig. 3.15.

Table 3.2: Modeling of parameters for the slow crack growth problem.

Name	Distribution	Parameters	Description
T	Uniform	[773.15 - 1273.15]	Temperature [K]
σ	Uniform	[1100 - 1500]	Applied stress [MPa]
D_0	Uniform	$[2{\cdot}10^{-8}$ - $3{\cdot}10^{-8}]$	Diffusion coefficient of O_2 in SiO_2 $[\frac{m^2}{s}]$
k_0	Uniform	$[1.47{\cdot}10^2$ - $2.47{\cdot}10^2]$	Reaction coefficient of O_2 with SiC $[\frac{m}{s}]$
p_{O_2}	Uniform	[21278.25 - 100278.25]	Oxygen partial pressure [Pa]
P	Uniform	[0.01-0.99]	Fibres failure probability

3.5.1 Results

In Fig. 3.16 are reported the sensitivity analysis carried out in terms of Sobol' indices. In particular, the latter has been calculated up to order three.
Considering the total Sobol' indices of each input parameter, represented in Fig. 3.17(a), there are only four variables of six whose global effects on the system's response can be deemed relevant: the temperature, the applied load, the failure probability of the fibre and as of last the partial oxygen pressure. As stated above, these quantities include both

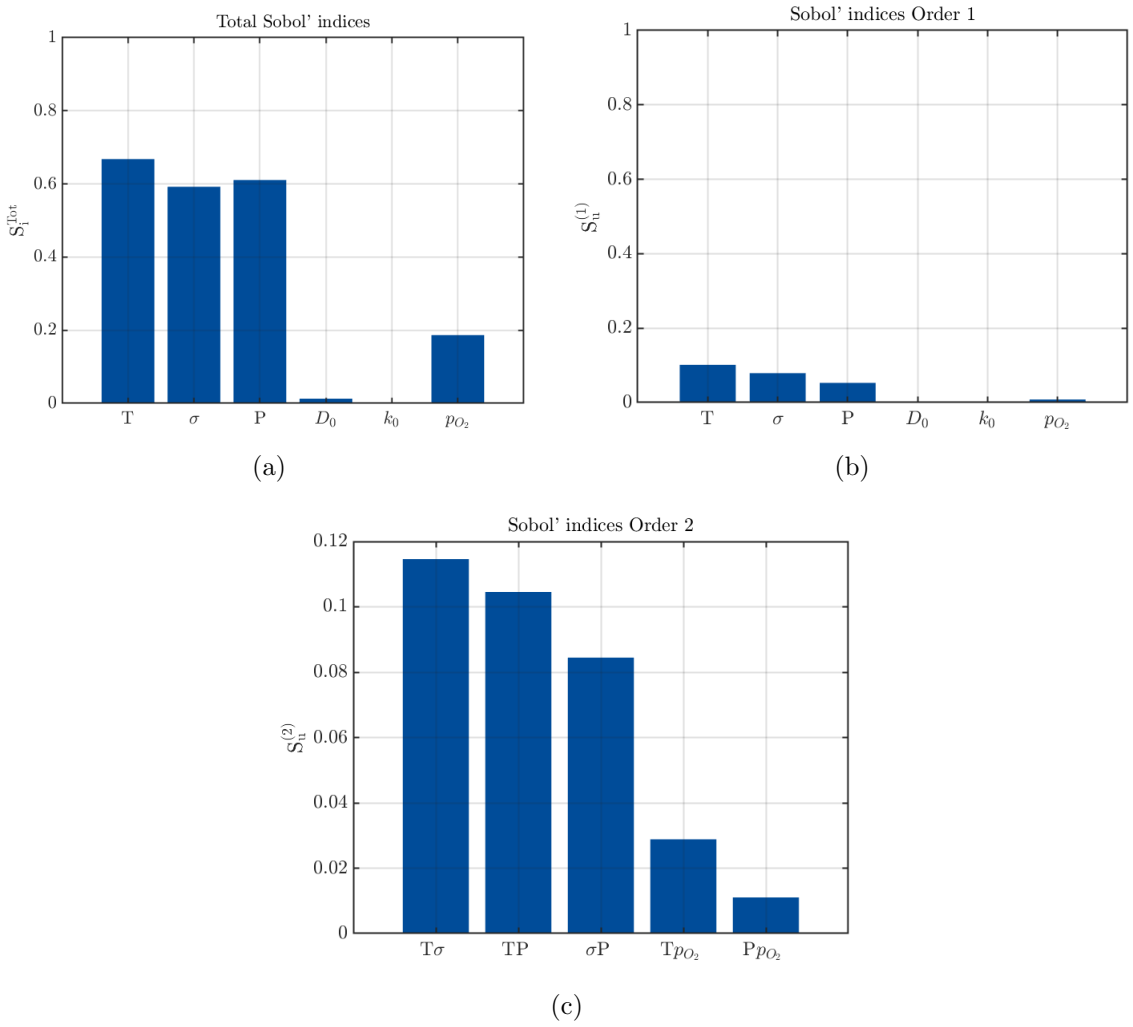

Figure 3.16: Sensitivity Sobol' indices for the analytic time to rupture model related to the SCG.

the direct and the combined variables' effects. Indeed, the direct effect of every single parameter on the model is given by the first Sobol' indices in Fig. 3.16(b). It is evident that only the temperature, the applied load and the failure probability of the fibre produce a direct strong variation of the time to rupture for the SCG model and most importantly, the crossed interaction between the temperature and the other two parameters (σ and P), as is shown in Fig. 3.16(c).

In order to have insight into the crossed mechanism between the most influent variables, the same analysis has been performed considering only the temperature, the failure probability and the applied load as parameters for the sensitivity study. The parameters description is reported in Tab. 6.2.

As the sensitivity results show in Fig. 3.17, the hierarchy of the three variables has remained the same and the predominant effect of the interaction of temperature with the

Table 3.3: Modeling of reduced parameters for the slow crack growth problem.

Name	Distribution	Parameters	Description
T	Uniform	[973.15-1273.15]	Temperature [K]
σ	Uniform	[1100-1500]	Applied stress [MPa]
P	Uniform	[0.01-0.99]	Failure probability

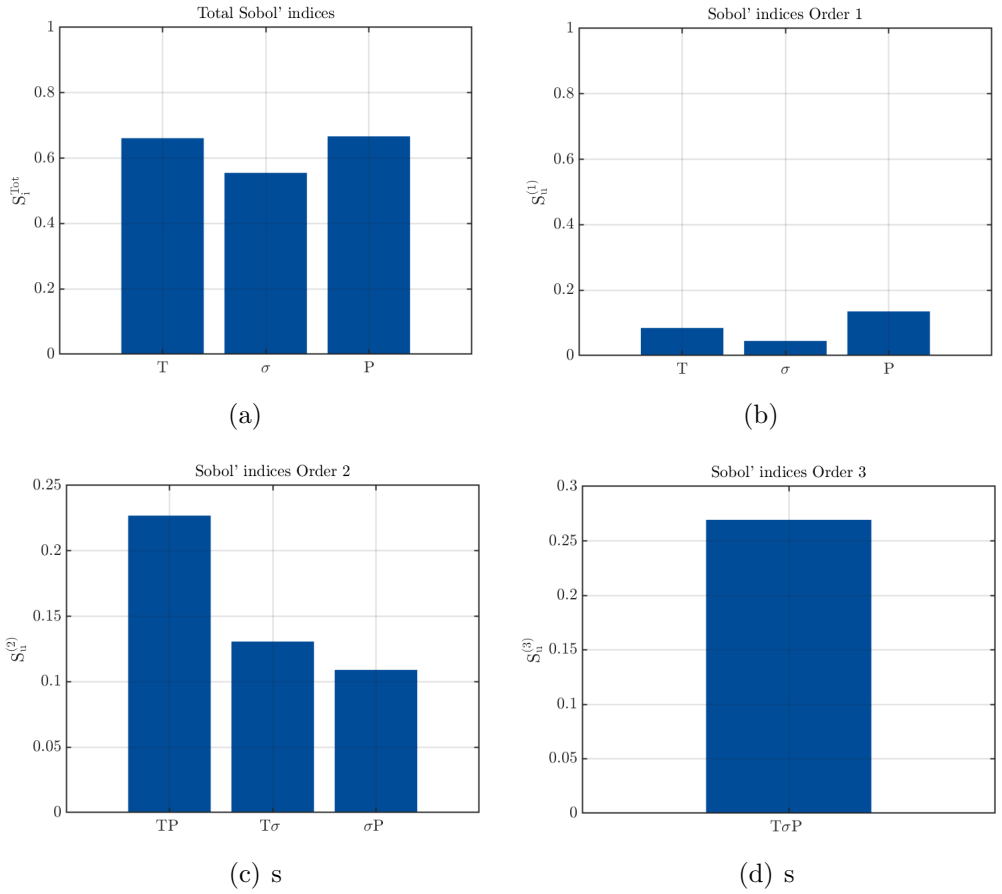

Figure 3.17: Sensitivity Sobol' indices for the analytic time to rupture model related to the SCG (reduced parameters model).

remaining variables has been confirmed. In particular, the combined effect of all the three parameters is the strongest source of variability of the model's output (Fig. 3.17(d)). In Fig. 3.18 is reported the sensitivity analysis based on Morris' method on the $\mu - \sigma$ plane. As mentioned above, points far away from the origin in the μ direction are relevant. In this case, the hierarchy of importance of the three parameters is the same as found in Sobol' sensitivity analysis. In particular, the temperature and the applied load are also far away from the origin in the σ direction and, consequently, represent variables with significant non-linear contributions and those in which interactions are important. This

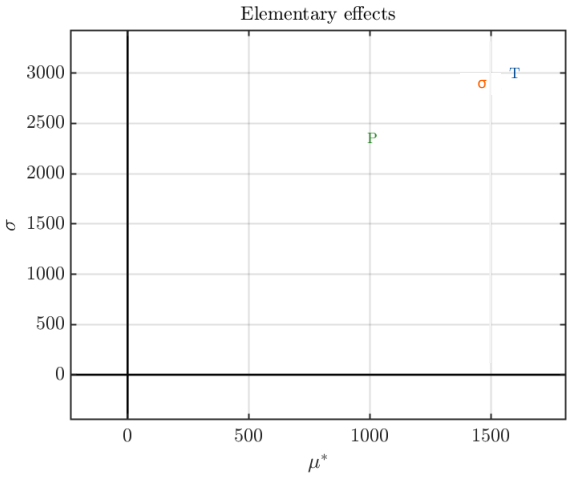

Figure 3.18: Morris plot for the 3-dimensional SCG problem.

result perfectly agrees with the one obtained in Fig. 3.17.

3.6 Chapter summary

In this chapter the slow crack growth model used to predict the fibres progressive degradation is illustrated and re-calibrated using a particular exact solution and integrated numerically in the general case. The re-calibrated model is in general agreement with both the experimental data and the original model in terms of both lifetime dependence on external conditions, and temporal evolution of the oxygen layer on the fibre surface. The sensitivity analysis was carried out through the calculation of the Sobol' and Morris indices on the resulting analytical formula, showing the stability of the model as a result of the variation of the parameters concerning the diffusive/kinetic aspect. However, the model is strongly influenced by parameters that are given *a priori*, such as temperature, applied stress and fibre strength. The sensitivity analysis, together with the uncertainty quantification study, leads to the possibility of neglecting the detected unimportant parameters to reduce the computational cost and simplify the model with a view toward the upscaling problem.

Chapter 4

Lifetime prediction of a SH-CMC mini-composite

Contents

4.1 Introduction

When the material is subjected to a stress greater than the strength of the matrix, it exhibits cracks. The cracking scenario of a CMC material has been extensively discussed in [30, 43, 53, 55, 59]. Initially, the crack is generated from a macro-pore and subsequently propagates through the inter-yarns matrix in an orthogonal direction with respect to the main direction of the applied load. Once the crack reaches the fibres, it is deflected by the action of the interphase present between the fibres and the matrix itself, forming a certain decohesion zone. In a second moment, the intra-yarns matrix is attacked by the crack starting from a micropore, moving in a longitudinal and transverse direction considering the respective direction of the fibres. Since the cracking mechanism is very complex regarding CMC woven fabrics in their entirety, unidirectional models are generally used in order to isolate the specific mechanisms [11, 77]. In the present thesis, the case study concerns only static loads, therefore cyclic loads and fatigue degradation are not considered ([26, 65, 90, 105]). As already mentioned in the chapter 2 as oxidising environment, dry air was considered (for degradation of fibres in a humid environment see [35, 103] and for oxide volatilisation in the case of SH-CMC see [6, 65, 73, 102]). In addition, temperatures below 1000°C were investigated for which the creep phenomenon is negligible (see [26, 105]). The chapter is structured as follows: the first part is devoted to an illustration of the main failure mechanisms affecting mini-composites and the main hypotheses that are currently proposed. Thereafter, the model used to calculate the failure of the mini-composite analysed is described and motivated. The final part of the chapter is dedicated to the results concerning the mini-composite lifetime calculated through the coupling of the models relating to self-healing and oxidation in the crack presented in chapter 2, the sub-critical propagation model for the fibres illustrated in chapter 3 and the aforementioned mechanical model. The results were analysed in terms of the variation in lifetime as a function of acting stress, temperature and fibres strength distribution in the mini-composite.

4.2 Failure mechanisms in mini-composites

To study the subsequent failure of the constituents of the mini-composite, several approaches have been proposed [7, 18, 63, 67, 72, 95]. Two scenarios can occur when a crack reaches the fibre, depending on the intensity of the fibre/matrix bond [1]. If the fibre/matrix bond is strong, then the crack will propagate through the fibre. If, conversely, the fibre/matrix bond is weak, the crack will be deflected in the proximity of

the fibre in a longitudinal direction. Therefore, a fibre-matrix decohesion and shear load transfer between the fibre and the matrix can be detected. For this purpose, the interphase placed between the fibre and the matrix assumes a key role in conferring ductile and non-fragile behaviour to the entire composite. If the case of a single crack is considered, the applied load is carried entirely by the fibres in correspondence of the crack plane and is transferred to the matrix through sliding at the fibre/matrix interface. Therefore, the pull-out lengths of the fibres are zero [95] and, according with the shear-lag assumption, the stress profile has a linear decreasing trend starting from the plane where the crack is located. Thus, under single-matrix crack conditions, stresses and strains are localised in the proximity of the matrix crack.
The formation of the silica layer around the fibres can cause a decrease in the fracture loads of the bundles due to coalescence between the silica layers of neighbouring fibres. Particularly for Hi-Nicalon fibres, the coalescence of the silica oxide layers is the predominant interaction occurring between the fibre bundles [58]. In particular, as shown in Fig. 4.1, this phenomenon is temperature-dependent, having a major impact on the speed, and thus the size, of silica formation.

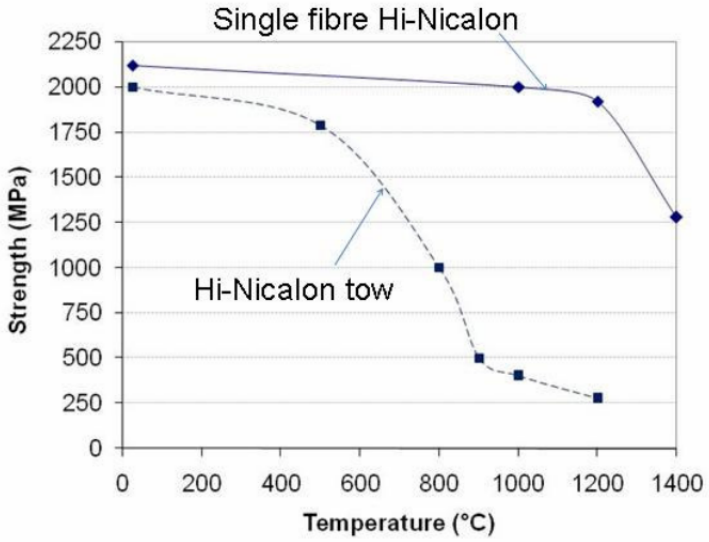

Figure 4.1: Temperature-strength diagram for tows and Hi-Nicalon single filament [58].

4.3 Tows lifetime estimation : Global Load Sharing (GLS) and Local Load Sharing (LLS)

In order to identify the ultimate stress of parallel fibre yarns and its redistribution for all sequential failures, two different approaches are considered in the literature: local load

sharing (LLS) and global loal sharing (GLS). In the case of the LLS approach, it is considered that the repartition of the load after the failure of a fibre is, for a certain amount, redistributed to the fibres that are linked to the freshly broken fibre. In the works dealing with this type of approach [9, 82, 84] are therefore present not only a representative geometry of the fibre yarn but also the introduction of parameters such as the percentage of imperfections, and probability laws on stiffness that are difficult to identify as they are variable from one yarn to another. Furthermore, this approach does not provide an analytical solution but requires a numerical strategy to be implemented. The advantage of considering a LLS-type load distribution lies in the possibility of detecting the influence of imperfections in the bundles of fibres, considering that it has been shown in [9] that the greater the interaction between the fibres, the more dispersion of the results on the load at failure. In contrast, the GLS approach does not consider that there are interactions between the fibres. It therefore expects the load to be equally redistributed over all fibres still undamaged. In fact, works [16, 22] that use GLS for the computation of the ultimate tensile stress of the fibres, assume that the fibres are perfectly parallel. The solution obtained in this way is simple and analytical.

4.4 Failure mechanical model

It is known that CMCs have two different damage evolution regimes. The first generally occurs for low-stress values and shows a growth of defects present in the matrix that evolve into a crack in the material. Due to the presence of debonding between matrix and fibres, the crack does not penetrate the fibres. This phase is mainly controlled by the evolution of the defects inside the matrix. The second phase is called tough behaviour and occurs for high loads. During this phase, the tow failure is entirely controlled by the evolution of the defects present in the fibres. However, it has been demonstrated in [19] and [83] that failure stress is controlled by the characteristic fibre strength relevant in the saturated-matrix crack regime. The evolutions of stresses along the fibres and the matrix for an axially loaded fibre bundle are shown in [20].

A simplified version of this description is proposed in this work as shown in Fig.4.2. It is considered that, in the debonding zone, the load is constant and maximum, i.e. there is no load transfer between matrix and fibre, which is a conservative assumption.

Let's consider a mini-composite with a certain length L, surface A and debonded length l_d as illustrated in Fig.4.3. In the zone (1), the effective modulus is:

$$E_1 = v_f E_f + (1 - v_f) E_m \tag{4.1}$$

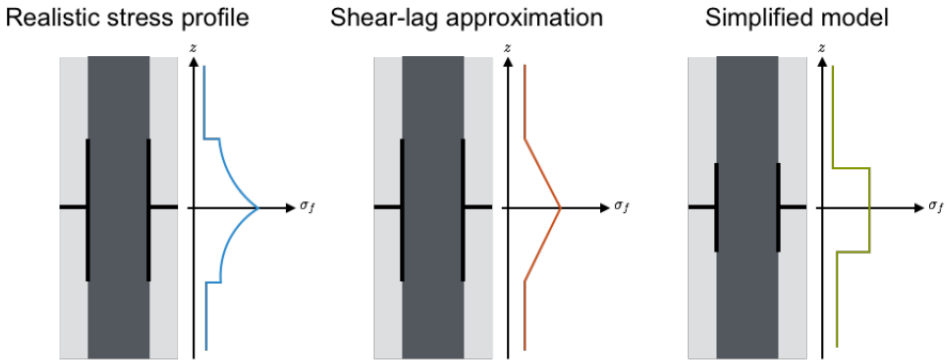

Figure 4.2: Schematic representation of fibre stress profile within the debonded area for different approaches.

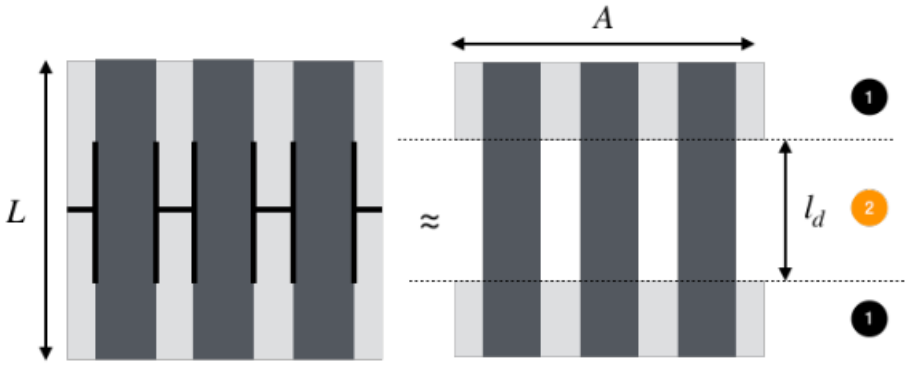

Figure 4.3: Schematic areas of the mini-composite for the estimation of elastic and resistance properties.

in which E_f and E_m are Young's moduli of the fibre and the matrix and v_f represents the fibre volume fraction.

Considering that there is no transfer between the matrix and the fibres, in zone (2) the load is carried only by the fibres. The effective modulus in that zone is given by the following relation:

$$E_2 = \frac{A_f}{A} E_f \tag{4.2}$$

where $A_f = \sum_{i=1}^{n} {A_f}^i$ and ${A_f}^i$ is the cross-section area of the i^{th} fibre and n the number of fibres. Thus considering the 1D rule of mixture of a serie model and the taking the normalized debonded length as $\tilde{l_d} = \frac{l_d}{L}$, the modulus of the minicomposite is simply given by:

$$E_c = (\frac{\tilde{l_d}}{E_2} + \frac{1 - \tilde{l_d}}{E_1})^{-1} \tag{4.3}$$

Considering a tensile load F applied on a mini-composite and using the isostress assumption, each fibre carries a load F_i proportional to its cross-section area A_i:

$$F_i = F\frac{A_i}{\sum_{i=1}^{n_{\text{fibres}}} A_i} \tag{4.4}$$

and therefore its stress is given by:

$$\sigma_f = \frac{F_i}{A_i} = \frac{F}{\sum_{i=1}^{n_{\text{fibres}}} A_i} \tag{4.5}$$

Using these assumptions, the fibres stress only depends on the surface of the actual fibres carrying the load, which we refer to as n_{fibres}. For a load-controlled test, such as a static fatigue test, each broken fibre will increase the load carried by the remaining fibres. In global load-sharing assumptions, the stress acting on the surviving fibres σ, the average strain ϵ and the opening of the crack e_c are calculated as follows:

$$\sigma = \frac{F_0}{(n^0{}_{\text{fibres}} - n_{\text{broken}})S_f} \tag{4.6}$$

$$\epsilon = \frac{F_0}{(n^0{}_{\text{fibres}} - n_{\text{broken}})S_f E_f} \tag{4.7}$$

$$e_c = l_d\frac{F_0}{(n^0{}_{\text{fibres}} - n_{\text{broken}})S_f E_f} \tag{4.8}$$

where $n^0{}_{fibres}$ represents the initial number of fibres.

4.5 Lifetime evaluation strategy for SH-CMCs mini-composites

In this section, the strategy used for the evaluation of self-healing ceramic matrix mini-composite lifetime under static fatigue tests is illustrated. Defining a certain stress σ applied to the mini-composite, the subsequent deformation and opening of the crack is calculated. The oxygen diffusion inside the crack leads to the oxidation processes of fibres and reactive matrix layers. The latter is responsible for the local healing of the crack by the generated oxide. In particular, the simulation involves the resolution of the diffusion-oxidation system in a two-dimensional domain accounting for the average (along the crack width) spreading of the protective oxide. The oxygen that arrives at the fibres must first diffuse through the oxide layer formed around the fibres and then oxidizes fibres. The defects growth on the surface of the fibres is calculated as a function of the

oxygen flux at the latter. We chose to consider the worst-case scenario, i.e. when the maximum oxygen concentration value corresponds to the largest defect on a fibre. The bundle failure time calculated is, thus, conservative. Moreover, the model considers the growth of the silica oxide layer around the fibres and the diffusion of oxygen through it. The variation of the fibre resistance distribution is calculated according to the size of the defect. When a defect reaches the critical size, i.e. when $\sigma_r = \sigma_{fib}$, the fibre breaks and the oxide is spreaded on the new domain. The redistribution of the load over the intact fibres and the subsequent reopening of the crack is calculated. Finally the failure time of the mini-composite is computed as the time at which the critical fibre breaks, causing the failure of the whole bundle.

4.5.1 Results: temperature, applied stress and fibres strength distribution influence

We have investigated the predictive capabilities of the model proposed on the cracked-yarn configuration previously shown in Fig. 2.10 . We have first performed a purely mechanical simulation, i.e. without generating the protective plug. In particular, the simulation was carried out for T = 973 K and applied stress $\sigma = 1$ GPa and a Weibull distribution of fibre strength values. Fig. 4.4(a) shows the failures times of each fibre as a function of the assigned σ_R and fibre-to-tow outer edge distance. As is evident, the sequence of fibre failure is a function only of the initial failure probability distribution and therefore follows the Weibull law introduced above. There is no correlation between the breaking times and the position of the fibres inside the yarn.

Subsequently, the same simulation was repeated introducing the self-healing action. In Fig. 4.4(b), identical environmental and mechanical conditions have been considered. Moreover, the values of the initial distributions of σ_R of the fibres are the same as those chosen in Fig. 4.4(a). The scenario of bundle failure shows that both the sequence and the times of fibres breakage events are dependent on the fibre position in the yarn. This effect is clearly due to the level of oxygen concentration reaching the fibres. As stated above, the oxide allows slowing down oxygen diffusion from the outside towards the tow. To demonstrate this concept, Fig. 4.5 shows the maximum concentration of oxygen on the fibres in the case of fibres closer to the outer domain, which are surrounded by only one sequence of matrix layers, in the case of fibres in the second row, and in the case of fibres placed more internally in the tow. In all cases the oxygen concentration is constant until the crack has been filled by the oxide and then has a rapid drop, which is in agreement with results obtained by other models in literature [2, 15]. Then, the oxygen starts over

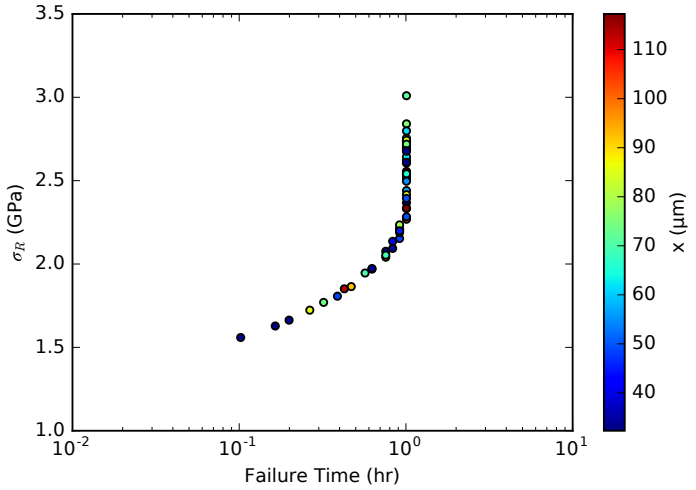

(a)

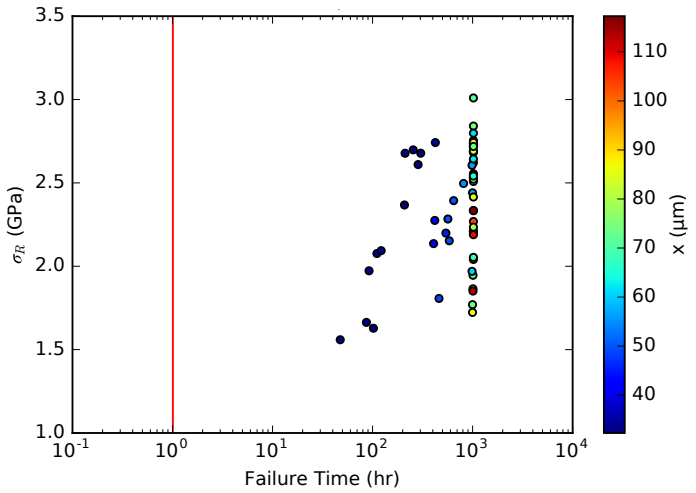

(b)

Figure 4.4: Fibres' failure history in function of their initial strength and distance from the outer boundary at $T = 973$ K and $\sigma = 1$ GPa without (4.4(a)) and with oxide (4.4(b)).

diffusing through the crack at a slower rate and first reaches the fibres closest to the outer edge.

Thanks to the action of the produced oxide, it can be observed that the tow lifetime is longer than the one calculated in the relative non-oxide case reported with the straight line. To illustrate the concept in more detail, Fig. 4.6 illustrates a spatial representation showing the position of the fibres that break during the life of the material under the imposed conditions.

In particular, the strong dependence of fibres' lifetime on their position in the yarn in the

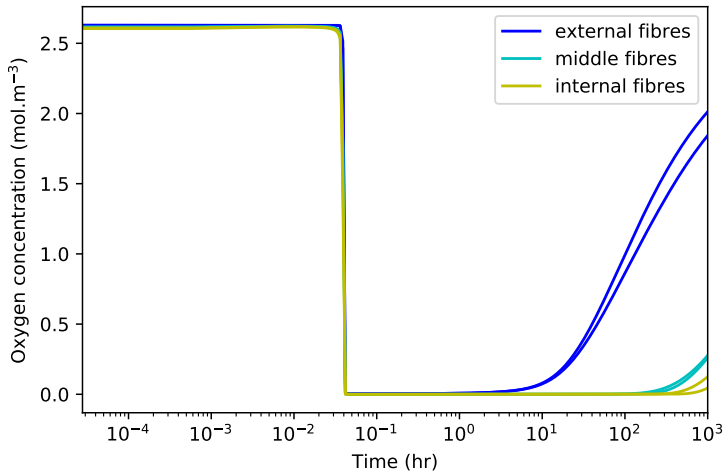

Figure 4.5: Oxygen concentration at the surface of fibres vs. time for $\sigma = 1$ GPa and $T = 973$ K.

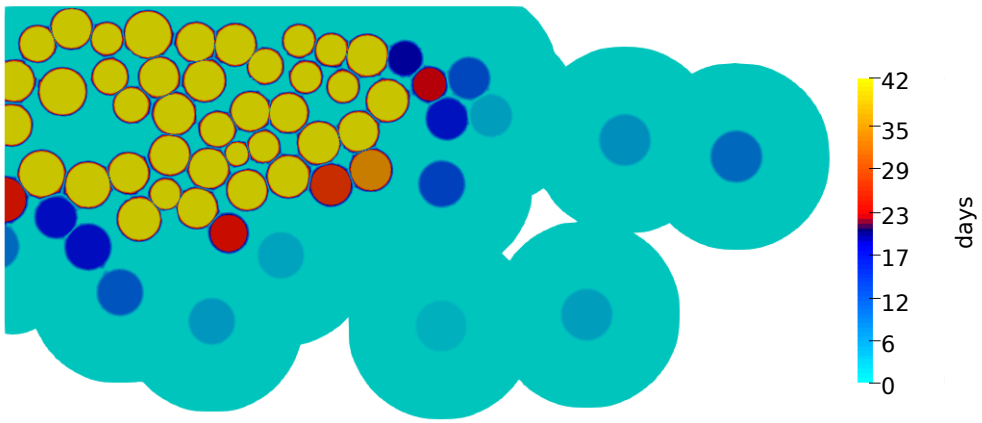

Figure 4.6: Fibres' failure history representation of simulation 4.4(b) in the 2D crack's domain.

case of complete self-healing and on their initial strength in the case of non-healing is evident in Fig. 4.7.

Moreover, Fig. 4.8 provides a more accurate representation of the failure scenario of the first six fibres of the simulation shown in Fig. 4.4(b). Each fibre starts with an initial strength value which continuously decreases as the size of its critical defect increases. The rate of this decrease is dependent on the oxygen concentration reaching the fibre. The more the fibre is subjected to a high oxygen concentration, the faster the propagation of its critical defect. When σ_R of the fibre is equal to the stress, it fails. In this case, the first fibre that breaks is the one with the lowest initial σ_R. Already for the second fibre that breaks the situation is different. This fibre is not initially the second with the lowest

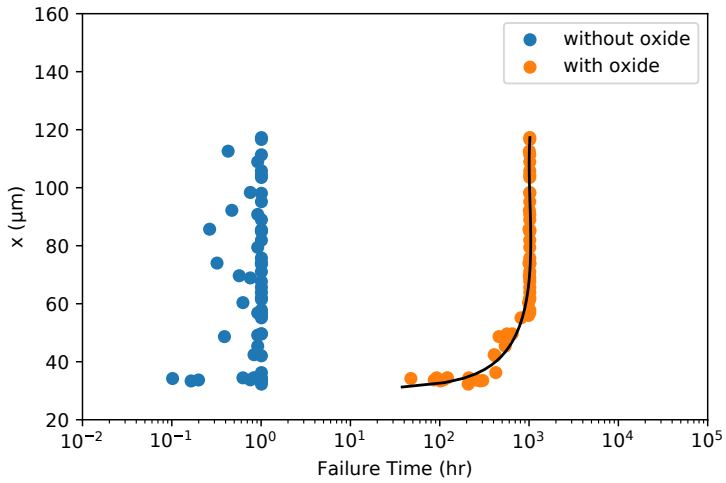

Figure 4.7: Fibres' failure time w.r.t. distance from the outer domain considering the oxide 4.4(b) and non-oxide 4.4(a) simulation at $T = 973$ K and $\sigma = 1$ GPa.

resistance, but it is the third. It breaks before the one with the lowest initial resistance because it has a higher defect propagation rate since it sees a higher oxygen concentration value. Obviously, for each fibre that breaks, the line representing the stress acting on the fibres has a jump due to global load sharing. As soon as a fibre breaks, the oxide instantly fills up the newly created space, allowing oxygen to diffuse there.

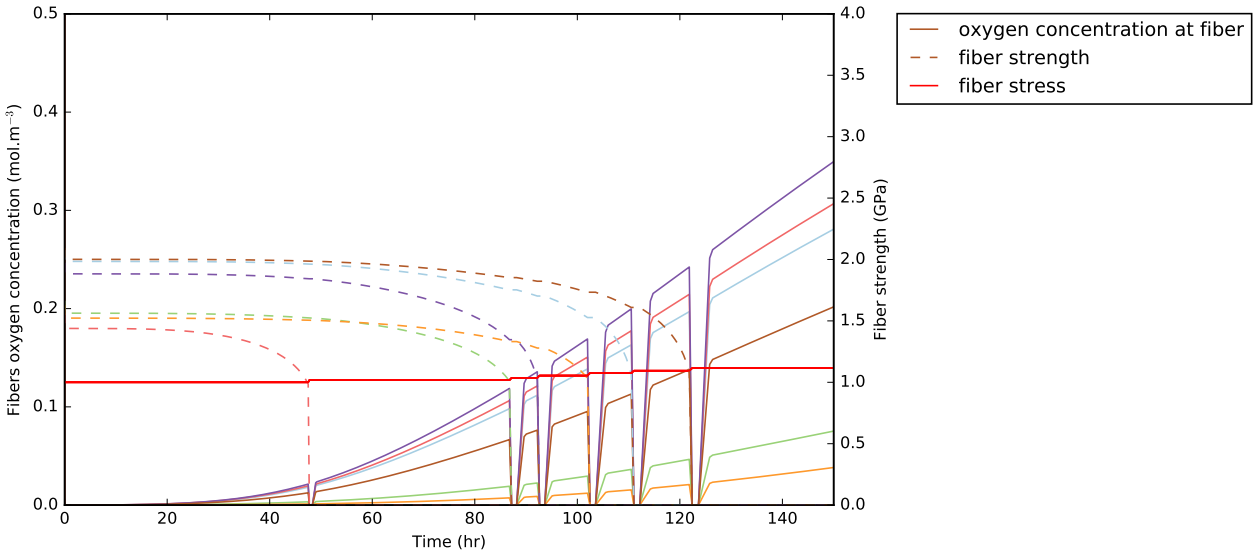

Figure 4.8: Time evolution of fibres' oxygen concentration, strength and applied stress for 4.4(b).

In Fig. 4.9, the evolution of the number of broken fibres over time was analysed for both cases (healing/non-healing). The effect of the oxide is to slow down the growth of the critical defect in the fibres and protect them for a longer time. This result is translated in

different breaking times for the fibres, especially in the final part of the bundle life, when a certain number of fibres are already broken. On the other hand, in the case where there is no plug, the speed of propagation of the defects in the fibres is higher, and therefore there are more fibres that reach breakage in short times.

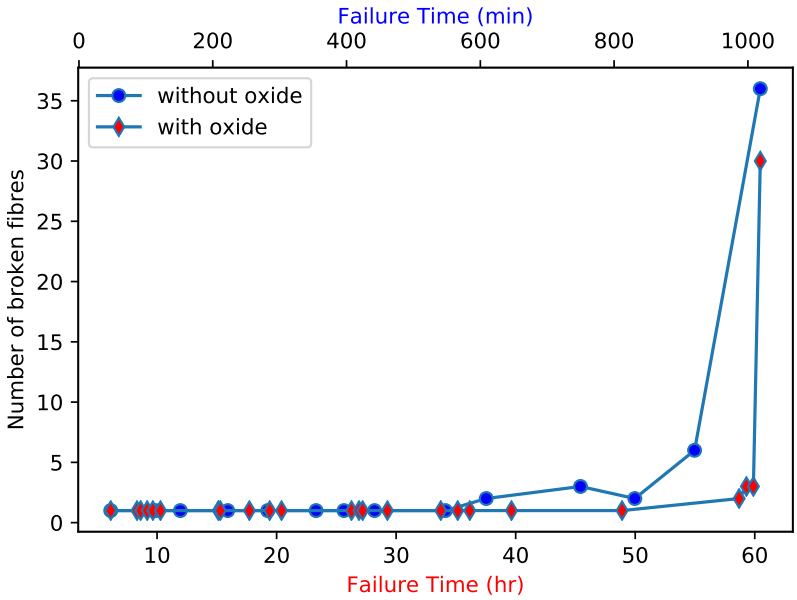

Figure 4.9: Evolution in time of the number of broken fibres for the oxide 4.4(b) and non-oxide 4.4(a) simulation cases. Time scale for non-healing case minutes (upper axis), time scale for healing case: hours (lower axis).

Sensitivity to applied stress and temperature

We have then investigated the effect of the applied stress on the mini-composite failure time. Fig. 4.10(a) shows the failure time results of 50 simulations for each loading condition. All the simulations were carried out considering the same temperature, but with a different realization of the initial strength distribution obeying to the same Weibull law. Note that the breaking time decreases as the load increases, but interestingly, as the load increases, there is a greater dispersion of failure times among the different simulations. If the loading is very high, there is a small margin of variation for the defects in fibres, and therefore it all depends on their initial strength distribution and geometry. The same operation was then done, varying the temperature and maintaining fixed the value of the applied load. Fig. 4.10(b) shows that the failure time remains almost constant for a certain range of temperatures until it drops. Under certain stress and temperature conditions, such as here at 1173 K and at 1 GPa, there is a transition zone. Two different regimes are distinguished. In fact, in this zone, the failure time can reach 1000 hours or just a few seconds. This depends on the time it takes for the oxide to cover

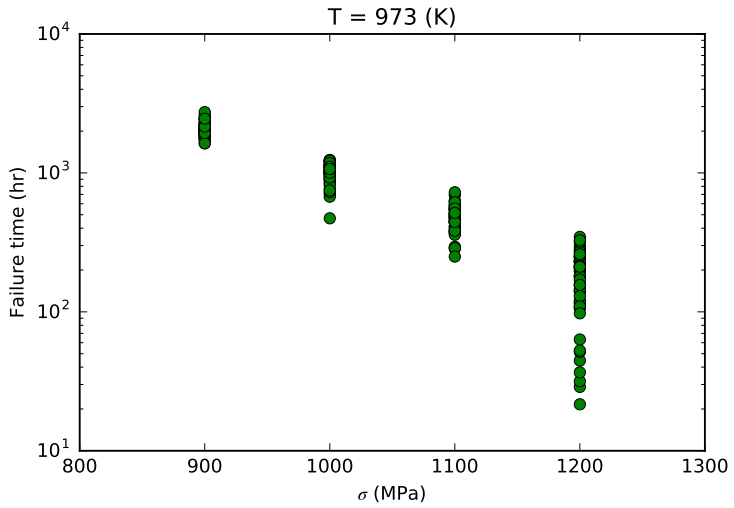

(a)

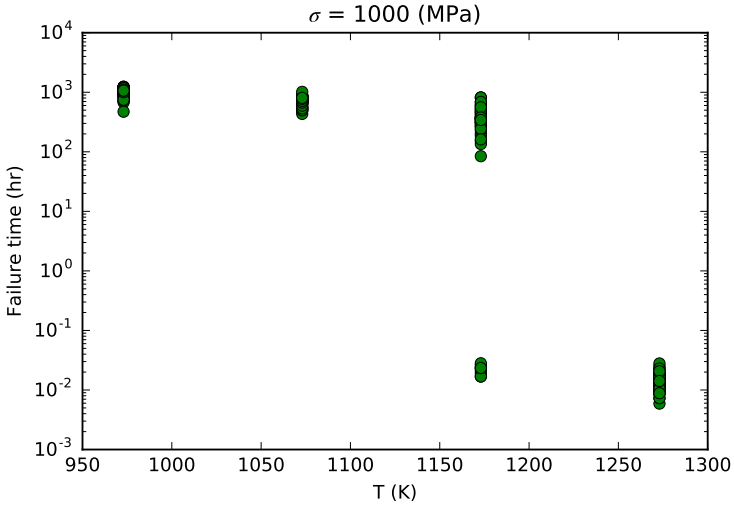

(b)

Figure 4.10: Mini-composite failure time for different load 4.10(a) and temperature 4.10(b) conditions.

the crack. If during this time, the initial distribution of fibres' strengths is such that a sufficient number of fibres are broken so that the applied stress is immediately achieved, then the whole tow will break before the oxide has had a chance to heal the crack. Otherwise, the oxide can play its role, and consequently, the lifetime of the tow is increased by 6 orders of magnitude, as could be expected from the ratio between diffusion coefficients in the liquid and the gas.

In particular, considering a temperature-stress plane, a sector was found in which the bimodal behaviour mentioned above is found, separating the zone of conditions allowing complete healing from the zone of non-healing (see Fig. 4.11).

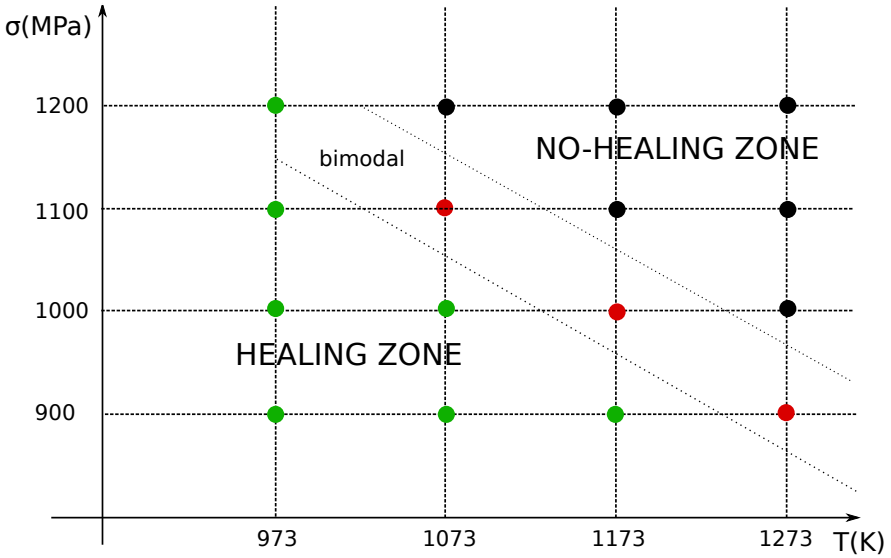

Figure 4.11: Temperature and stress conditions for healing, non-healing and bimodal behaviour for the considered tow configuration 2.10.

To clarify this concept, two simulations in the transition zone conditions found in Fig. 4.10(b) which represent the two different regimes are considered. Fig. 4.12 and Fig. 4.13 show both the evolution of the oxide inside the crack with respect to the crack height and the evolution of the fibre strengths with respect to the applied stress. In Fig. 4.12 it is evident that the oxide fails to plug the crack as the distribution of fibre strengths is such that many of these fail in the first few seconds. Therefore the crack opening increases rapidly according to Eq. 4.8. Fig. 4.13 represents a case in the healing regime. As can be seen in this case, the initial values of the fibre strengths are such that the crack is filled with oxide, and the fibres are protected.
Finally it was considered a second case more representative of a real material. In particular, a tow made up of 509 fibres represented in Fig. 4.14 has been studied.

We have performed a battery of 50 simulations for different loads. The lifetimes obtained have been compared with the ones for the configuration 2.10 in Fig. 4.15. The vertical lines represent the dispersion of the lifetimes, and the dot represents the average value. It can be observed that the lifetimes are very similar at higher loads and, as expected in the case of the larger bundle, the average lifetimes calculated are slightly longer and their dispersions narrower.

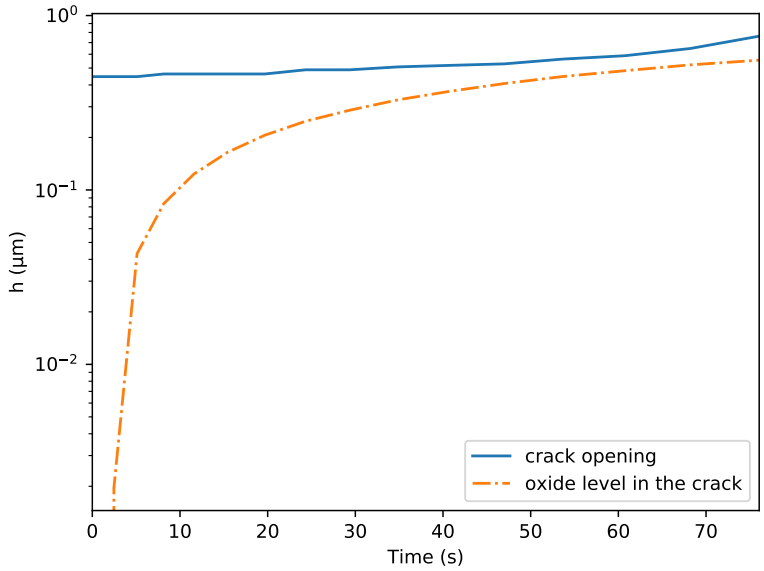

(a)

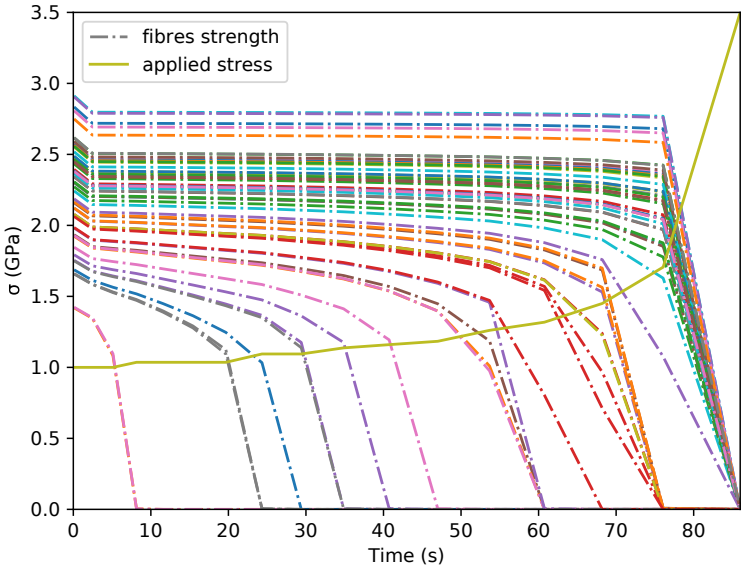

(b)

Figure 4.12: Evolution in time of the oxide inside the crack w.r.t. the crack's opening (a) and fibres' strength degradation (b) for non-healing regime in transition zone at T = 1173 K and σ = 1 GPa.

4.6 Chapter summary

In this chapter the failure mechanics model and the strategy adopted to calculate the lifetime of a SH-CMC mini-composite in an oxidizing atmosphere subjected to a tensile

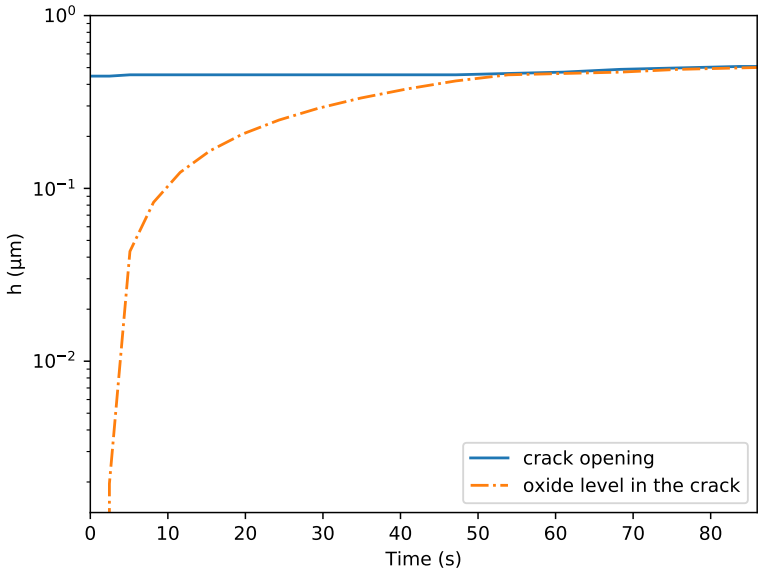

(a)

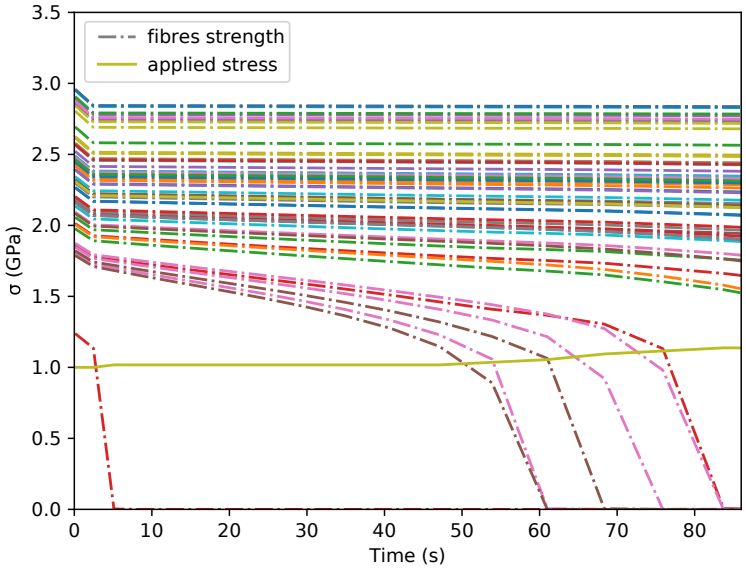

(b)

Figure 4.13: Evolution in time of the oxide inside the crack w.r.t. the crack's opening (a) and fibres' strength degradation (b) for healing regime in transition zone at T = 1173 K and σ = 1 GPa.

load are presented. In particular, the model for the self-healing description described in chapter 2 model has been coupled for the first time with a descriptive model of the sub-critical propagation of defects in the fibres (illustrated in chapter 3) which explicitly links the environmental conditions inside the crack instant by instant to the fibre strength.

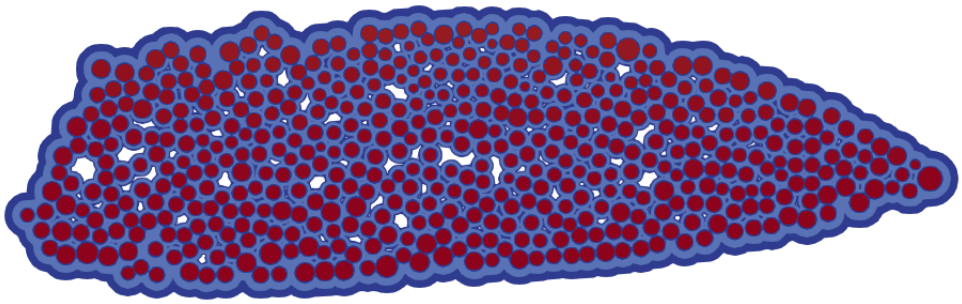

Figure 4.14: Tow 2 configuration.

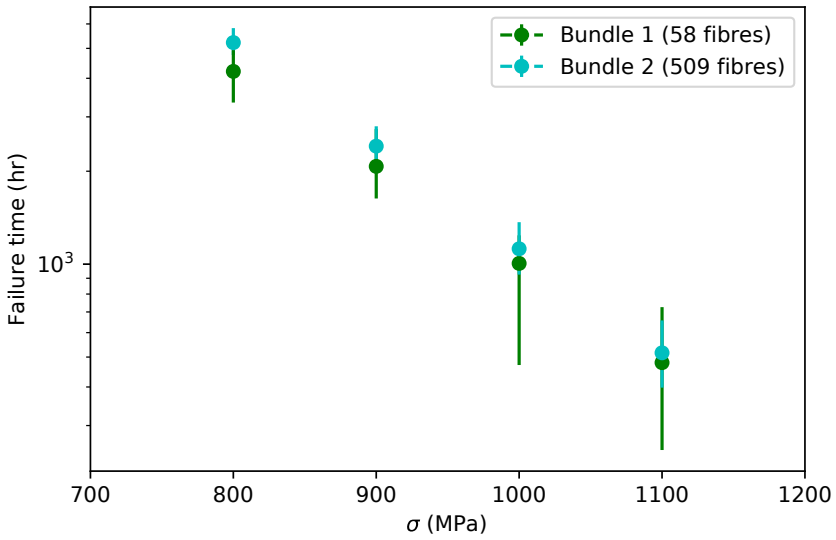

Figure 4.15: Mini-composite lifetimes vs applied stress for the two different tow size at $T = 973$ K.

Furthermore, this enables us to consider a naturally scattered fibre strength distribution. As a result, multiple simulations were performed to account for the stochastic nature of the problem and provide insight into the dispersion of the results. This model is entirely explicitly dependent on parameters such as temperature, pressure, mechanical properties of the material considered and applied load. Although the model is able to establish precisely both the lifetime of the mini-composite and its dispersion, the absence of experimental tests at this scale on this SH-CMCs allowed analyzing the results obtained from a purely qualitative point of view. The model shows how the presence of the oxide inside the crack drastically modifies the fibre failure scenario. In particular, it has been shown that while in the non-oxidizing case, the failure of the fibres depends only on their initial strength (which is an *a priori* parameter), in the oxidizing case, it is influenced by the position of the fibres inside the tow. Moreover, the model shows the different

behaviour of the material at different temperatures and stress parameters. Wide variations of the failure time values of the mini-composite are due to a healing/non-healing crack condition which depends not only on the considered conditions but also on the distribution of the fibre strengths and their initial values. In particular, a transition zone has been evidenced in which both behaviours coexist at fixed load and temperature conditions. Moreover, it could be interesting to modify the materials' choice, e.g. the type of fibres, and therefore the associated mechanical characteristics, to verify the conditioning on the material lifetime in different conditions.

Chapter 5

Towards upscaling, part I: parameters sensitivity for a tow

Contents

5.1 Introduction

The present chapter aims at providing a qualitative and quantitative parametrization of a mini-composite in terms of geometrical, topological, and scale parameters. Firstly, the stochastic convergence of the lifetime has been analyzed, as well as its stochastic moments to characterize the variability of the lifetimes in a single (or small number of) simulation. Furthermore, it has already been shown in the previous sections how the diffusion/oxidation processes follow a well-defined geometrical path within the crack. For this reason, different tow configurations with different geometrical properties and numbers of fibres were analysed. In particular, the influence of these parameters on the average and dispersion of lifetimes under various load and temperature conditions has been evaluated. Finally, a methodology was proposed to estimate the service life of mini-composites as a function of the aforementioned parameters.

5.2 Convergence study

The mini-composite coupled model presented in the previous chapters has a strong stochastic character. This is an intrinsic property of ceramic fibres as their strength is not represented by a fixed and unique value for all of them but, on the contrary, it is a function of the defects existing on their surface. These defects are due to manufacturing and fabrication processes. Therefore, as has already been discussed in chapter 3 and chapter 4, a certain distribution of fibre strength values in the bundle is considered. So each individual simulation is characterized by a different set of fibre strengths, as well as different spatial distributions of these values. Thus it may occur, for example, that for some parameter extractions a greater number of strong fibres are clustered closer to the outer edge. These are therefore quickly damaged, as more exposed to oxygen, and this impacts radically the lifetime, as was shown in chapter 2. The opposite can also happen, with strong fibres well protected in the center of the bundle, which generally increases the lifetime. The interaction of these factors, i. e. the initial set of fibre strength values and the location of the fibres in the tow, results in different mini-composite lifetimes under the same environmental conditions and tow configuration. For this reason, a convergence analysis was conducted on the mean and dispersion of the computed lifetimes. The aim is to find a sufficient number of simulations to be considered in order to estimate the correct mean and dispersion that are representative of the mini-composite's lifetime in each condition.

Therefore a reference tow was fixed, as shown in Fig. 5.1, consisting of 51 iso-distributed

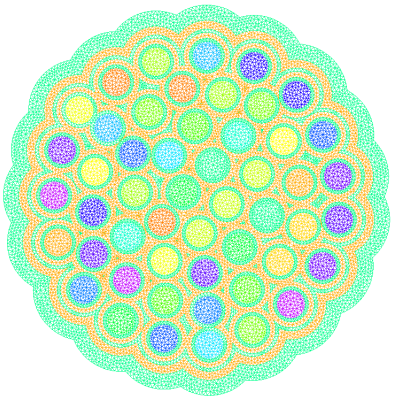

Figure 5.1: Reference tow.

Table 5.1: Relative error of the mean of different size bootstrap sample (b.s.) w.r.t. the mean of the reference sample (size = 100) for different values of applied stress.

	800 (MPa)	900 (MPa)	1000 (MPa)	1100 (MPa)
b.s. size 10 error	9.4 %	3.5 %	2.2 %	7.8 %
b.s. size 15 error	5.4 %	5.2 %	2.6 %	5.7 %
b.s. size 25 error	3.0 %	1.8 %	1.7 %	4.1 %
b.s. size 50 error	0.8 %	1.3 %	0.7 %	0.2 %

fibres. For each external condition, i.e. applied stress, temperature and oxygen concentration, 100 lifetimes were evaluated. These constitute the reference sample associated with the reference tow. From the reference sample, 10000 samples were extracted using the bootstrap technique with sizes 10, 15, 25 and 50 respectively. Thus, for each of them, a mean lifetime distribution of the considered tow was evaluated. The same operation was performed for different stress conditions as shown in Fig. 5.2. Starting from these data, it was then possible to compare the mean of each distribution obtained from different sizes with the mean calculated on the reference sample. The relative errors calculated for each applied stress condition are reported in Tab. 5.1. Note that the larger the sample size, the closer the mean is to the mean of the reference sample, and this is true for each condition. In particular, considering the values of the relative error, 50 can be considered a reasonable and representative size for the lifetime mean, since its error is less than 2% for each of the load conditions investigated. Concerning the dispersion of the lifetimes, an analogous process to the one above mentioned for the mean values has been considered. In Fig. 5.3 the distributions of the standard deviations of the bootstrap samples with sizes 10, 15, 25 and 50 considered above are shown. The mean of each distribution is compared with the standard deviation

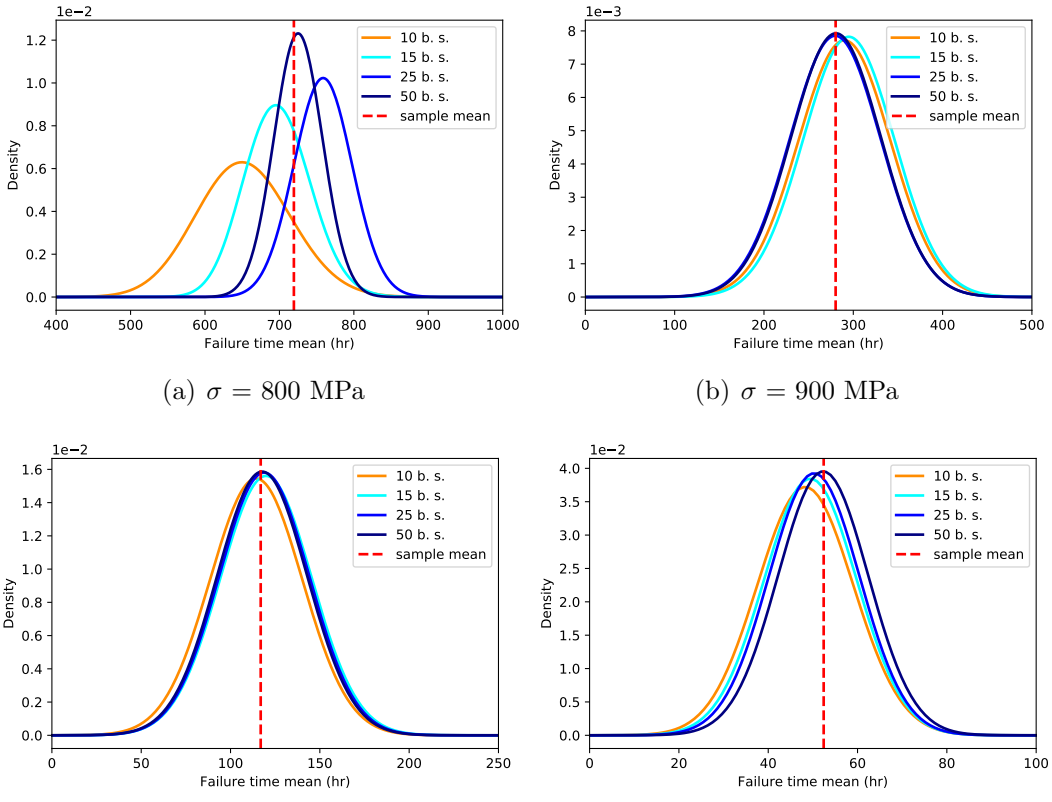

(a) $\sigma = 800$ MPa

(b) $\sigma = 900$ MPa

(c) $\sigma = 1000$ MPa

(d) $\sigma = 1100$ MPa

Figure 5.2: Mean distribution of different size bootstrap sample (10000 bootstrap = b.s.) w.r.t. the mean of the reference sample (size = 100) for different values of applied stress.

calculated for the reference sample.

The dispersion of the lifetimes in such conditions is well represented if one considers a sample of size 50. Looking at the relative errors of the mean of the distributions of the standard deviation with respect to the standard deviation of the reference sample (see Tab. 5.2), it can be remarked that the error decreases considerably (and not always linearly) as the sample size increases. In particular, for a sample of size 50, the error on the calculation of the dispersion of the lifetimes is approximately less than 2.1% in all the evaluated conditions.

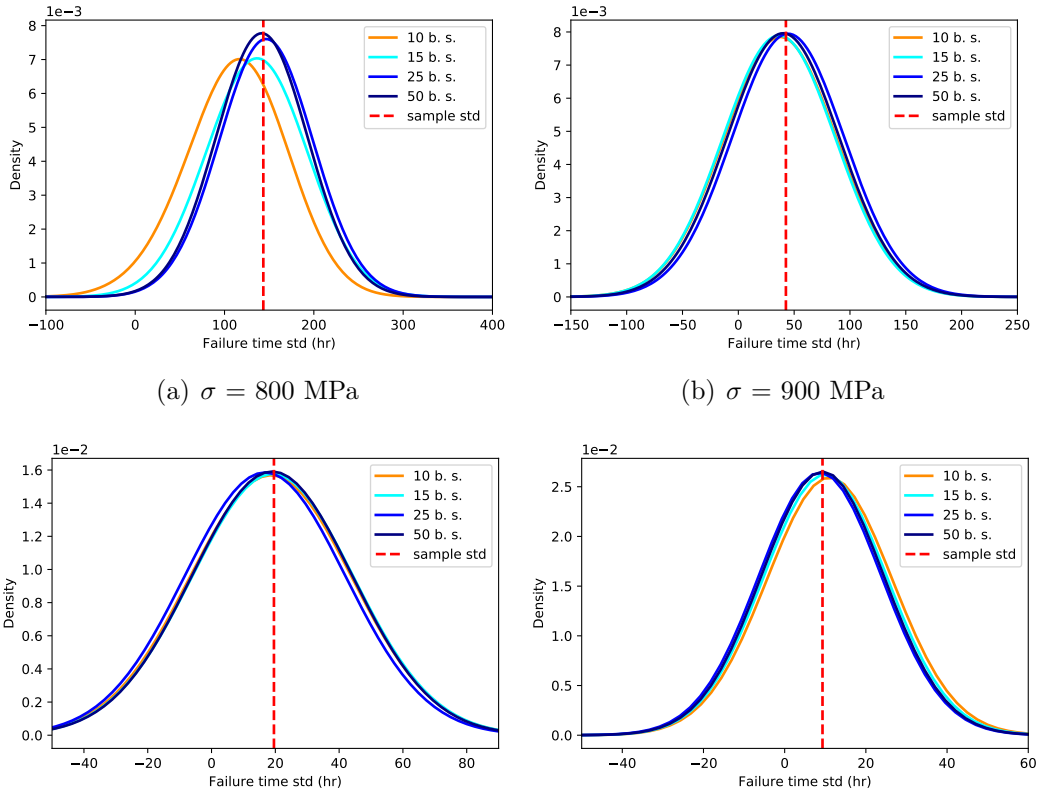

(a) $\sigma = 800$ MPa

(b) $\sigma = 900$ MPa

(c) $\sigma = 1000$ MPa

(d) $\sigma = 1100$ MPa

Figure 5.3: Standard deviation (std) distribution of different size bootstrap sample (10000 bootstrap = b.s.) w.r.t. the standard deviation of the reference sample (size = 100) for different values of applied stress.

Table 5.2: Relative error of the standard deviation (std) mean of different size bootstrap sample (b.s.) w.r.t. the standard deviation of the reference sample (size = 100) for different values of applied stress.

	800 (MPa)	900 (MPa)	1000 (MPa)	1100 (MPa)
b.s. size 10 error	21.3 %	12.2 %	4.9 %	18.8 %
b.s. size 15 error	5.4 %	14.3 %	2.8 %	7.4 %
b.s. size 25 error	3.1 %	4.5 %	1.9 %	6.6 %
b.s. size 50 error	2.1 %	1.3 %	1.4 %	0.8 %

5.3 Tow behaviour changing number of fibres, their topology and strength distribution

The two-dimensional modelling of the physical/chemical processes occurring in the crack has made it possible to highlight how the topological aspect of the yarn cross-section has an effect on its lifetime. Indeed, as previously discussed, the oxidative mechanisms are driven by the diffusion of oxygen through the crack, which occurs from the outside to the inside of the bundle. For this reason, there are some fibres that are more quickly subjected to degradation than others. The failure of the fibres as a result of such degradation is obviously also a function of their initial strength, which differs from one yarn to another. In fact, considering the tow that was already examined chapter 2 in Fig. 2.10, it can be remarked how the scenario and also the lifetime change if the same initial fibre strengths are placed in increasing order from the outside to the inside or *vice versa* , respectively (see Fig. 5.4).

If the weaker fibres are placed close to the outer edge of the tow (see Fig. 5.4(a)) the failure scenario is rather similar to that of a purely mechanical case (except, of course, for the final lifetime) since the two phenomena accelerating fibre failure (oxygen concentration and initial fibre strength) work in the same direction. On the other hand, if the weaker fibres are placed inside the tow, the failure scenario is totally different (see Fig. 5.4(b)): the external fibres take longer time to break (being those with the highest initial strength) but then the internal fibres holding the tow, being the weakest, fail immediately. Furthermore, depending on the number of fibres in the yarn and their configuration, the number of fibres breaking in the early stages of life can be decisive on the final lifetime of the bundle. The combination of these factors leads us to analyse how the geometry and topological aspect of the tow influences its lifetime in order to understand the phenomenon under study in even greater detail. For this reason, sections of yarns with a different number of fibres (such as 51, 101, 251, 501 fibres) and aspect ratio (0.25, 0.50, 1.00) were considered and shown in Fig. 5.5.

In the following sections, results on lifetimes obtained firstly by considering a fixed geometry and changing the number of fibres and then considering tow with the same number of fibres but different geometries will be presented.

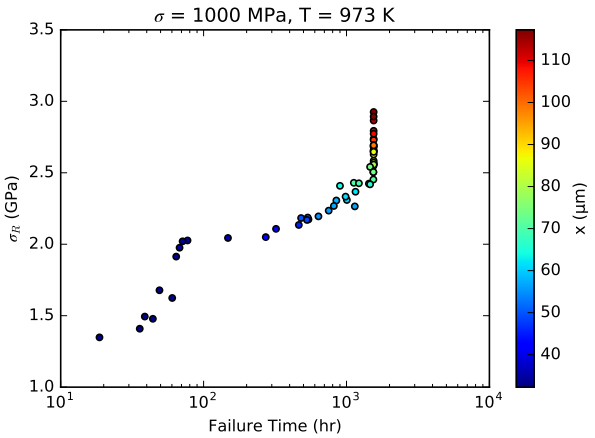

(a)

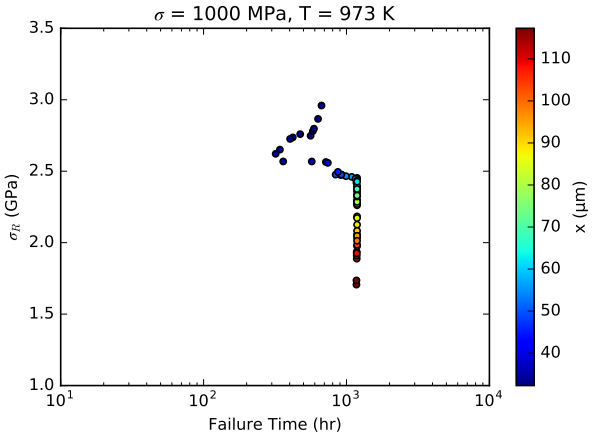

(b)

Figure 5.4: Lifetime and failure scenario of the fibres positioned depending on their initial strength in tow 2.10 : weaker fibres close to the outer edge, failure time : 1548 hours ≈ 65 days(5.4(a)), stronger fibres close to the outer edge, failure time : 1185 hours ≈ 49 days (5.4(b)).

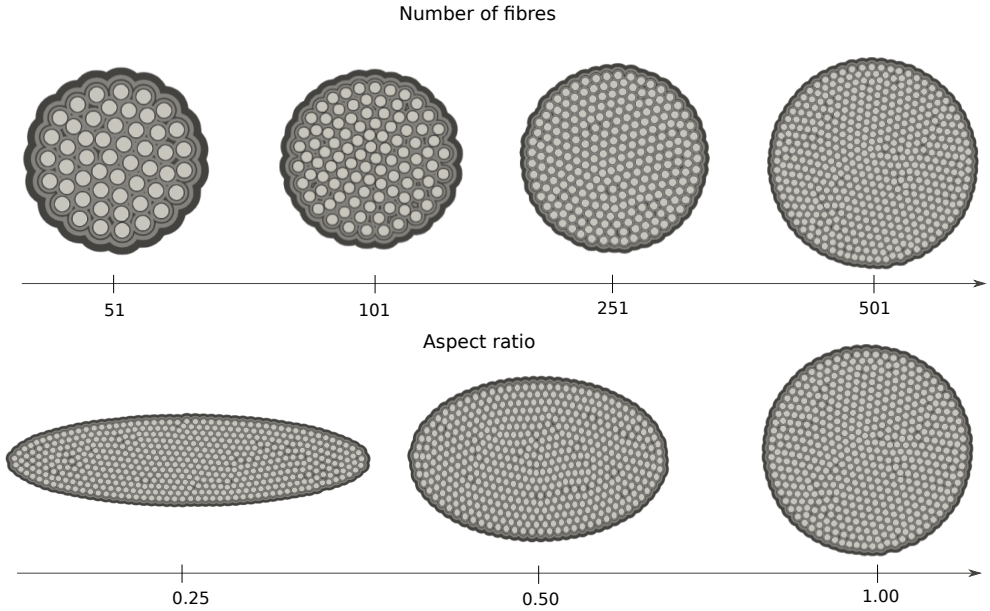

Figure 5.5: Tow configurations function of aspect ratio and number of fibres.

5.3.1 Influence of yarn's geometry

In assessing the influence of the aspect ratio of the yarn cross-section, the condition of iso-arranged and randomly-arranged fibres was also investigated to evaluate if there are some correlations regarding lifetimes. An example of the investigated configurations is given in Fig. 5.6.

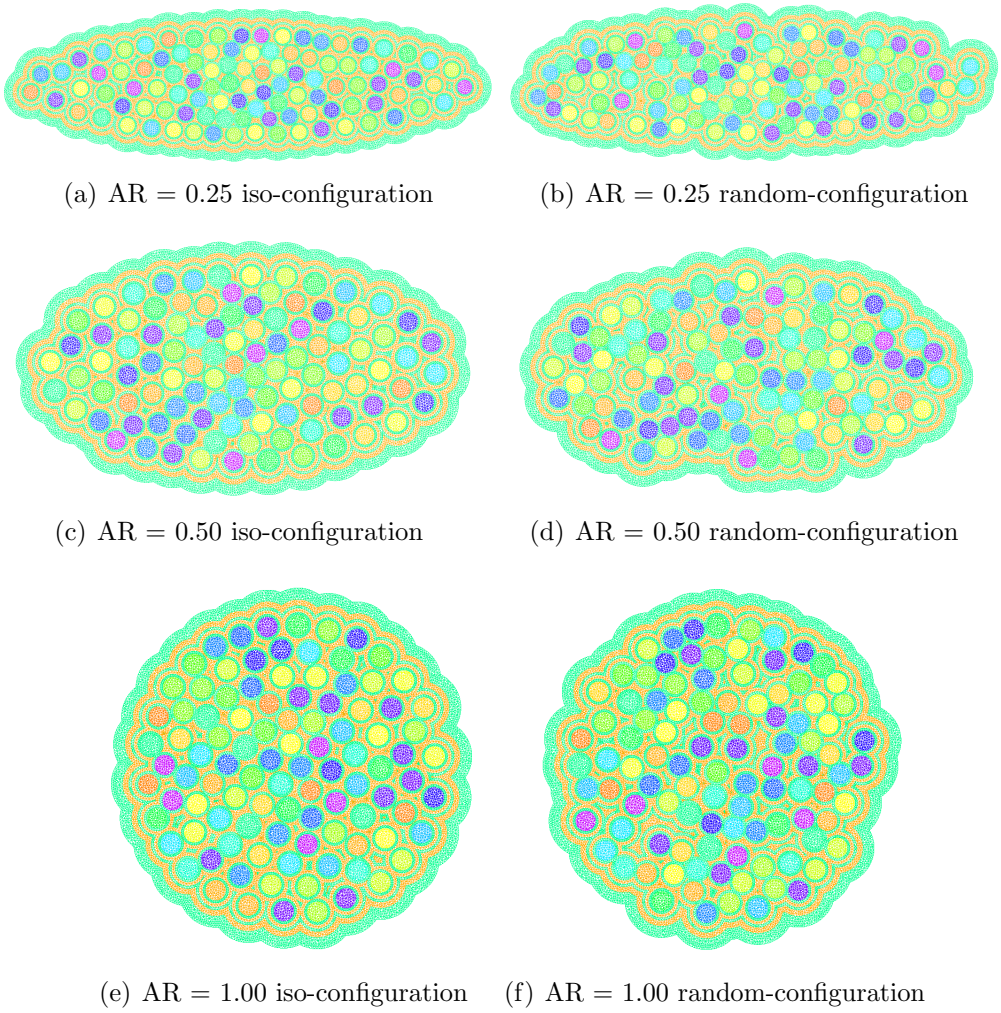

(a) AR = 0.25 iso-configuration (b) AR = 0.25 random-configuration

(c) AR = 0.50 iso-configuration (d) AR = 0.50 random-configuration

(e) AR = 1.00 iso-configuration (f) AR = 1.00 random-configuration

Figure 5.6: Tows with different aspect ratio and fibres arrangement.

The influence of the aforementioned parameters was also evaluated for various conditions of applied stress and temperature.

Applied stress

In this section, the results of the lifetime distributions calculated for the different shaped tows under varying applied stress are reported. In particular, the two threshold conditions concerning the aspect ratios considered, such as $AR = 0.25$ and $AR = 1.00$, are

investigated. In both cases, we considered both the configuration with iso-distributed fibres and the randomly one. For each condition, as has already been proposed in the previous sections, a battery of 50 simulations was run in order to evaluate the lifetime distribution. The results are shown in Fig. 5.7 considering tows made of 51 (Fig. 5.7(a)), 251 (Fig. 5.7(b)) and 501 (Fig. 5.7(c)) fibres, respectively.

Note that in all the cases presented, the lifetimes of the tow with $AR = 1.00$ are significantly greater than those obtained considering the tow with $AR = 0.25$. This is true for each loading condition and the number of fibres constituting the tow. In particular, the difference between the lifetimes of the above-mentioned tows increases with the number of fibres of the tow under consideration. Indeed, for a circular section, the minimum distance required for oxygen to reach the inner part is the same everywhere and is trivially represented by the radius of the section. On the contrary, in the case of a tow with an elliptical shape, the oxygen arrives faster towards the centre of the section as it diffuses along a shorter path, which corresponds to the minor semi-axis of the ellipse. When oxygen reaches the inner part of the bundle, it has faster access to those fibres, which, being positioned away from the edge, would have remained weakly oxidised for the first few stages. Therefore, in the circular yarn, the inner fibres are more protected, and therefore it has a longer lifetime. As far as the iso or random distribution of the fibres in the tow is concerned, we can state that although there is a variation in the lifetimes of the tows in the two configurations, it is not preponderant.

The role of the minimum distance from the centre is also evident by considering Fig. 5.8 where the calculated lifetimes for a yarn with $AR = 0.50$ with the same number of fibres and at the same conditions are also reported. It is observed that the values of the lifetimes in each condition are approximately proportional to the respective aspect ratios. Thus, taking the average lifetime of the tow with $AR = 1.00$ as a reference, the average lifetime of the tow with $AR = 0.50$ and the tow with $AR = 0.25$ are respectively about $1/2$ and $1/4$ of the mean lifetime of the yarn with circular cross-section.

Therefore, to specifically analyse the variation of the mean and dispersion of the mini-composite lifetimes as a function of its geometry and topology, the number of fibres in the tow was fixed (in this case, a tow containing 501 fibres was chosen) and iso-arranged and randomly-arranged fibres configurations were considered. The mean lifetime of the aforementioned configurations at varying tow aspect ratio was calculated for various loading conditions and is shown in Fig. 5.9(a) and Fig. 5.9(b), respectively. As was already observed above, the average lifetime decreases as expected as the load increases and it rises for the same external conditions as the aspect ratio increases in both conditions. For all these cases there is no substantial difference in terms of lifetime mean

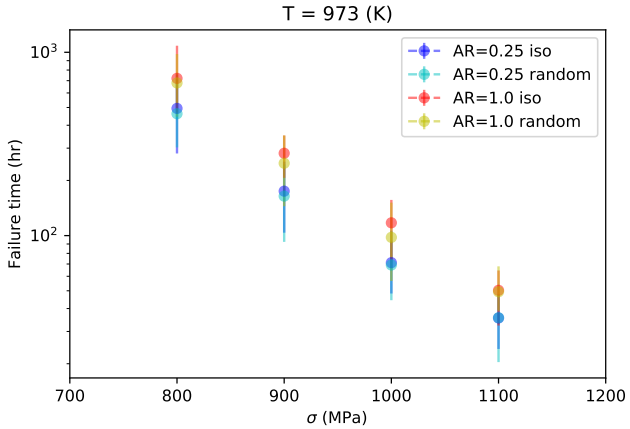

(a) 51 fibres

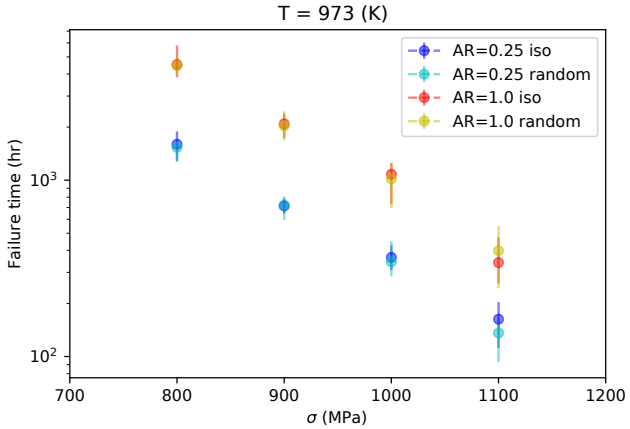

(b) 251 fibres

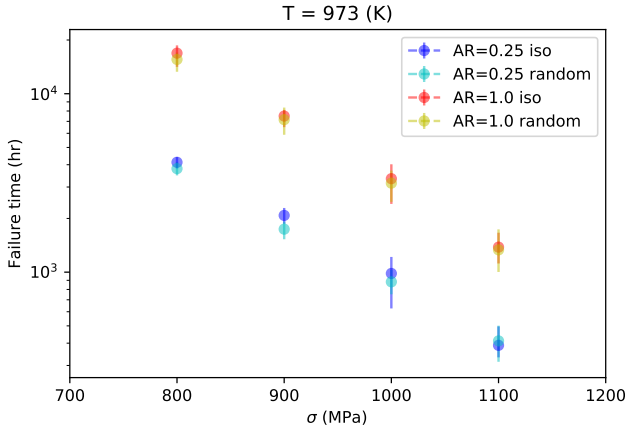

(c) 501 fibres

Figure 5.7: Failure time vs applied stress for tow with $AR = 0.25$ and $AR = 1.00$ constituted by 51 5.7(a), 251 5.7(b) and 501 5.7(c) fibres iso-distributed or randomly-distributed.

considering an iso-arranged or a randomly-arranged fibres case.

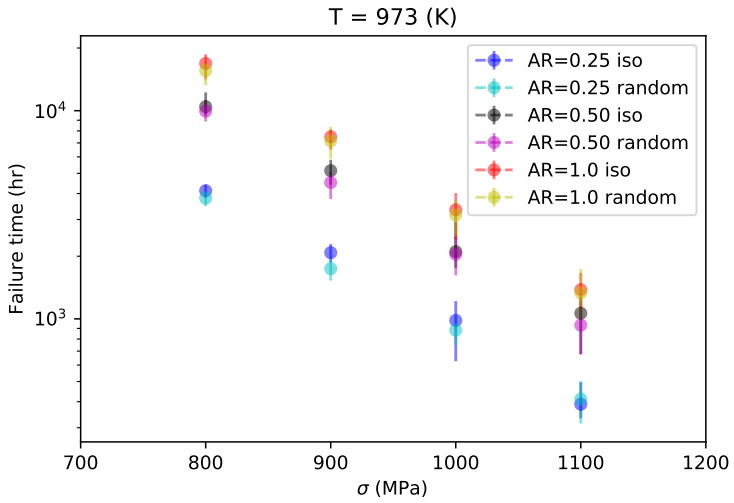

Figure 5.8: Failure time vs applied stress for tow with $AR = 0.25$, $AR = 0.50$ and $AR = 1.00$ constituted by 501 5.7(c) fibres iso-distributed or randomly-distributed.

As measure of lifetime dispersion, the coefficient of variation was considered. It is expressed as c.v. $= \sigma/\mu$, where σ represents the standard deviation and μ the mean. This parameter is useful to compare the variation of lifetimes under various conditions independently of their orders of magnitude as it is a dimensionless parameter. Therefore, Fig. 5.10 shows the trend of the coefficient of variation as a function of aspect ratio at different values of applied stress. In particular, Fig. 5.10(a) refers to an iso-distributed fibres condition, while Fig. 5.10(b) concerns the random one. It is evident that in all the these cases the coefficients of variation are very small, less than 0.15, suggesting that the lifetime distributions are rather close to the mean. Furthermore, we can observe that the coefficients of variation do not have a proportional trend with either the load or the aspect ratio. Finally, compared to the configuration of iso-arranged fibres, the random configuration leads to neither a reduction nor an increase in dispersion.

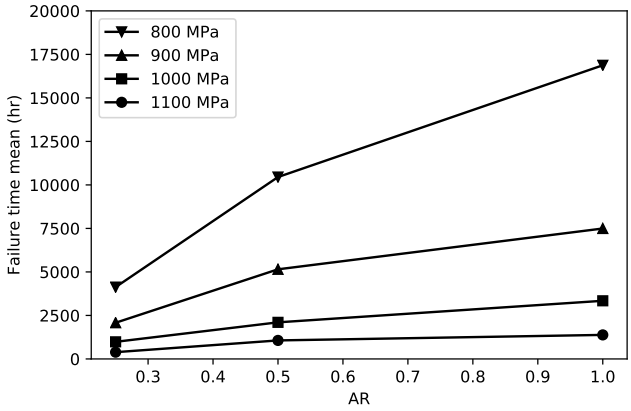

(a)

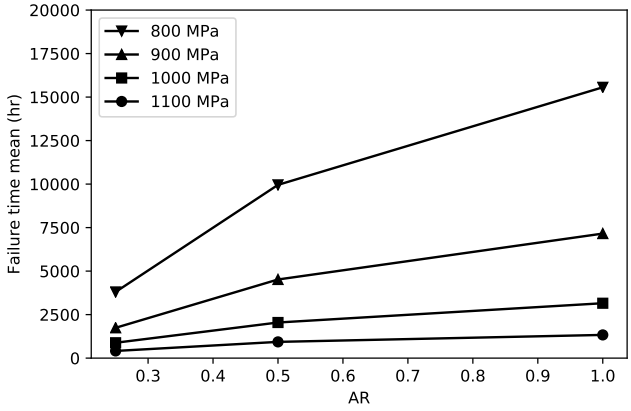

(b)

Figure 5.9: Failure time mean vs aspect ratio (AR) for a tow with 501 fibres iso-distributed 5.9(a) and randomly-distributed 5.9(b) subjected to different values of applied stress.

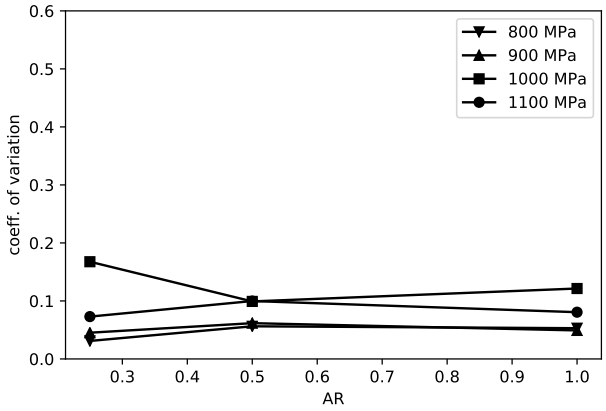

(a)

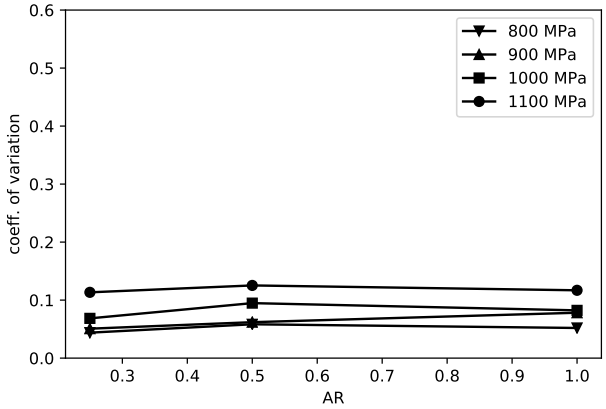

(b)

Figure 5.10: Failure time coefficient of variation vs aspect ratio (AR) for a tow with 501 fibres iso-distributed 5.9(a) and randomly-distributed 5.9(b) subjected to different values of applied stress.

Temperature

The influence of the geometry and topology of the mini-composite is here investigated in relation to temperature.

In particular, Fig. 5.11 shows the calculated lifetimes for the two extreme cases with respect to aspect ratio, i.e. $AR = 0.25$ and $AR = 1.00$, both in iso and randomly fibres arranged configuration. This was performed considering tow formed by 51 (see Fig. 5.11(a)), 251 (see Fig. 5.11(b)) and 501 (see Fig. 5.11(c)) fibres respectively. For each of these conditions, a battery of 50 simulations was run in order to provide an insight into the lifetimes dispersion. Also under different temperatures, it can be observed that the lifetimes of the mini-composite with circular cross-section are greater than those calculated for the tow with aspect ratio 0.25. This difference increases if we consider yarns with more fibres. In the latter case, the distance to be covered in terms of oxygen diffusion becomes even more significant. For each condition shown in Fig. 5.11 the same conditions for the bimodal and no-healing behaviour addressed in chapter 4 are found.

Once again the intermediate case in terms of aspect ratio between the two previously considered ones was taken into account, i.e. a tow with an aspect ratio of 0.50 having the same number of fibres (501 fibres). Fig. 5.12 shows the results in terms of lifetimes with respect to the two cases AR= 0.25 and $AR = 1.00$. Also here we observe a proportionality of the lifetimes with respect to the aspect ratio of the mini-composite section. Moreover, the same healing/transition/no-healing conditions are present in the configuration $AR = 0.50$.

It was already mentioned that the mini-composite exhibits three conditions as the temperature changes: healing, transition regime and no-healing. Therefore, two different distributions in the transition zone corresponding to the healing and no-healing conditions have been considered in the analysis of the averages and dispersions of the lifetimes. It is referred to as case a the no-healing condition and case b the healing condition at $T = 900$ °C and $\sigma = 1000$ MPa. Fig. 5.13 shows the increase in the mean lifetime as the aspect ratio increases and this is valid for every considered temperature. Furthermore, as Fig. 5.13(b) shows, there is no substantial variation when considering the randomly-arranged fibres configuration.

Furthermore, since it has been shown that for $\sigma = 1000$ MPa at $T = 900$ °C we may be in a no-healing condition, and at $T = 1000$ °C we are in no-healing condition: in these cases the lifetime of the mini-composite is reduced to a few hundred seconds. In such conditions, as can be seen in Fig. 5.14, the aspect ratio doesn't play any role on the lifetime. In fact, in the no-healing condition, the oxygen concentration is constant anywhere in the crack. The small variations noticeable are a few seconds and depend on

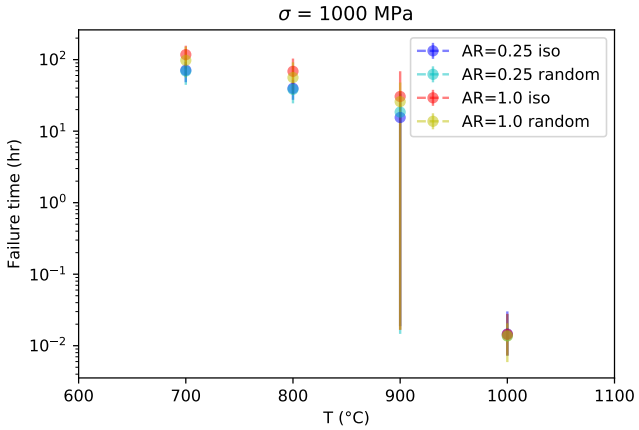

(a)

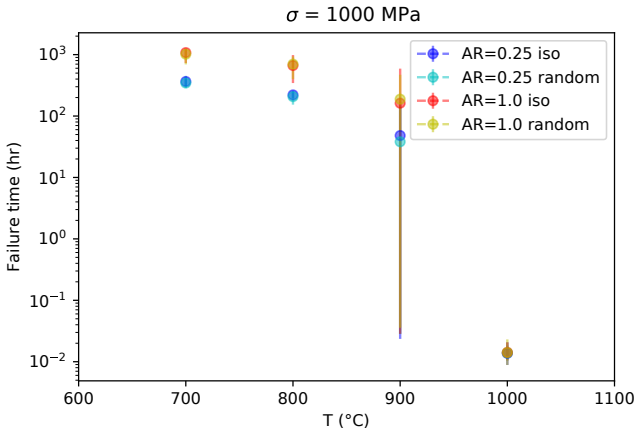

(b)

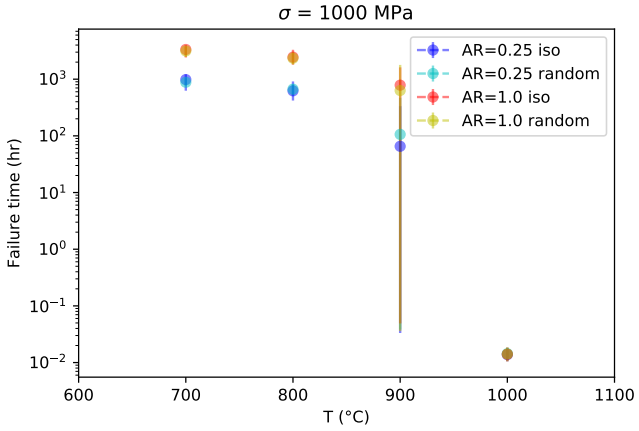

(c)

Figure 5.11: Failure time vs temperature for tow with $AR = 0.25$ and $AR = 1.00$ constituted by 51 5.11(a), 251 5.11(b) and 501 5.11(c) fibres iso-distributed or randomly-distributed.

the initial values of fibres strength.

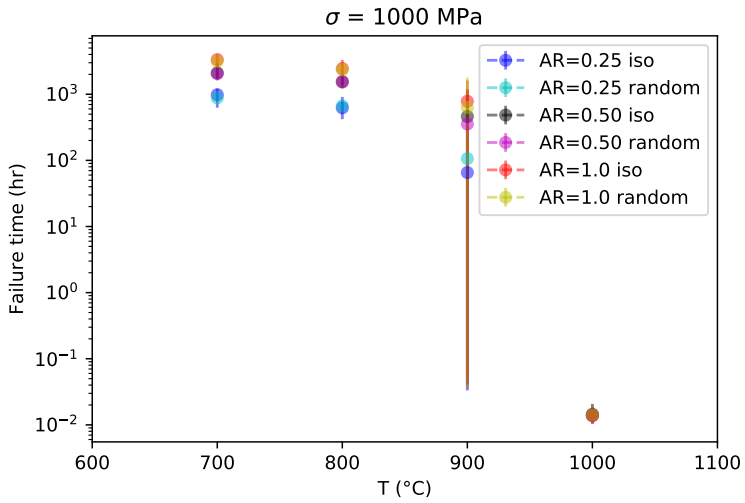

Figure 5.12: Failure time vs temperature for tow with $AR = 0.25$, $AR = 0.50$ and $AR = 1.00$ constituted by 501 fibres iso-distributed or randomly-distributed.

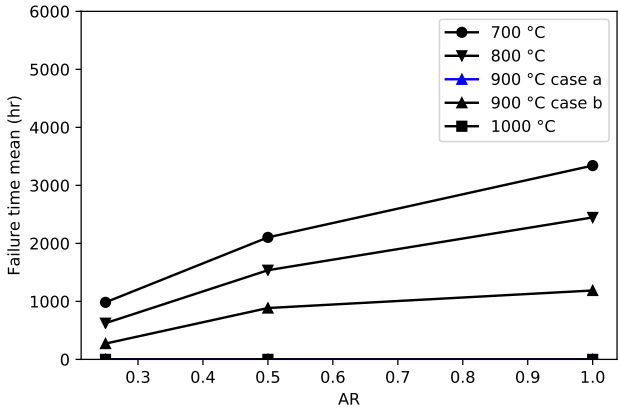

(a)

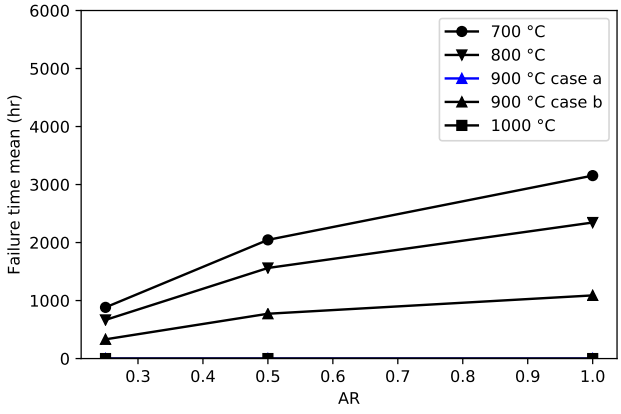

(b)

Figure 5.13: Failure time mean vs aspect ratio (AR) for a tow with 501 fibres iso-distributed 5.13(a) and randomly-distributed 5.13(b) at different temperatures.

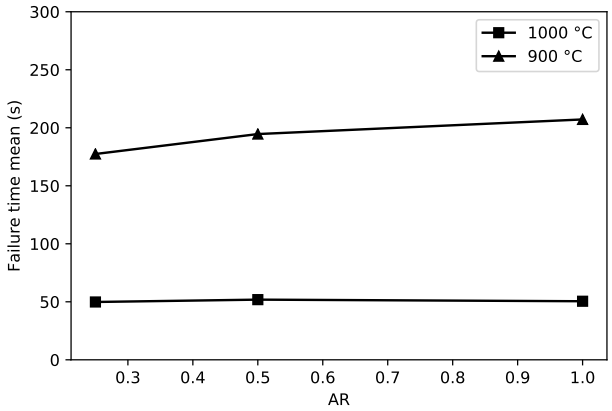

(a)

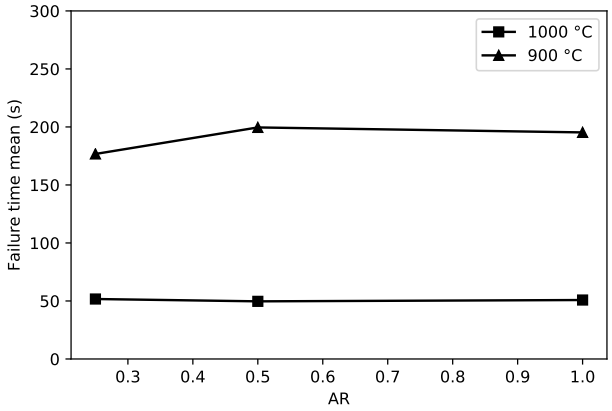

(b)

Figure 5.14: Failure time mean vs aspect ratio (AR) for a tow with 501 fibres iso-distributed 5.14(a) and randomly-distributed 5.14(b) for no-healing temperature condition.

Concerning the dispersion of the results, explained by means of the variation coefficient in Fig. 5.15, it can be noted that it is quite similar considering an iso-arranged or randomly-arranged fibre configuration and it does not appear to have a correlation with the aspect ratio of the considered tow.

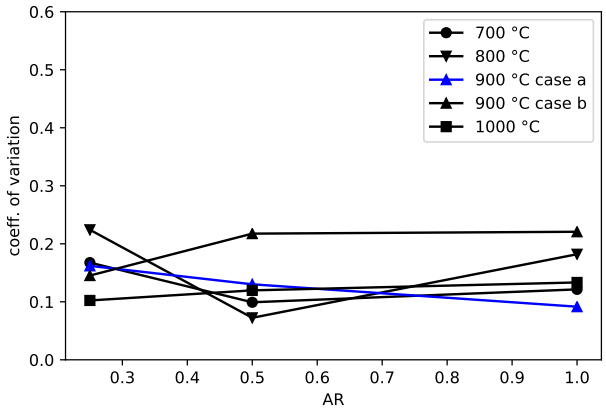

(a)

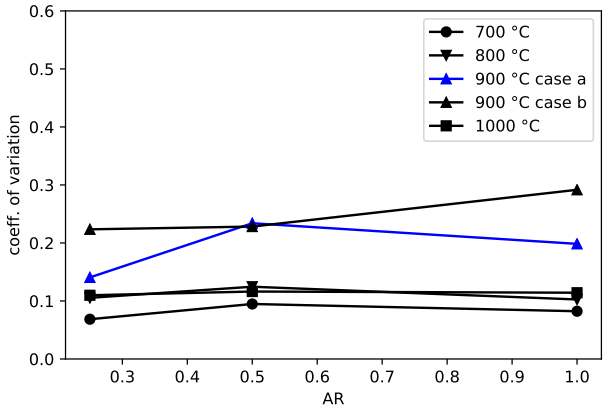

(b)

Figure 5.15: Failure time coefficient of variation vs aspect ratio (AR) for a tow with 501 fibres iso-distributed 5.9(a) and randomly-distributed 5.9(b) at different temperatures.

5.3.2 Influence of yarn's number of fibres

In this section, the aim was to investigate how the mini-composite's lifetime was affected by a variation of the number of fibres present within it assuming the same geometrical conformation. Different stress conditions were first considered at the same temperature, then the influence of the temperature was analysed considering the same applied stress. Therefore, different tow, with aspect ratios equal to 1, consisting of 51, 251, 101 and 501 iso-distributed fibres, respectively, were considered. This choice was made because, as seen in the previous section, assuming the same aspect ratio, we find the same behaviour for iso and randomly arranged fibres in terms of stress and temperature.

Applied stress

For all the aforementioned cases, the lifetimes are shown in Fig. 5.16 as the applied load varies. Fifty simulations were also performed for each individual condition and case. The lifetime of the mini-composites decreases almost linearly as the stress increases and, assuming the same applied stress, rises as the number of fibres increases.

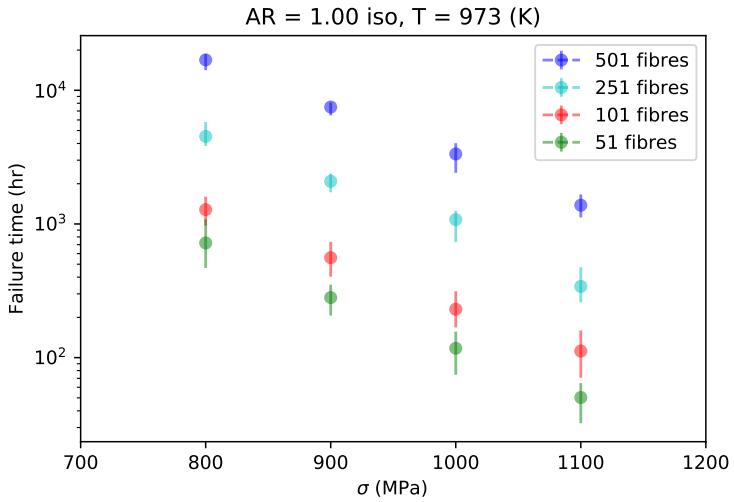

Figure 5.16: Failure time vs applied stress for tow with $AR = 1.00$ with different numbers of iso-distributed fibres.

This concept becomes even more evident if one considers Fig. 5.17, in which the trends of the mean lifetimes as a function of the number of fibres are shown.

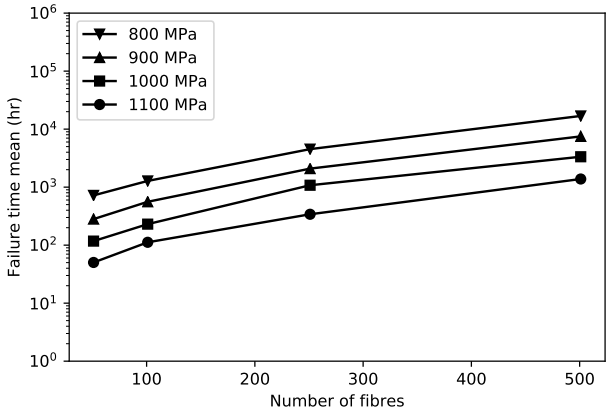

Figure 5.17: Failure time mean vs number of fibres for tow with $AR = 1.00$ subjected to different values of applied stress.

Concerning the scattering or the lifetime data, an increase in the number of fibres appears to have an overall weakly decreasing impact for all the load conditions analysed (see Fig. 5.18). In any case, it can be stated that, since the coefficient of variation is relatively low, the calculated lifetimes are all close to their mean.

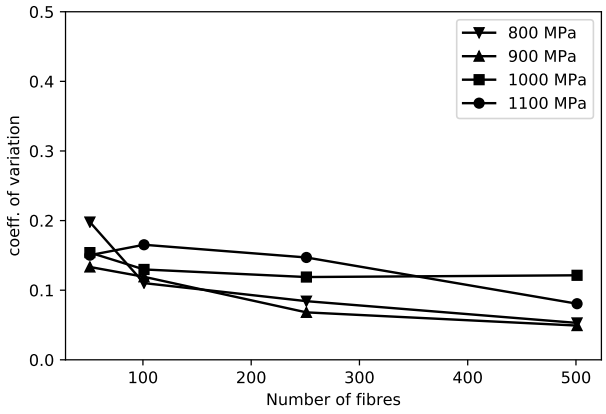

Figure 5.18: Failure time coefficient of variation vs number of fibres for tow with $AR = 1.00$ subjected to a different values of applied stress.

Temperature

Considering a tow with fixed shape and a varying number of fibres, we find the same conditions for the healing/no-healing regimes as shown in Fig. 5.19. Moreover, under healing conditions, the same gap can be observed between the lifetimes referring to the different bundles (51, 101, 251 and 501 fibres) under different temperature conditions.

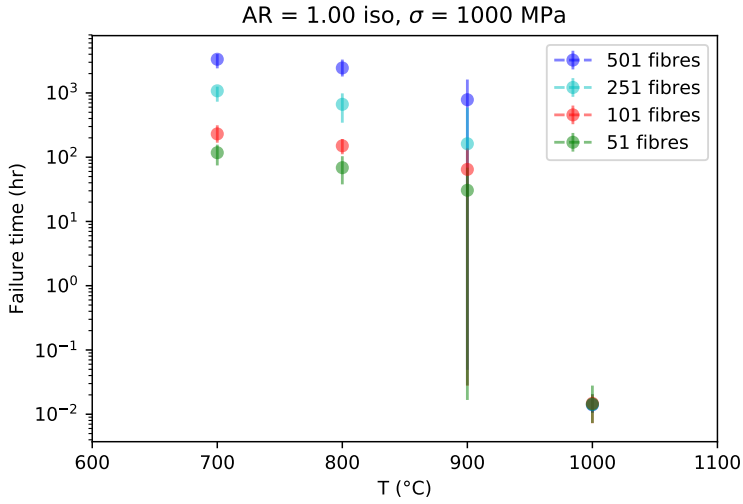

Figure 5.19: Failure time vs temperature for tow with $AR = 1.00$ with a different number of iso-distributed fibres.

In particular, by looking at the mean lifetimes of these configurations as a function of temperature in Fig. 5.20, it is evident that they increase as the number of fibres in the tow increases while decreasing as the temperature rises.
However, with regard to the scattering of the lifetimes, expressed by means of the coefficient of variation and shown in Fig. 5.21, it has no linear correlation either with the number of fibres present in the tow or with the temperature conditions.

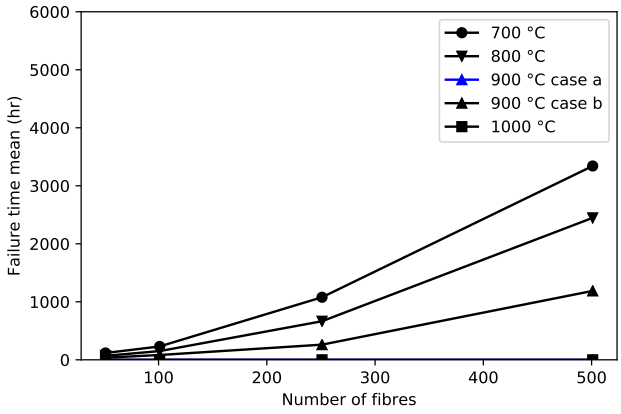

(a)

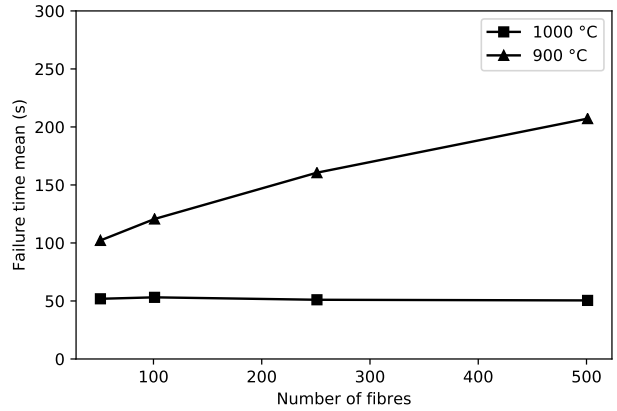

(b)

Figure 5.20: Failure time mean vs number of fibres for tow with $AR = 1.00$ at different temperatures.

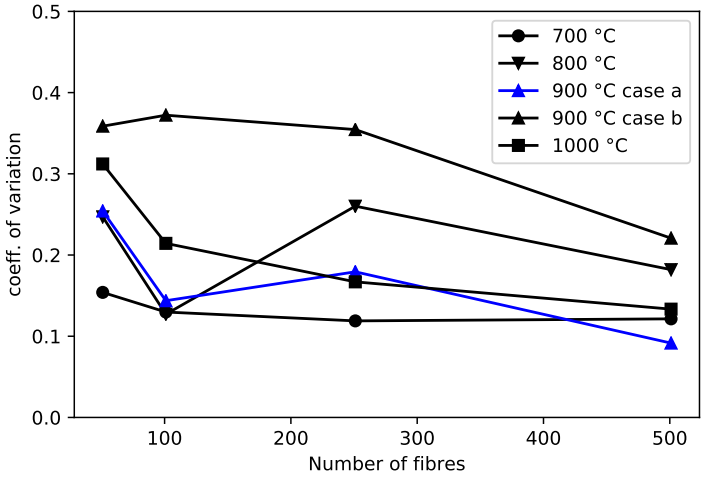

Figure 5.21: Failure time coefficient of variation vs number of fibres for tow with $AR = 1.00$ at different temperatures.

5.4 A strategy for computing yarn's lifetime

The analysis of the lifetimes of mini-composites with different shapes and dimensions properties revealed how these parameters play a role in determining the failure scenario. For this reason, it was decided to quantify these effects by means of the definition of two factors, referred to here as the shape factor and the scale factor. These factors represent the relationship between the lifetimes of tows with different aspect ratios and numbers of fibres, respectively. In this section, these factors and laws will be defined as a function of the relevant parameters together with a strategy for estimating the lifetimes of mini-composites under different loading conditions as a function of their geometrical characteristics.

5.4.1 Shape factor

Considering the dependence of the lifetime of the mini-composite on the aspect ratio observed in the previous section, it was possible to define a shape coefficient that takes into account the ratio of the average lifetime of tow in any random configuration to the average lifetime of the circular tow. The shape factor is therefore defined as follows:

$$\text{shape factor} = \frac{\text{mean } t_R(AR)}{\text{mean } t_R(AR = 1.00 \text{ iso})} \tag{5.1}$$

The values of the shape factor thus calculated referring to tow consisting of 501 fibres are shown in Fig. 5.22. The shape factor has been computed for each load condition (see Fig. 5.22(a)) and temperature (see Fig. 5.22(b)). Note that the curves for each condition have the same trend. In particular, the shape factor curve computed for the condition $T = 900$ °C results to be shifted as we are in bimodal behaviour, while the condition $T = 1000$ °C represents the no-healing condition.

Therefore, as a result of the considerations made in the previous section, a law describing the trend of the shape factor varying the geometrical parameters of the tow was defined. It is expressed as follows:

$$\text{shape factor law} = \frac{\dfrac{p\ (\text{AR} = 1 \text{ iso }\ )^2}{r\ (\text{AR} = 1 \text{ iso})}}{\dfrac{p\ (\text{AR random})^2}{b\ (\text{AR random }\ )}} \tag{5.2}$$

In particular it involves the perimeters p of the considered tow and the characteristic tow lengths, such as the radius r in the case of $AR = 1.00$ and the minor semi-axis b otherwise. As is shown in Fig. 5.23 the law written in this way fits pretty well the shape

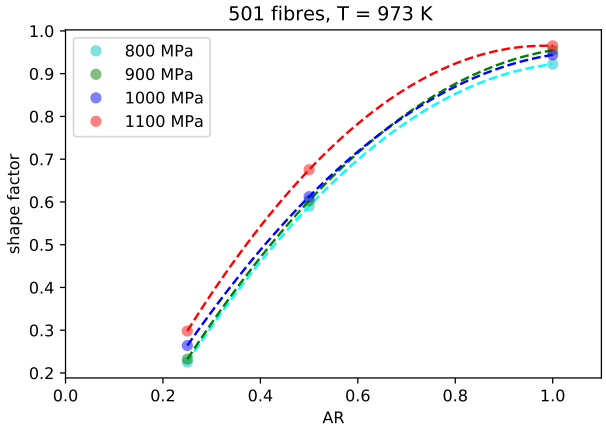

(a)

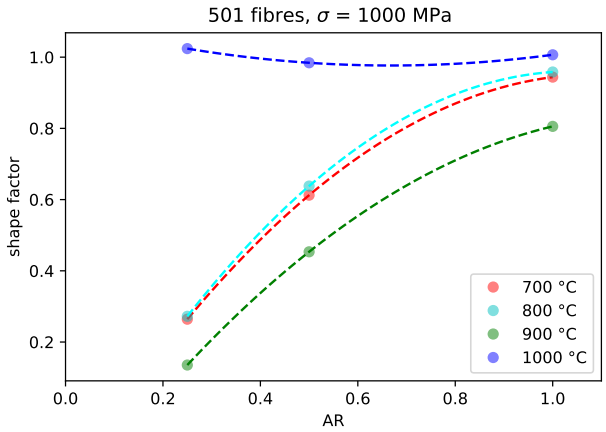

(b)

Figure 5.22: Shape factor vs. aspect ratio (AR) under different stress and temperature conditions (reference tow 501 fibres).

factor curves.

As it has been defined, the shape factor is only a function of the average lifetime of the tow considered. For this reason, the standard deviations of the ratio defined by the shape factor for each condition were considered associated with it. In particular, the confidence intervals corresponding to 2σ, representing the 95% confidence interval for lifetime dispersion, have been reported in Fig. 5.24.

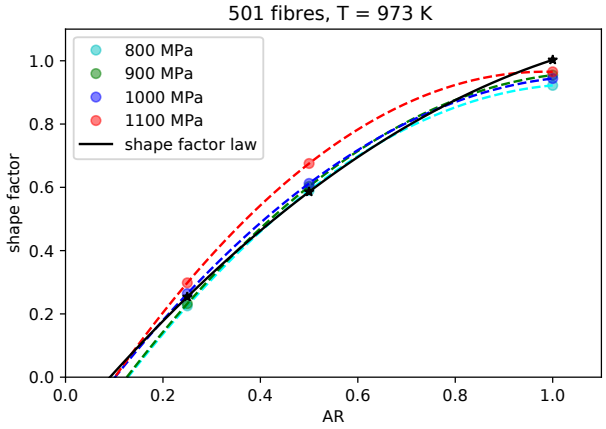

(a)

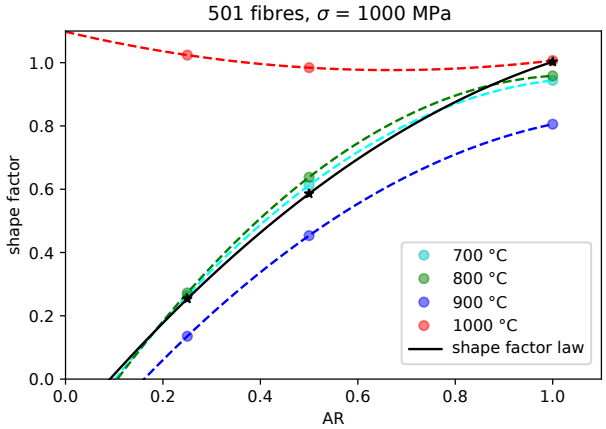

(b)

Figure 5.23: Shape factor law expressed in Eq. 5.2 vs. aspect ratio (AR).

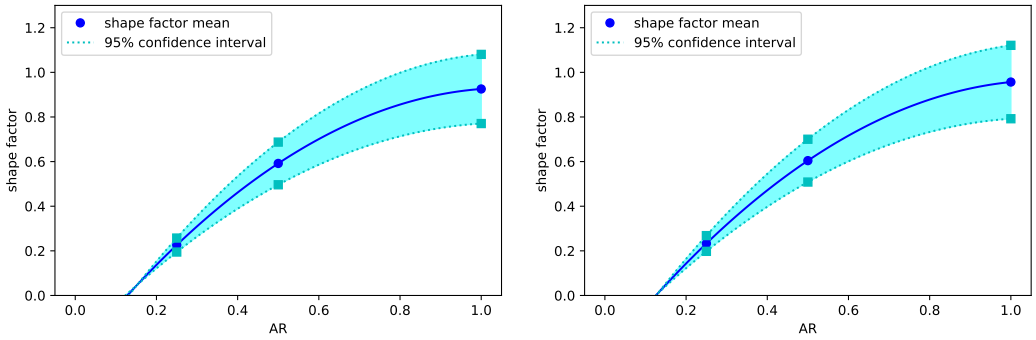

(a) $\sigma = 800$ MPa, $T = 700$°C

(b) $\sigma = 900$ MPa, $T = 700$°C

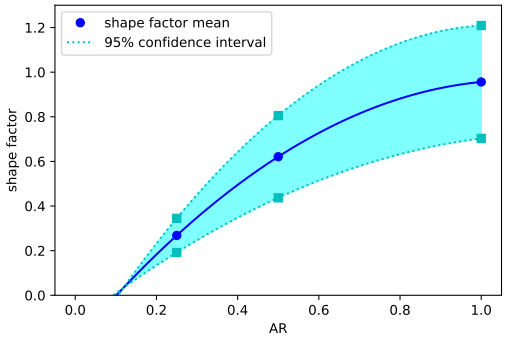

(c) $\sigma = 1000$ MPa, $T = 700$°C

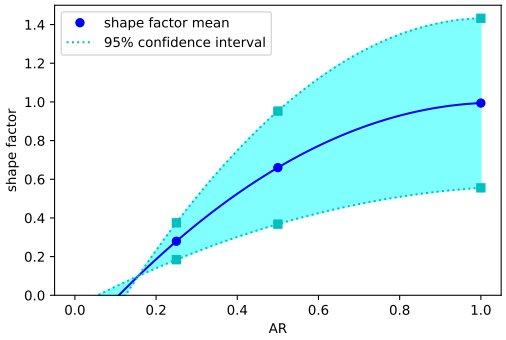

(d) $\sigma = 1000$ MPa, $T = 800$°C

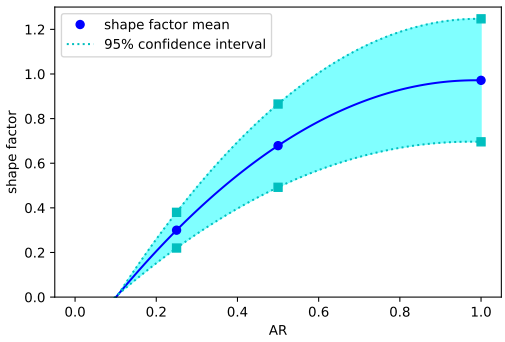

(e) $\sigma = 1100$ MPa, $T = 700$°C

Figure 5.24: Shape factor confidence area vs. aspect ratio (AR) for healing stress and temperature conditions.

5.4.2 Scale factor

Similar to the shape factor, a factor has been defined to describe the variability of the lifetime of the mini-composite as a function of the number of fibres in the tow compared to a reference sample. This factor was called the scale factor and was defined as follows:

$$\text{scale factor} = \frac{\text{mean } t_R \text{ (N. of fibres)}}{\text{mean } t_R \text{ (N = 51 fibres)}} \tag{5.3}$$

In this case, the reference lifetime sample was chosen as that obtained on a tow containing 51 fibres. Note that the scale factor is defined considering a fixed shape tow. In this case the scale factor is computed starting from a tow with aspect ratio equal to one. The representation of this scale factor is given in Fig. 5.25 under varying load (see Fig. 5.25(a)) and temperature (see Fig. 5.25(b)). Also in this case it can be observed that the curves present the same behaviour under varying conditions except for the cases where we find the bimodal and no-healing behaviour ($T = 900$ °C and $T = 1000$ °C respectively). Similarly as for the shape factor, a law was also defined in this case to reproduce the trend of the scale factor taking into account the variables influencing the lifetime as discussed in the previous section. Given tow having the same shape but different numbers of fibres, a law dependent on the area of the fibres placed on the perimeter can be defined as follows:

$$\text{scale factor law} = \frac{\dfrac{N_f}{A_f \cdot N_f^{ext}}}{\dfrac{N_f^{ref}}{A_f^{ref} \cdot N_f^{ext,ref}}} \tag{5.4}$$

where N_f is the number of fibres present in the considered tow, N_f^{ref} is the number of fibres present in the reference tow and A_f the area of a fibre. The trend of this law in relation to the number of fibres in the tow is shown in Fig. 5.26. This law exhibits a good fitting under varying conditions of applied stress and under varying temperature, if healing conditions are considered.
Finally, in order to account for the dispersion of the lifetime, the standard deviation of the scale factor was also defined for each healing condition. The results of the computed confidence area (corresponding to $\pm\ 2\sigma$) are shown in Fig. 5.27.

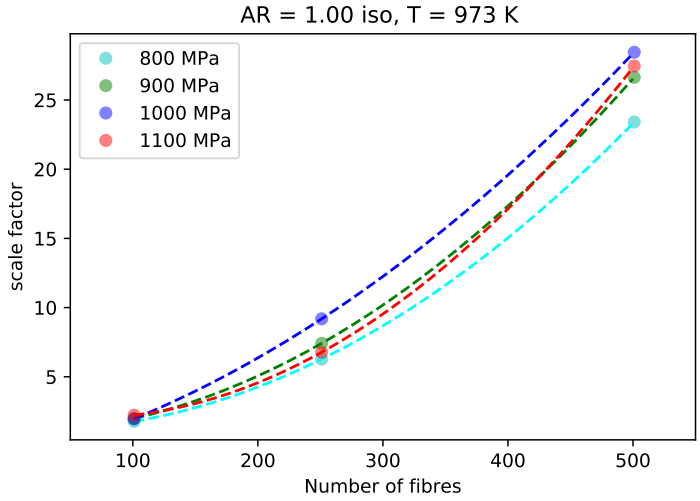

(a)

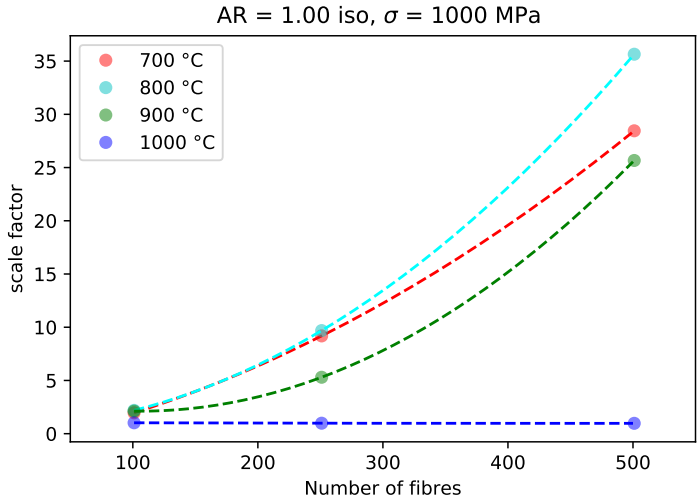

(b)

Figure 5.25: Scale factor vs. number of fibres under different stress and temperature conditions (reference tow AR = 1.00 iso configuration).

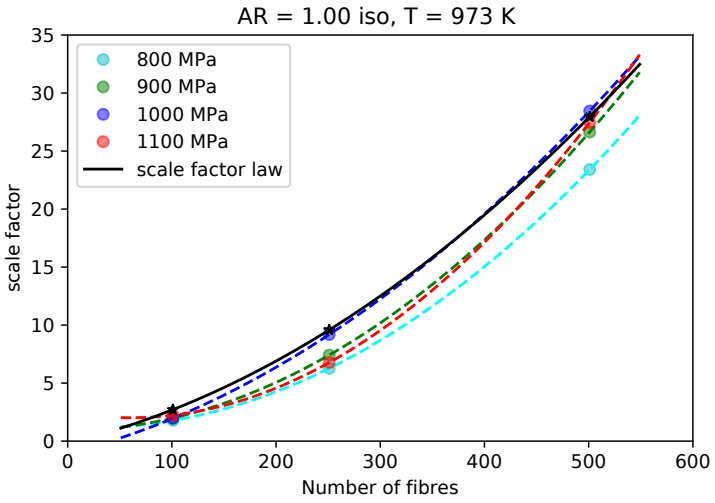

(a)

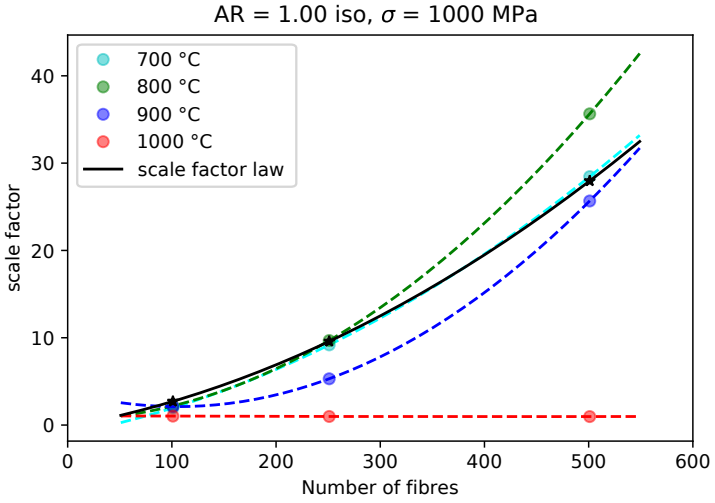

(b)

Figure 5.26: Scale factor law expressed in Eq. 5.4 vs. number of fibres.

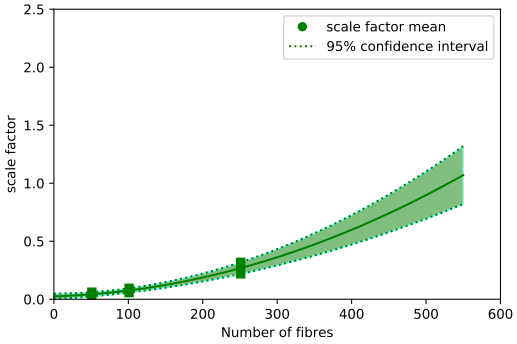

(a) $\sigma = 800$ MPa, $T = 700$°C

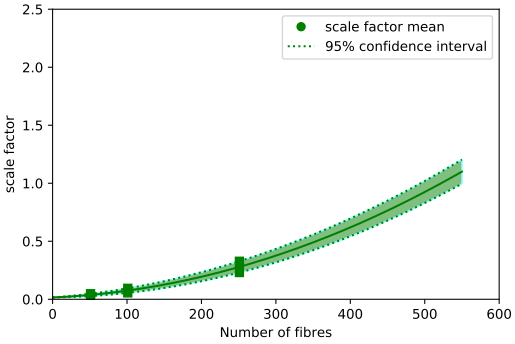

(b) $\sigma = 900$ MPa, $T = 700$°C

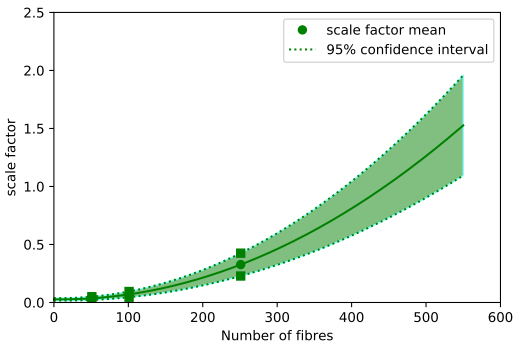

(c) $\sigma = 1000$ MPa, $T = 700$°C

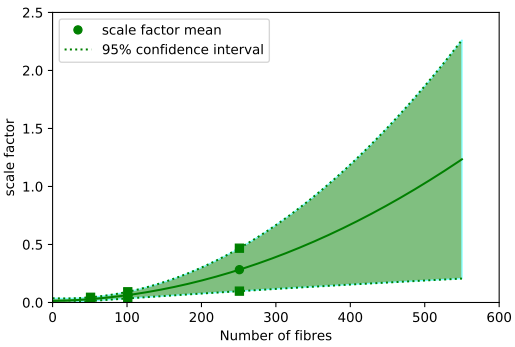

(d) $\sigma = 1000$ MPa, $T = 800$°C

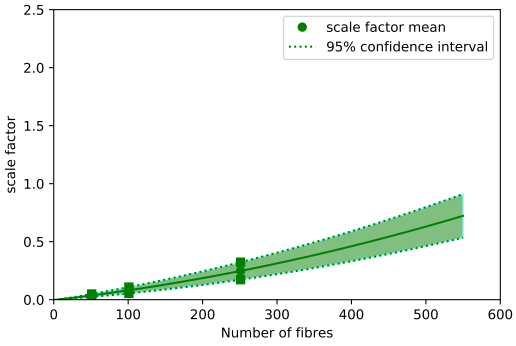

(e) $\sigma = 1100$ MPa, $T = 700$°C

Figure 5.27: Scale factor law vs. number of fibres for healing stress and temperature conditions.

5.4.3 Lifetime prediction

The understanding of the relevant parameters influencing the lifetimes of tows with different characteristics naturally led to the question of whether it would be possible to estimate the lifetimes of a mini-composite of any shape and size purely on the basis of these information. In particular, starting from a given configuration (i.e. having fixed the number of fibres and the aspect ratio) for which we know the lifetimes and their dispersion for different external conditions, the idea is to use the laws determined for the scale and the shape factor to obtain the lifetime of a tow having a different aspect ratio and a different number of fibres within it. In particular, the strategy used is depicted in Fig 5.28.

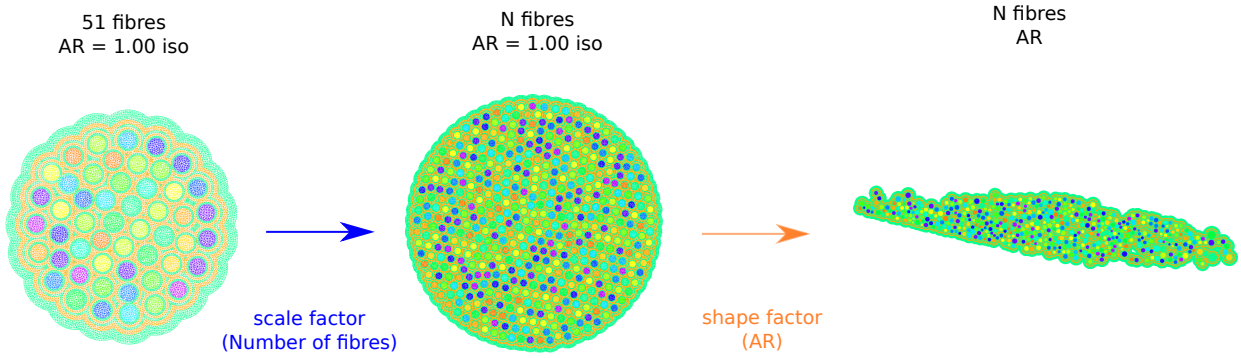

Figure 5.28: Sketch of the strategy used to predict the lifetime of tow depending on aspect ratio (AR) and number of fibres.

From the knowledge of the lifetime of a tow with a fixed AR and a specific number of fibres (depending on how the scaling factor has been defined), by means of the scaling factor it is possible to obtain the average and dispersion of the lifetime of a tow with the same AR but with a different number of fibres as the final tow. Subsequently, the same operation can be performed on such an intermediate tow obtained through the shape factor. In this way, the average and lifetime dispersion of a mini-composite with N fibres and specific AR is obtained. To test this strategy, two image-based representations of tow having 508 and 510 fibres and aspect ratios of 0.21 and 0.16, respectively, were considered and represented in Fig. 5.29.

Lifetimes (battery of 50 simulations) were then calculated for various stress conditions by means of the complete multi-physics model and subsequently compared with the area evaluated by means of the strategy described above. The results are given in Fig. 5.30. The area evaluated corresponds to $\mu \pm 3\sigma$, i.e. the 99.7% confidence interval. As can be seen, the agreement of the calculated and estimated lifetimes shows a good understanding of the influence of these parameters on the lifetime of the mini-composite.

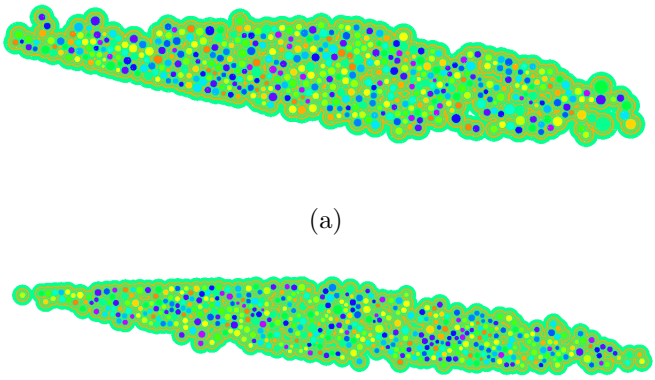

(a)

(b)

Figure 5.29: Image-based tow configuration.

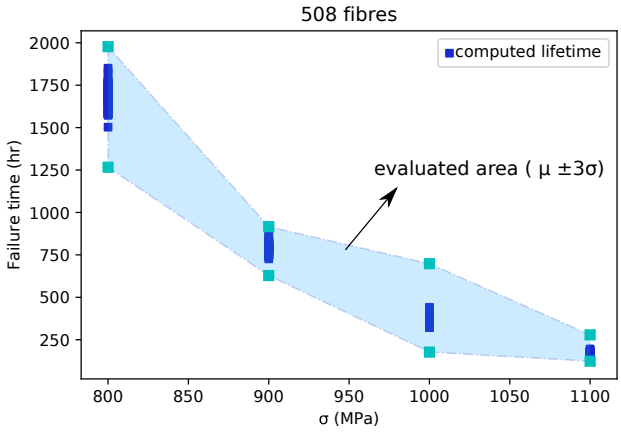

(a)

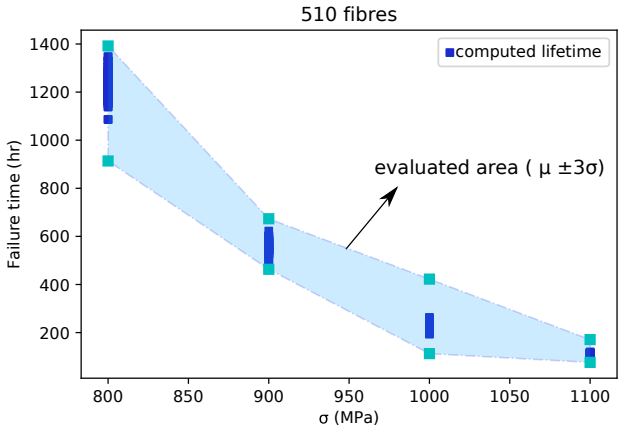

(b)

Figure 5.30: Comparison of lifetimes calculated via multi-physical model and evaluated by means of shape and scale factors for tow represented in Fig. 5.29 under different stress conditions.

5.5 Chapter summary

In this chapter, an analysis of the average and dispersion of the mini-composite lifetimes obtained by means of the multi-physics model described in the previous chapters was carried out. First of all, a convergence analysis was carried on by taking a particular conformation of tow as a reference and evaluating the number of simulations required in order to consider the correct representation of its mean and dispersion over the lifetimes for various conditions. It was thus demonstrated that considering a battery of 50 simulations for each condition yields a relative error of less than 2% on the mean and 2.1% on the standard deviation. Subsequently, different tow configurations for shape and number of fibres were analysed in order to determine the effect of these parameters on lifetime. In fact, it was verified that the lifetime of the mini-composite is strongly related to the geometry of the tow considered, and in particular its dependence is proportional to the minimum characteristic length of the tow. This is due to the oxygen diffusion field through the tow, which, as already shown in the previous chapters, follows a radial path from the outside (where the source is located) towards the inside of the tow. As the degradation of the fibres is dependent on the oxygen concentration, it is clear that fibres located in a certain sector, by breaking first, open the way for oxygen to reach more or less influential sectors of the tow. Although no correlation was found between the lifetime dispersions with the above parameters and external conditions, the same behaviour in transition conditions (i.e. where healing/no-healing conditions coexist) was found for all analysed configurations. The study of how shape and scale parameters affect lifetime allowed the definition of two factors, called shape and scale factors, determined from the tow in the analysed configurations. These factors were determined under each load and temperature condition and their trend was well reproduced through laws dependent on the parameters that were found to be most influential. These laws made it possible to calculate the life time of towers with different configurations at various load conditions solely through the knowledge of their geometric parameters. Although this strategy does not replace the entire multi-physics model implemented, it allows us to state that we have a good understanding of the main parameters and how they affect the failure mechanisms.

Chapter 6

Towards upscaling, part II: Polynomial Chaos Expansion (PCE) for the coupled global model

Contents

6.1 Introduction

This chapter aims at the development of a metamodel capable of reproducing the entire physical-chemical model presented in the previous chapters, obtaining as output the response in terms of lifetime of the mini-composite at the variation of the assigned inputs. Indeed, the creation of such a metamodel allows to perform an explicit sensitivity analysis on the input parameters, highlighting their major contributions and interactions in terms of lifetime variation. Therefore, initially a PCE-based metamodel representing the slow crack growth model presented in chapter 3 was built in order to compare the results obtained on the sensitivity of the parameters in terms of Sobol' indices with those obtained through the analytical formulation. Subsequently, the PCE-based metamodel was developed representing the global model, on which the sensitivity analysis of the input parameters was performed. Finally, in order to evaluate the importance of the spatial distribution of the fibre strengths for different tow configurations, a metamodel with constant external conditions was also created and used for the sensitivity analysis of these parameters.

6.2 Fundamentals of PCE Metamodeling

More generally, an analytical solution can not always be obtained for the problem to be solved and therefore the above-mentioned methods may not be directly applied to perform the sensitivity analysis. As already illustrated in chapter 3, in order to compute the Sobol' indices, it is necessary to evaluate the variances associated with the model. Although it can be done with Monte Carlo (MC) simulations, the computational costs would be very large due to the high dimensionality of the problem. In this cases, the sensitivity analysis passes through the creation of a so-called metamodel (or surrogate model), which is able to reproduces the same (or almost) response of the real model with a lower computational cost. Successively, the sensitivity analysis is carried out directly on the created metamodel. In the present thesis the surrogate models based on polynomial chaos expansion (PCE) are treated.

6.2.1 Polynomial chaos expansion

Considering a random vector with independent components $\mathbf{X} \in \mathbb{R}^M$ described by the joint probability density function (PDF) f_x, the Polynomial Chaos Expansion (PCE) of the computational model $M(\mathbf{X})$ response is defined as follows:

Table 6.1: Correspondence between the variable distribution and the optimal family of orthonormal polynomials.

Type of variable	Distribution	Orthogonal polynomials
Uniform	$\mathbf{1}_{]-1,1[}(x)/2$	Legendre $P_k(x)$
Gaussian	$\frac{1}{\sqrt{2\pi}}e^{-\frac{x^2}{2}}$	Hermite $H_{ek}(x)$
Gamma	$x^a e^{-x}\mathbf{1}_{\mathbb{R}}(x)$	Laguerre ${L_k}^a(x)$
Beta	$\mathbf{1}_{]-1,1[}(x)\cdot\frac{(1-x)^a(1+x)^b}{B(a,b)}$, with $B(a,b)=\frac{\Gamma(a)\Gamma(b)}{\Gamma(a+b)}$	Jacobi ${J_k}^{a,b}(x)/J_{a,b,k}$

$$y = M(\mathbf{X}) \approx M^{PCE}(\mathbf{X}) = \sum_{\alpha \in A} y_\alpha \Psi_\alpha(\mathbf{X}) \tag{6.1}$$

The response of the model Y is approximated through a polynomial expansion in which y_α represent the coefficients of the expansion, $\Psi_\alpha(\boldsymbol{X})$ the multivariate polynomials and α are the components of the multivariate polynomials. The polynomial basis $\Psi_\alpha(\boldsymbol{X})$ is built starting from a set of univariate orthonormal polynomials ${\phi_k}^{(i)}(x_i)$ [71] which satisfy the following relation for each variable i:

$$< {\phi_j}^{(i)}(x_i), {\phi_k}^{(i)}(x_i) >= \int_{D_{x_i}} {\phi_j}^{(i)}(x_i){\phi_k}^{(i)}(x_i) f_{X_i}(x_i)dx_i = \delta_{jk} \tag{6.2}$$

where j and k are the corresponding polynomial degrees. Then they are assembled as the tensor product of their univariate counterparts:

$$\Psi_\alpha(\mathbf{X}) = \prod_{i=1}^{M} {\phi_{\alpha_i}}^{(i)}(x_i) \tag{6.3}$$

due to the orthonormality of univariate orthonormal polynomials shown in the Eq. 6.2, also the multivariate polynomials built are orthonormal. Consequently, it is valid the following:

$$\langle \Psi_\alpha(x), \Psi_\alpha(x) \rangle = \delta_{\alpha\beta} \tag{6.4}$$

The univariate polynomials are built according to the PDF of each input parameter. The classic families of polynomials used are shown in Tab. 6.1.

6.2.2 Calculation of the coefficients

Regarding the calculation of the coefficients y_α, different techniques have been considered in this work. The investigated methods are the Ordinary Least-Squares (OLS) minimization, Least Angle Regression (LAR) and the Orthogonal Matching Pursuit (OMP). These methods all belong to the projection techniques. In this discussion we wanted to make a comparison between the results obtained using the three alternative approaches to build the surrogate model in terms of reproducibility of the model response. In this view the coefficients are a result of the post-processing of the experimental design set given on a proper sampling of the input random variables. The Ordinary Least-Squares (OLS) basically solves a minimization problem. It is possible to write the model's polynomial expansion approximation as a truncated summation with a residual term that has to be minimized, as is reported below:

$$Y = M(\mathbf{X}) \approx M^{PCE}(\mathbf{X}) = \sum_{j=0}^{p-1} y_j \mathbf{\Psi_j}(\mathbf{X}) + \epsilon_p = \mathbf{y^T \Psi_j}(\mathbf{X}) + \epsilon_p \tag{6.5}$$

Therefore, considered the $\boldsymbol{A}$ matrix of experimental design points, to each of which corresponds a certain response of the system Y, the least-square minimization problem can be set up as:

$$\hat{\mathbf{y}} = \arg\min \mathbb{E}\left[\left(\mathbf{y^T \Psi_j}(\mathbf{X}) - M(\mathbf{X})\right)^2\right] \tag{6.6}$$

The Eq. 6.6 which can be solved directly considering:

$$\hat{\mathbf{y}} = \left(\mathbf{A^T A}\right)^{-1} \mathbf{A^T Y} \tag{6.7}$$

where $A_{ij} = \Psi_j(x^{(i)})$, $i = 1, .., n$ and $j = 0, ..p-1$.

The Least Angle Regression (LAR) is based on the so-called principle of sparsity of effects. Indeed, in most applied science problems, only low-order interactions between variables are important. Thus the idea is to add a term that forces the minimization in favor of the low-rank solutions as follows:

$$\hat{\mathbf{y}} = \arg\min \mathbb{E}\left[\left(\mathbf{y^T \Psi_j}(\mathbf{X}) - M(\mathbf{X})\right)^2\right] + \lambda || \sum_{\alpha \in A} |y_\alpha| || \tag{6.8}$$

Finally, the Orthogonal Matching Pursuit (OMP) uses a greedy iterative strategy that minimizes the approximation residual at each iteration. Since the residual can be written as follows:

$$R_n = \langle R_n, \psi_{\alpha_{n+1}} \rangle \psi_{\alpha_{n+1}} + R_{n+1} \tag{6.9}$$

then the relation below holds:

$$||R_n||^2 = | < R_n, \psi_{\alpha_{n+1}} > |^2 + ||R_{n+1}||^2 \tag{6.10}$$

Consequently, minimizing the residual is equivalent to choosing a polynomial such that this quantity is maximized:

$$\psi_{\alpha_{n+1}} = \arg\max_{\alpha \in A} | < R_n, \psi_\alpha > | \tag{6.11}$$

It is worth to underline that the latter two techniques both use only a subset of the most relevant polynomials since the coefficients of all the other are set to 0.

6.2.3 Error estimation

The construction of a good metamodel requires an estimation of the error on the response approximation process. Several measures of error that are defined in this sense exist. In this work, in order to consider sets of experimental designs having different sizes, the modified leave-one-out cross-validation error was considered [71]. It is defined as:

$$\epsilon_{LOO} = \frac{\sum_{i=1}^{N} \left(\frac{M(\mathbf{x}^{(i)}) - M^{PCE}(\mathbf{x}^{(i)})}{1 - h_i} \right)^2}{\sum_{i=1}^{N} \left(M(\mathbf{x}^{(i)}) - \hat{\mu}_y \right)^2} \tag{6.12}$$

where $\mathbf{h} = diag(\mathbf{A}(\mathbf{A^T A})^{-1}\mathbf{A^T})$ and $\boldsymbol{A}$ is the experimental matrix.

6.3 PCE Metamodeling for SCG Problem

With a view to applying this technique to the most general possible problem, i.e. the global self-healing problem which involves all chemistry, physics and mechanics field for a mini-composite, as starting point it was chosen the same static fatigue model studied in chapter 3, considering this time the solution obtained numerically (this leads the possibility of having a non-constant oxygen concentration). Thus, considering the input variables examined in chapter 3 and reported in Tab. 6.2, the three-dimensional sample has been generated and the PCE-based metamodel has been built. Here UQLab library [70] is used to facilitate the implementation of a code to compute the metamodel and the Sobol' indices. The same sample was then used in order to compute the real

response of the system through a numerical code and finally, the results were compared both in terms of probability density function of the model output and sensitivity indices of the input parameters w.r.t. the one obtained for the analytical formula.

Table 6.2: Input parameters of the PCE metamodel for the slow crack growth problem.

Name	Distribution	Parameters	Description
T	Uniform	[773.15 - 1273.15]	Temperature [K]
σ	Uniform	[1100 - 1500]	Applied stress [MPa]
P	Uniform	[0.01 - 0.99]	Failure probability

The explained logic process is represented in Fig. 6.1.

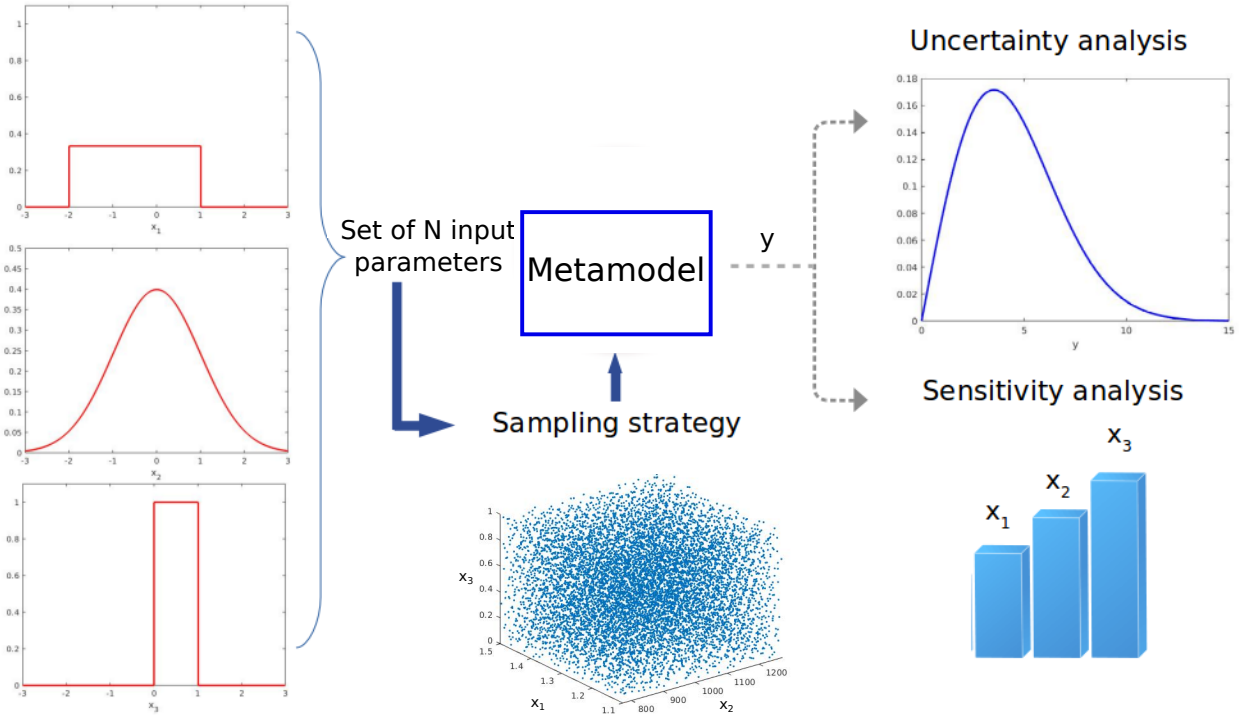

Figure 6.1: Uncertainty quantification on PCE-based metamodel strategy.

In Fig. 6.2 is shown the comparison of the metamodel built with the above-mentioned three different techniques with respect to the real response calculated via the analytical formula. All of them reproduce the output of the model fairly accurately. The major difference between the three techniques from the computational point of view, lies in the number of coefficients calculated and used in order to build the polynomial expansion and to approximate the response of the model. For the same sample's size, are reported in Fig. 6.3 the number of the used coefficients by the OLS, LARS and OMP PCE-based method.

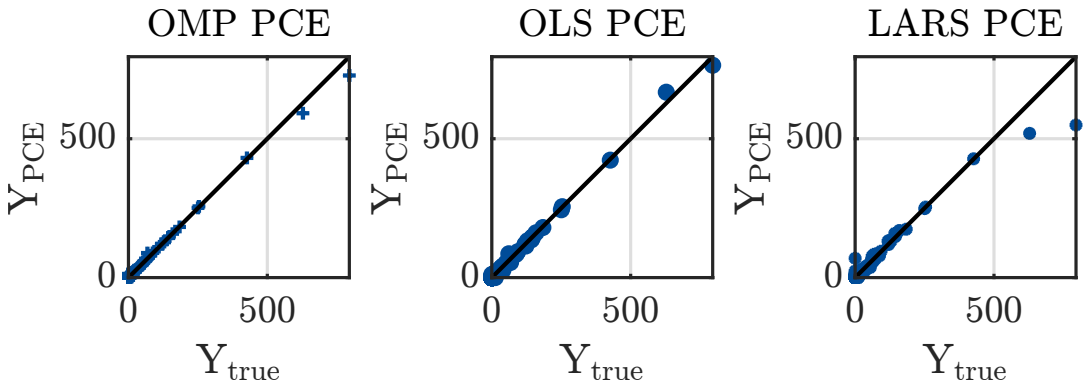

Figure 6.2: True vs. metamodeled responses of the SCG function to a sample of the input of size $N = 10^4$.

Table 6.3: Error comparison between the PCE metamodels techniques w.r.t. the analytical response.

	OLS	LARS	OMP
Modified L-O-O ($N = 10^4$)	$2.36 \cdot 10^{-4}$	$1.46 \cdot 10^{-4}$	$1.16 \cdot 10^{-5}$
Degree	17	19	25
Modified L-O-O ($N = 10^3$)	$6.1 \cdot 10^{-2}$	$1.23 \cdot 10^{-2}$	$1.04 \cdot 10^{-4}$
Degree	9	14	20

The solutions with LARS and OMP produce a smaller number of non-zero coefficients w.r.t. the solution calculated with the OLS technique. The reason lies in the sparse nature of the other two methods. In particular, the LARS solution tends to produce less sparse solutions for this particular model with respect to OMP. In addition, the probability density function of the model's output, such as the time to rupture for the fibre subject to the SCG phenomenon, has been obtained and compared with the one calulated with the numerical model formulation (which is in this case the same calculated with the analytical formula). The results are reported in Fig. 6.4 and show the hyperbolic trend of the fibre failure time.

In Fig. 6.4 are highlighted the trend differences obtained by considering the different techniques for the coefficients computation. Except from a different estimation of the peak, all of them approximate fairly well the evolution of the real response. More precisely, the errors of the built metamodels with respect to the analytical response are reported in Tab. 6.3.

In order to overcome over-fitting, the error indicator chosen here is the leave-one-out cross validation error defined in (6.12).

Considering an experimental design sample of 10^4 points, the OMP-based PCE produces a smaller error compared with the OLS and LARS ones, but with a higher polynomial degree. Moreover, we have also considered a different experimental sample of size 10^3 in

order to compare the obtained metamodel with respect to the real output. The results show a remarkable difference between the error estimated for the OMP PCE with respect to the one obtained through the OLS and LARS formulations.

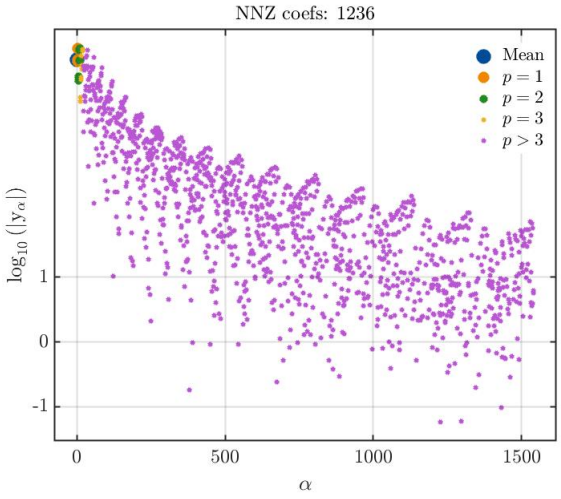

(a) Logarithmic spectrum of the OLS coefficients

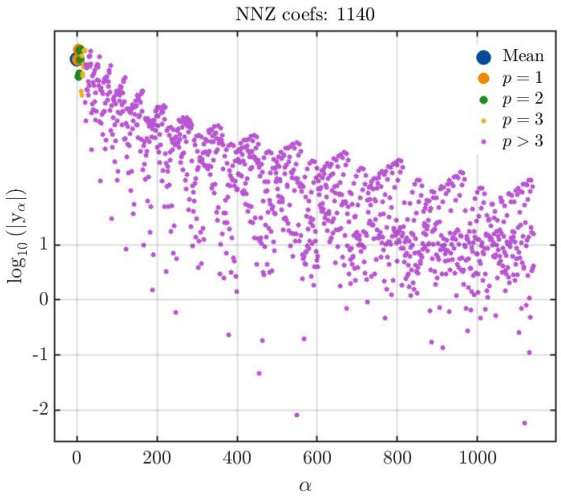

(b) Logarithmic spectrum of the LARS coefficients

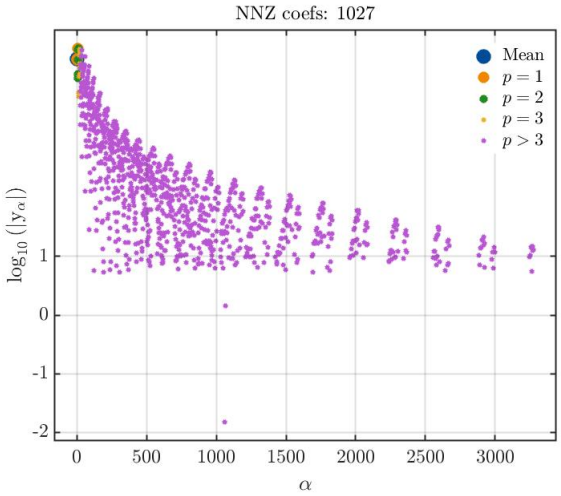

(c) Logarithmic spectrum of the OMP coefficients

Figure 6.3: Graphical representation of the logarithmic spectrum of the PCE coefficients.

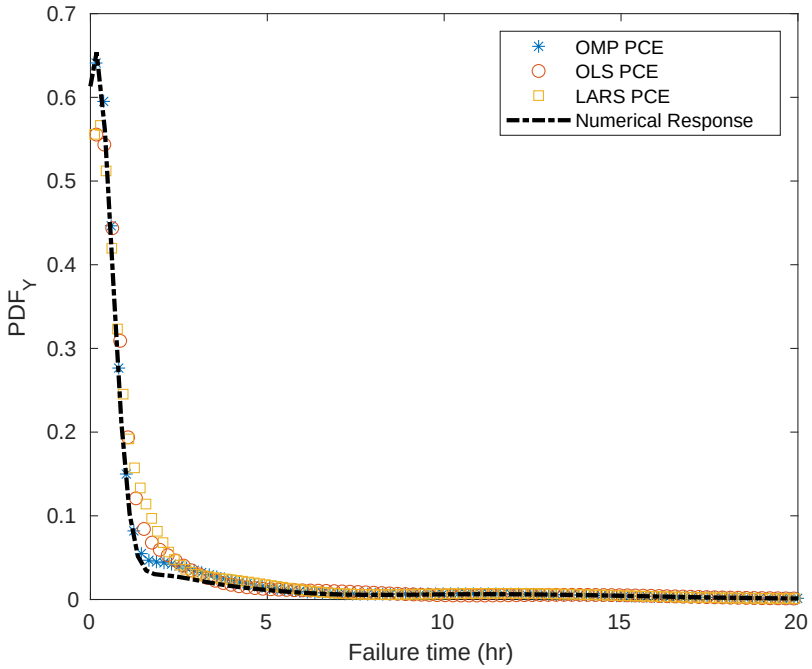

Figure 6.4: Fibre breaking time PDF in SCG modeling calculated with different PCE-based techniques w.r.t. the analytical response.

6.3.1 Sensitivity Analysis On The PCE Metamodel For SCG Problem

The sensitivity analysis based on Sobol' indices has been carried out on the OLS, LARS and OMP PCE, which represent the worst and the best choice respectively in terms of error, and the results compared with the one obtained on the analytical formula using the Monte-Carlo (MC) method. The results of the indices for all three variables match pretty well, as shows Fig. 6.5.

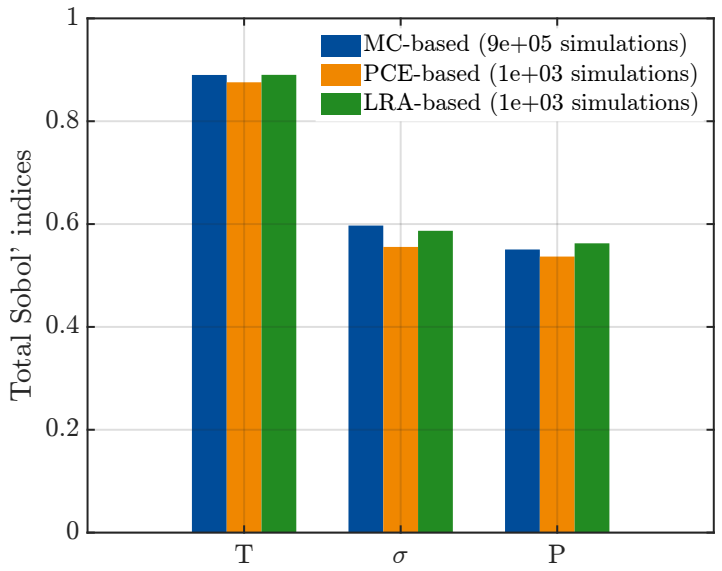

(a) Total Sobol' indices

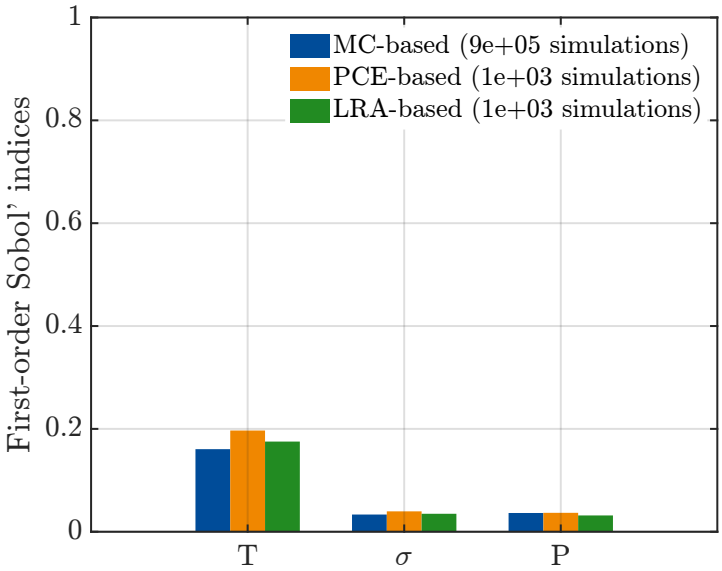

(b) First Sobol' indices

Figure 6.5: Sensitivity Sobol' indices calculated for different PCE metamodels and for the analytical function (N = 10^3).

6.4 PCE metamodel of the global model

In this section, the purpose is to derive the metamodel representative of the whole failure process of the mini-composite subjected to an oxidising environment. In particular, the response evaluated through the metamodel is expressed in terms of the mini-composite's lifetime. As was done in the previous section, the metamodel was built using the PCE technique, i.e. polynomial chaos expansion. As input variables, environmental parameters, such as temperature and partial pressure of oxygen, and the stress conditions were considered in the range of values discussed in the previous chapters. Concerning the failure probabilities of fibres, the following strategy was employed: the tow was divided into sectors and the failure probabilities of each of them were considered as input parameters. This means that all fibres belonging to a sector have the same initial failure probability. In particular, the considered tows have been divided into 3 circular and 8 angular sectors, for a total of 24 sectors. A representation of the division into sectors on tow is given in Fig. 6.6.

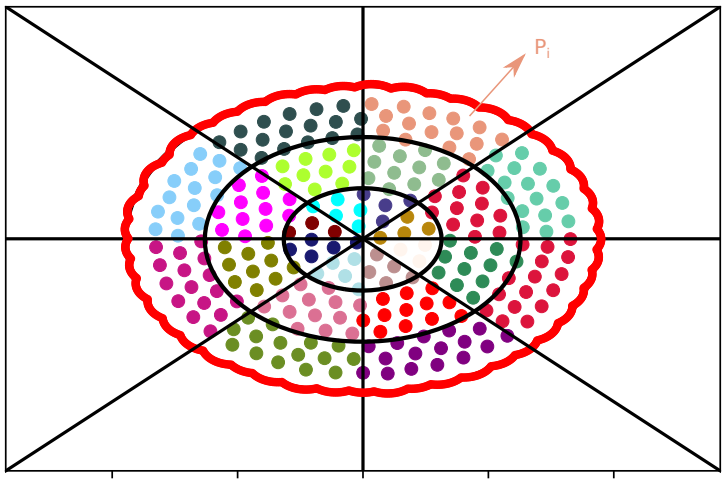

Figure 6.6: Considered sectors in a tow.

The reason behind this solution is that the calculation of the metamodel would have been computationally too heavy and the number of input parameters would have been too large if the probability of rupture of each fibre belonging to the tow had been taken into account. For each of the aforementioned input parameters, a uniform distribution was assumed. In Tab. 6.4 the bounds and distributions of the considered input parameters are shown.

The tow with $AR = 1.00$ shown in Fig. 6.7 was first considered. In order to build the metamodel, an experimental design set of 1000 points was evaluated using a Latin hypercube sampling (LHS) technique. On these points, the response in terms of lifetime was evaluated by means of the numerical model.

Table 6.4: Input parameters and distributions for the global problem.

Name	Distribution	Parameters	Description
T	Uniform	[973.15 - 1273.15]	Temperature [K]
σ	Uniform	[$800{\cdot}10^6$ - $1100{\cdot}10^6$]	Applied stress [Pa]
p_{O_2}	Uniform	[0.1 - 0.9]	Fraction of oxygen partial pressure [Pa]
P_i	Uniform	[$1{\cdot}10^{-6}$ - (1-$1{\cdot}10^{-6}$)]	Failure probability of the i sector

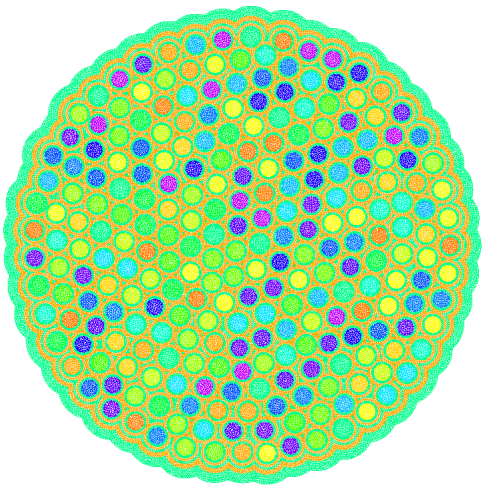

Figure 6.7: Considered tow for metamodel construction, consisting in 251 fibres with aspect ratio (AR) = 1.00.

These data allowed the construction of three type of metamodels made up of 100, 500 and 1000 points respectively, each of them evaluated N times until the probability density function (PDF) of the calculated lifetime fell within a specific bounded area, as shown in Fig. 6.8.

It can be seen that by increasing the number of points for the construction of the metamodel, the above-mentioned area tightens by converging to the probability density function obtained by using the entire set, i.e. 1000 points (see Fig. 6.9). However, the lifetime PDF calculated through the metamodel built with 1000 points was then compared with the lifetime PDF calculated through the numerical code. As is evident in Fig. 6.10 there is a pretty good agreement between the two responses. It is also useful to note that the response range of the metamodel (i.e. the lifetime of the mini-composite) is quite wide. This is due to the bounds of the input parameters we have chosen. Actually, a was demonstrated in chapter 4, for such values of external conditions and load, the lifetime of the mini-composite can be thousands of hours or a few hundred seconds.

In particular, the response points of the metamodel were compared with those obtained through the true model in Fig. 6.11, finding a modified leave-one-out error (see (6.12)) of

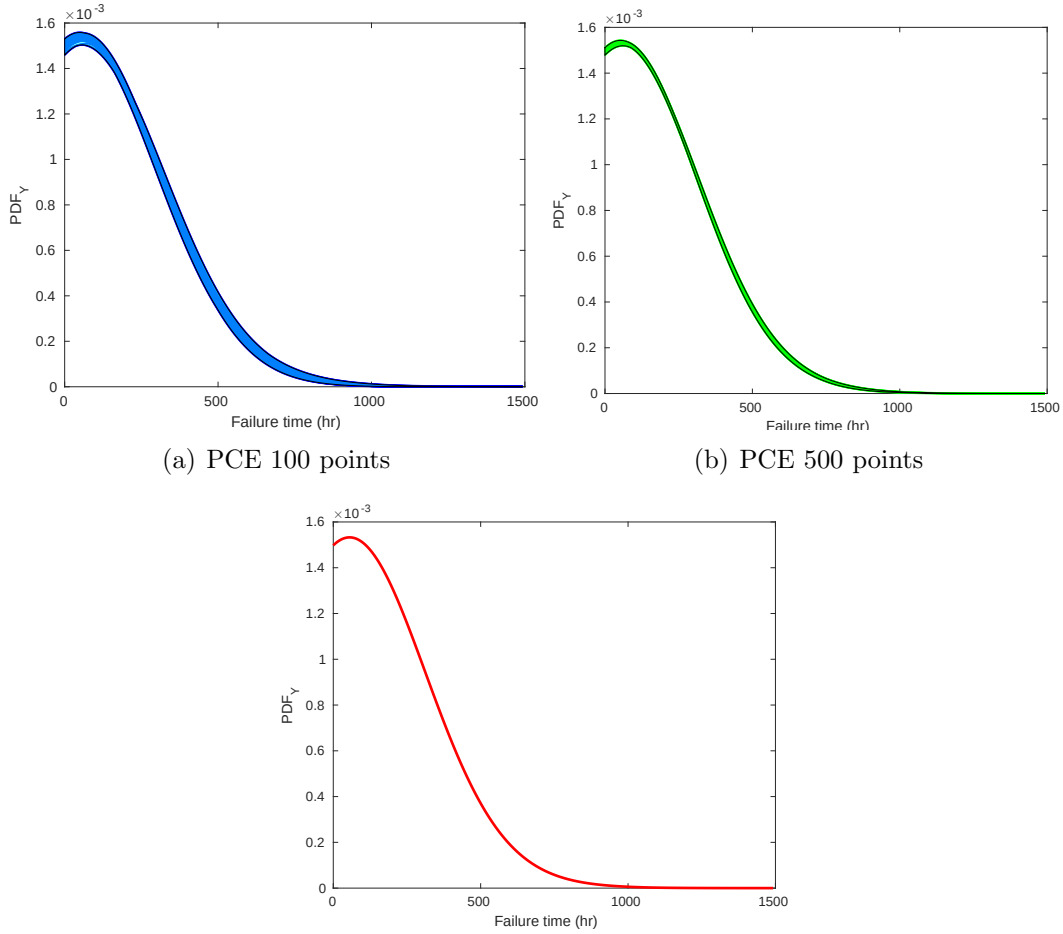

(a) PCE 100 points

(b) PCE 500 points

(c) PCE 1000 points

Figure 6.8: Probability density functions (PDFs) of the mini-composite failure time on validation set (1000 points) computed via different PCE metamodels built with 100, 500 and 1000 experimental design points.

the order 10^{-2}.

On such a metamodel, it is therefore possible to perform a sensitivity analysis of the parameters, through the calculation of Sobol' indices. The first-order Sobol' indices (see Fig. 6.12(a)) and total Sobol' indices (see Fig. 6.12(b)) of the considered input parameters are shown in Fig. 6.12. It is clear that the environmental parameters and the applied load conditions have a clear relevance in the variation of the lifetime compared to the variations of the internal parameters of the tow at fixed conditions.

However, it is also evident when looking at the difference between the first-order and total Sobol' indices that there is a considerable part of interaction between the most relevant parameters, i.e. oxygen partial pressure, applied stress and temperature. These interactions are well expressed in the second order Sobol' indices which are shown in Fig. 6.13. Since the Sobol' indices associated with the probability of sector failure are very

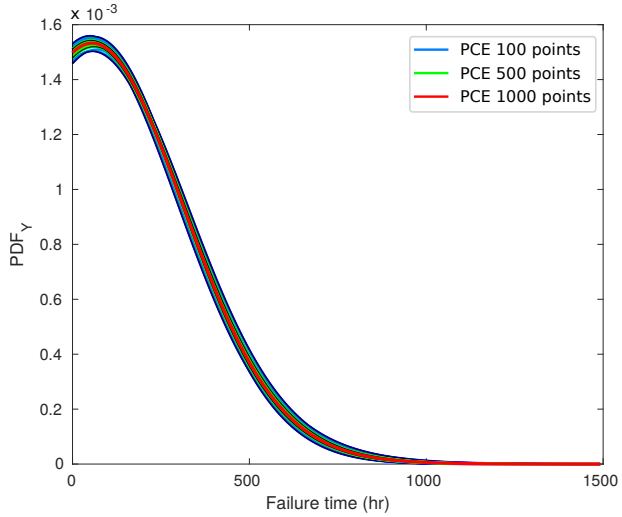

Figure 6.9: Convergence of probability density functions (PDFs) of the mini-composite failure time on validation set (1000 points) computed via different PCE metamodels built with 100, 500 and 1000 experimental design points.

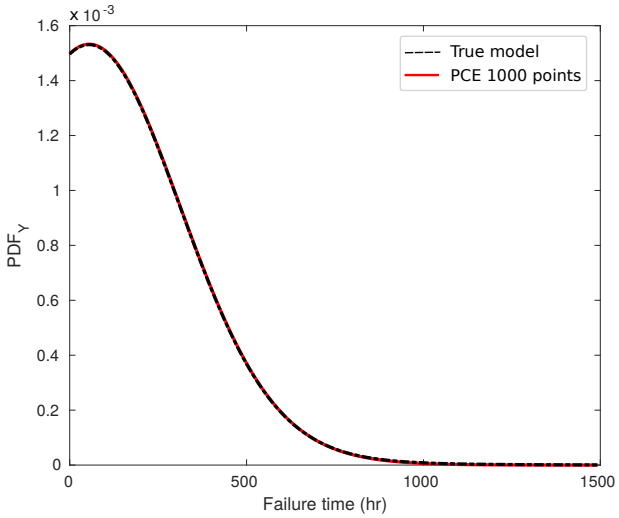

Figure 6.10: Probability density functions (PDFs) of the mini-composite failure time on validation set (1000 points) computed via PCE metamodel built with 1000 points w.r.t. the true PDF of the model.

small (of the order of 10^{-4}) a detailed analysis of their values and a consequent ranking of importance could be distorted due to the order of their differences.

For this reason, it was decided to maintain fixed external conditions (load, temperature and oxygen partial pressure) and to evaluate the variation of the lifetime of the mini-composite only in dependence on the probability distribution of the failure of the sectors within the tow.

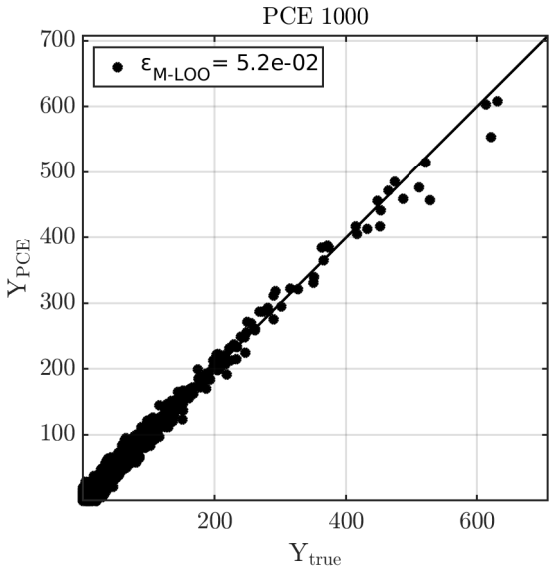

Figure 6.11: Failure time of the mini-composite computed via PCE metamodel built with 1000 points on the experimental design set w.r.t. the true response of the model.

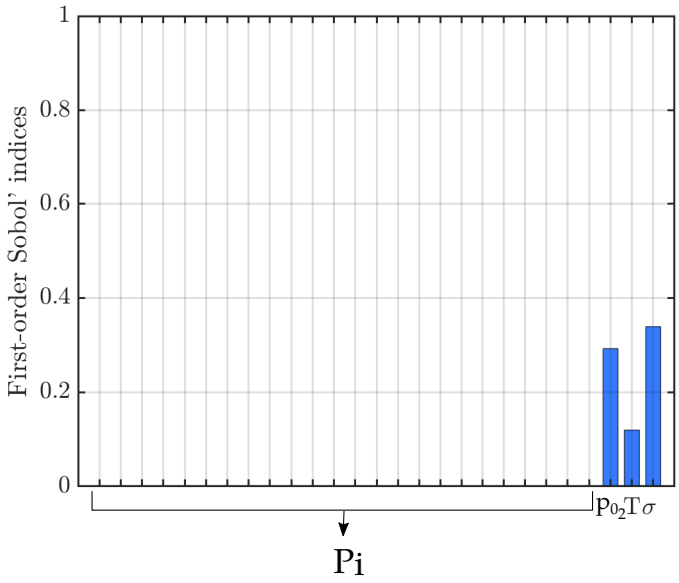

(a)

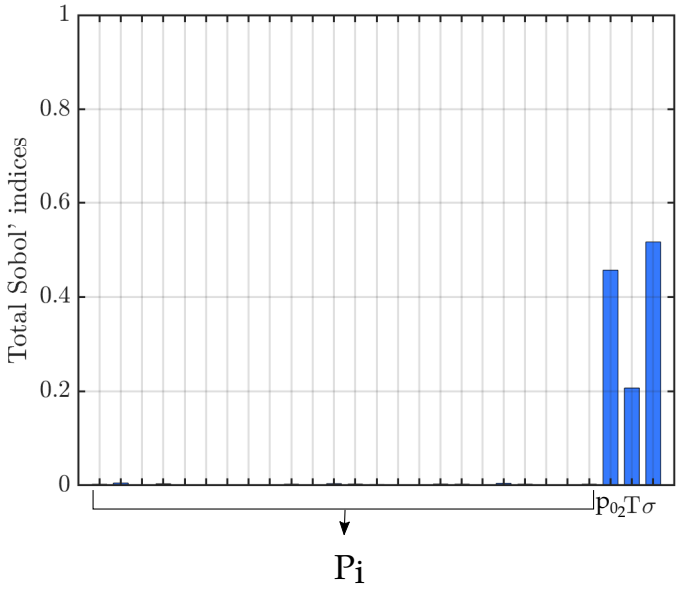

(b)

Figure 6.12: First order and total Sobol' indices for the global problem.

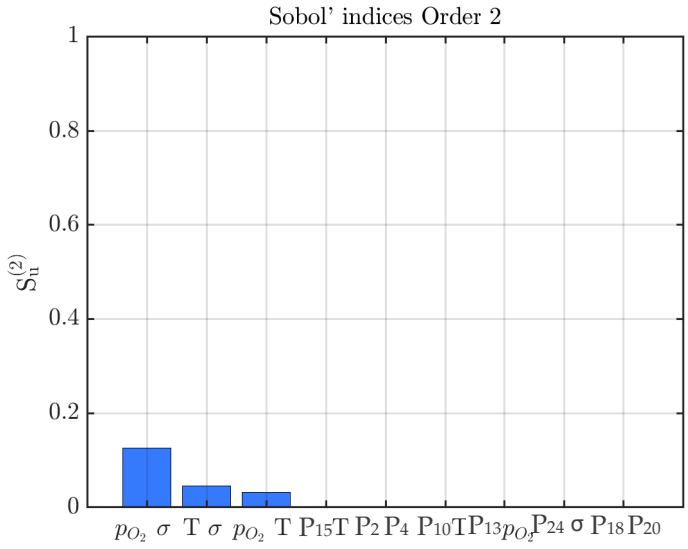

Figure 6.13: Second order Sobol' indices for the global problem.

6.4.1 Constant environmental conditions case

Two metamodels were respectively built on two geometrical configurations of the tow ($AR = 0.25$ and $AR = 1.00$) assuming the same number of fibres (251 fibres), as illustrated in Fig. 6.14. Considering the two extreme cases we are thus able to jointly evaluate the topological and geometrical effect on the lifetime of the mini-composite. The input parameters are represented by the failure probabilities of the fibres of the i sector P_i all with uniform probability distribution and with the same bounds (see Tab. 6.5).

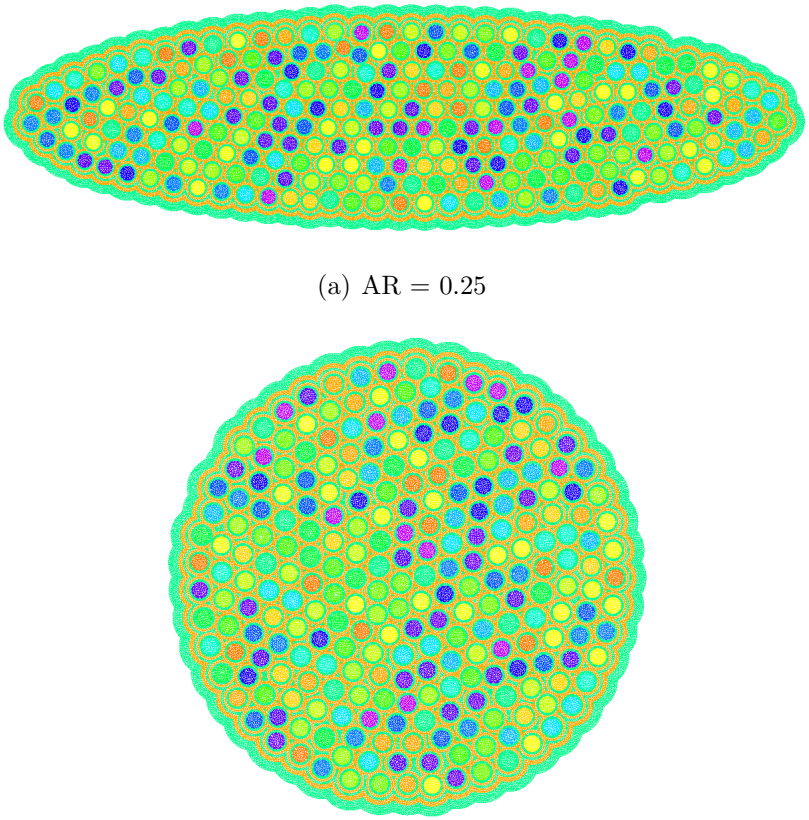

(a) AR = 0.25

(b) AR = 1.00

Figure 6.14: Considered tow for metamodel construction, consisting in 251 fibres with different aspect ratio (AR).

Table 6.5: Input parameters for PCE metamodel construction for fixed external condition.

Name	Distribution	Parameters	Description
P_i	Uniform	$[1 \cdot 10^{-6}$ - $(1$ - $1 \cdot 10^{-6})]$	Failure probability of the i sector

For both configurations ($AR = 0.25$ and $AR = 1.00$), the starting point was the generation of an experimental design set built using the LHS technique and consisting of 1000 points on which the response (Y) in terms of the lifetime of the mini-composite

through the true model was evaluated. From these sets, N metal models were built using 100, 500 and 1000 points respectively from the given set of 1000 points. Also in this case, N is determined by the convergence of the PDFs of the response of the metamodels to a certain area. The PDFs thus generated from the metamodels built with 100, 500 and 1000 points were evaluated on a validation sample also consisting of 1000 points and are shown in Fig. 6.16. Trivially, the PDF evaluated from the metamodel built with 1000 points is unique. The convergence of the metamodels thus built in terms of PDF is given in Fig. 6.15.

Subsequently, the response of the real model on the same sample was calculated and compared in terms of PDF (Fig. 6.17) and an excellent agreement was found. The response of the metamodel built with 1000 points was then compared with the response of the real model on the set of construction points.

The response of the metamodel built with 1000 points was then compared with the response of the real model on the set of construction points. As Fig. 6.18 shows, the responses of the metamodel are close to those obtained through the real model except for a few points at the upper end of the response and its leave-one-out error is of the order of 10^{-2}. It was therefore possible to perform a sensitivity analysis of the input parameters on this metamodel by calculating the Sobol' indices associated with them.

The first-order Sobol' indices associated with the fibres in each sector are illustrated in Fig. 6.19. They show that for the tow with $AR = 1.00$, the initial strengths of the fibres placed in the intermediate circular ring globally have a greater impact on the lifetime of the mini-composite. Indeed, the fibres placed in the first ring, being those closest to the oxygen source, are the first to be degraded and to fail regardless of their initial strength. Indeed, the growth of their critical defect is proportional to the concentration of oxygen at the fibre. Subsequently, as the tow is protected by the plug formed by the oxide, and the diffusion of oxygen is slowed down, the degradation of the fibres in the intermediate layer is slower. Therefore, the initial values of fibre strength in these sectors are more significant. Once the fibres in the intermediate sectors break, the whole mini-composite fails and therefore the initial probability of failure of the inner sectors becomes irrelevant.

On the other hand, if we look at the values of the Sobol' indices associated with the sectors in the case of the tow with $AR = 0.25$ represented in Fig. 6.19(b) the situation is totally different. Indeed, in this case the radial symmetry obtained in the previous case is lost since there are two characteristic lengths, represented by the major and minor semi-axes. The sectors that have more influence are those of the first layer along the major semi-axis and those of the second layer along the minor semi-axis. Indeed, along the minor semi-axis, oxygen diffuses over a path four times shorter and therefore reaches

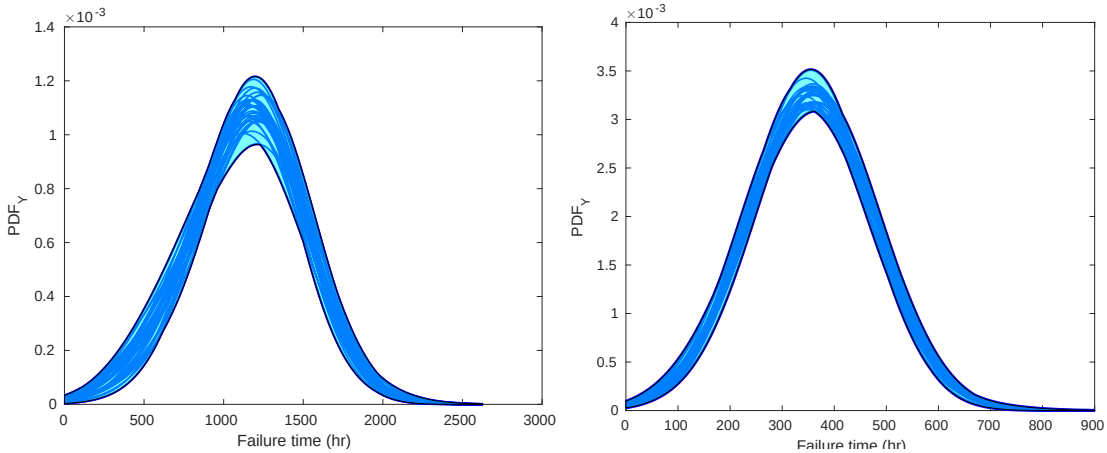

(a) PCE 100 points, AR = 1.00

(b) PCE 100 points, AR = 0.25

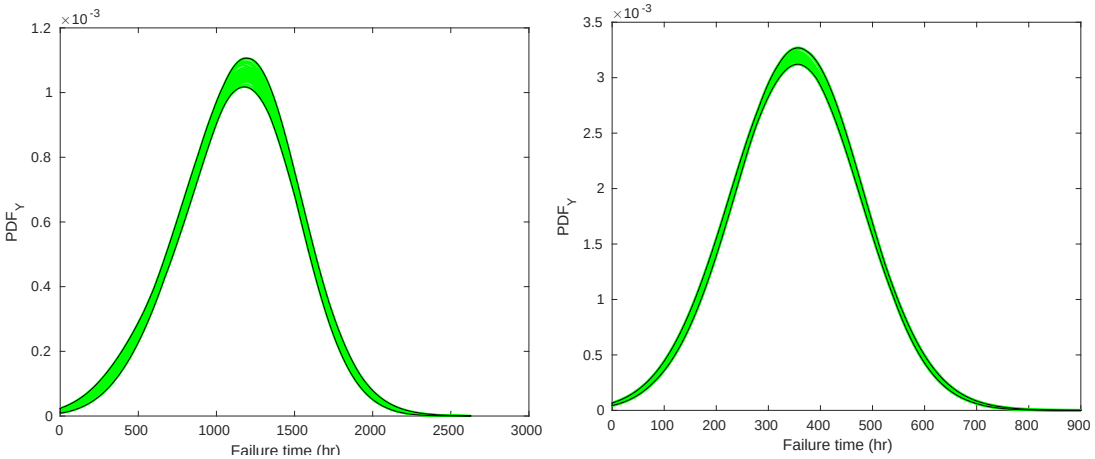

(c) PCE 500 points, AR = 1.00

(d) PCE 500 points, AR = 0.25

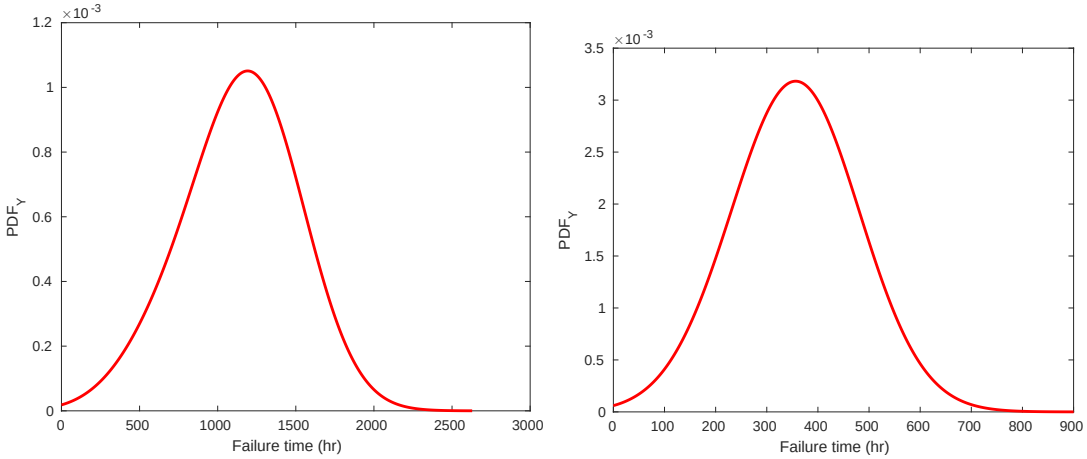

(e) PCE 1000 points, AR = 1.00

(f) PCE 1000 points, AR = 0.25

Figure 6.15: Probability density functions (PDFs) of the mini-composite failure time on validation set (1000 points) computed via different PCE metamodels built with 100, 500 and 1000 experimental design points for tow with $AR = 1.00$ and $AR = 0.25$.

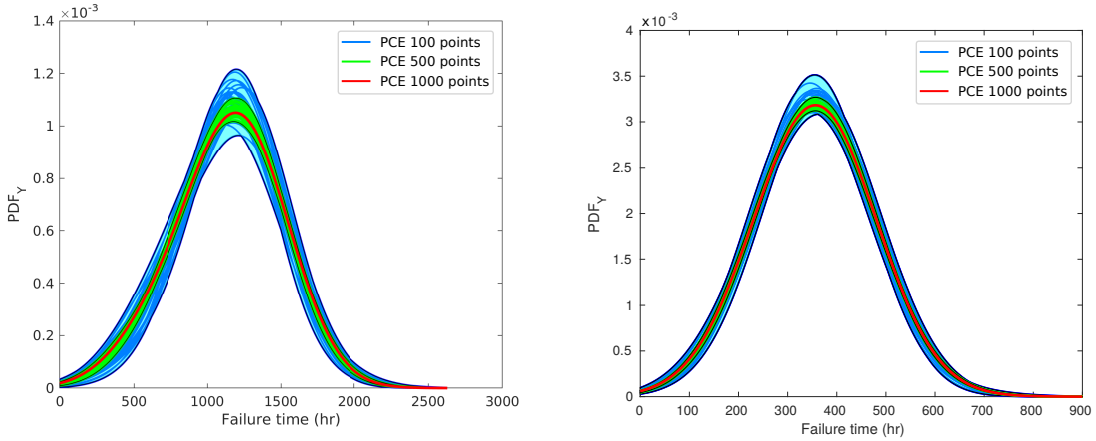

(a) AR = 1.00 (b) AR = 0.25

Figure 6.16: Convergence of probability density functions (PDFs) of the mini-composite failure time on validation set (1000 points) computed via different PCE metamodels built with 100, 500 and 1000 experimental design points for tow with $AR = 1.00$ and $AR = 0.25$.

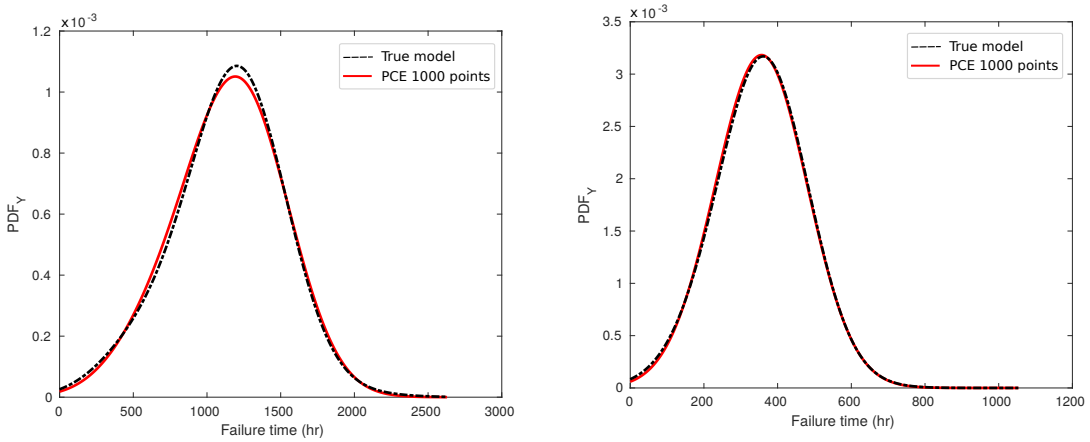

(a) AR = 1.00 (b) AR = 0.25

Figure 6.17: Probability density functions (PDFs) of the mini-composite failure time on validation set (1000 points) computed via PCE metamodel built with 1000 points w.r.t. the true PDF of the model for tow with $AR = 1.00$ and $AR = 0.25$.

the second layer immediately. If the fibres in these sectors are broken, the oxygen has access to the other intermediate layers of the tow, operating thus in a different direction. The first layer on the semi-major axis is more important as it extends over a fairly large area. In this case, however, a symmetry of results can be seen along the minor axis of the tow. Furthermore, considering the values of the total Sobol' indices in Fig. 6.20, it can be noted that they are almost equal to those of the first order and therefore the interactions between the sectors are almost irrelevant.

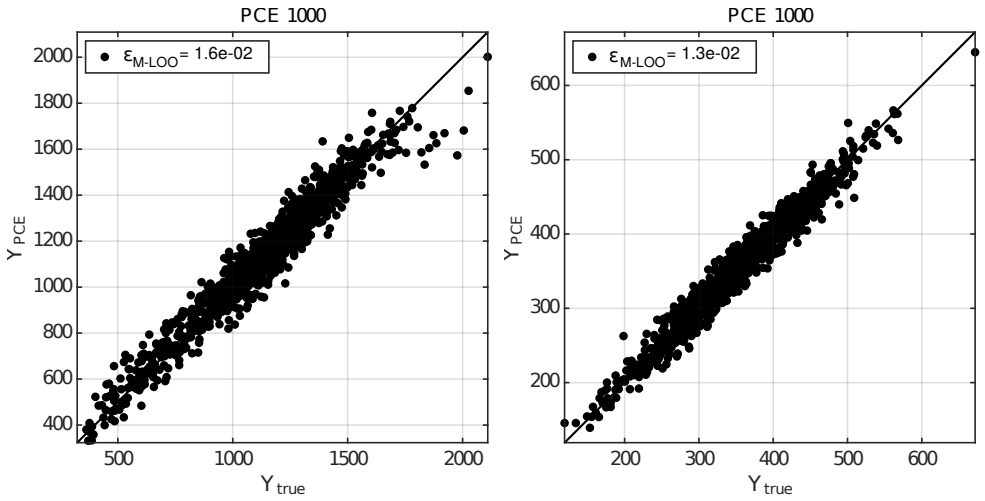

(a) AR = 1.00 (b) AR = 0.25

Figure 6.18: Failure time of the mini-composite computed via PCE metamodel built with 1000 points on the experimental design set w.r.t. the true response of the model for tow with $AR = 1.00$ and $AR = 0.25$.

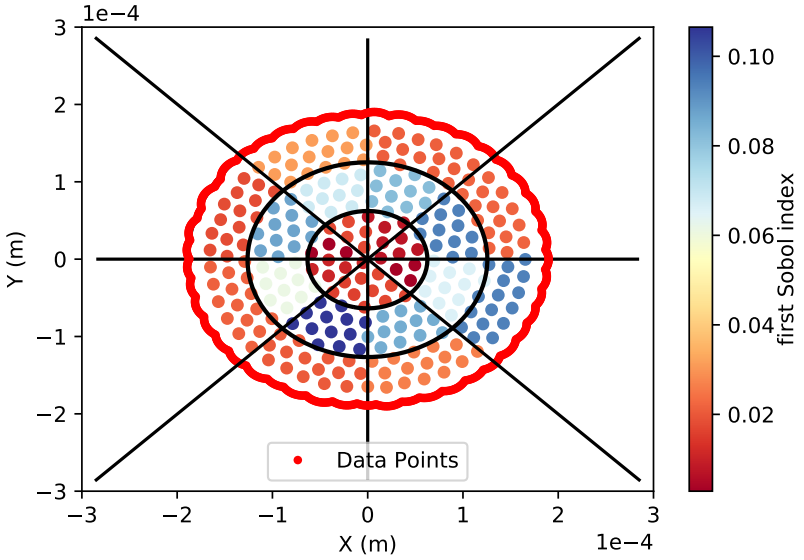

(a) AR = 1.00

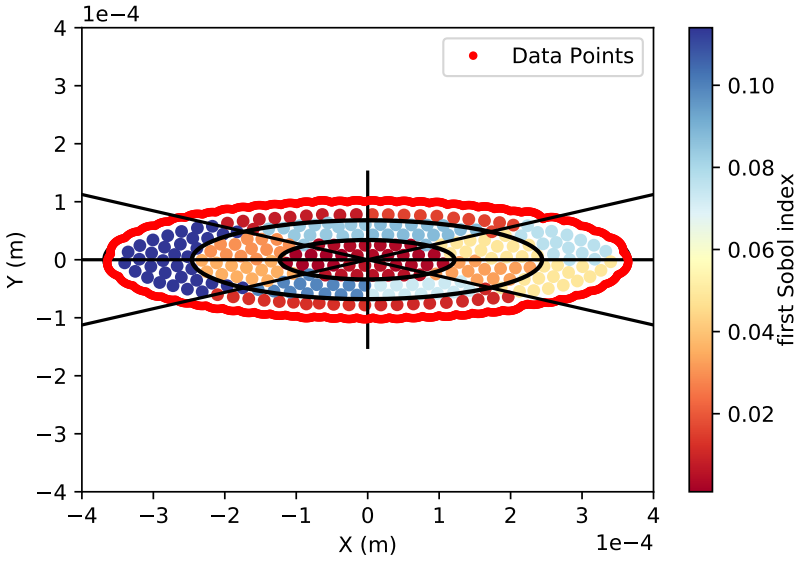

(b) AR = 0.25

Figure 6.19: First order Sobol' indices for the global problem for tow with $AR = 1.00$ and $AR = 0.25$.

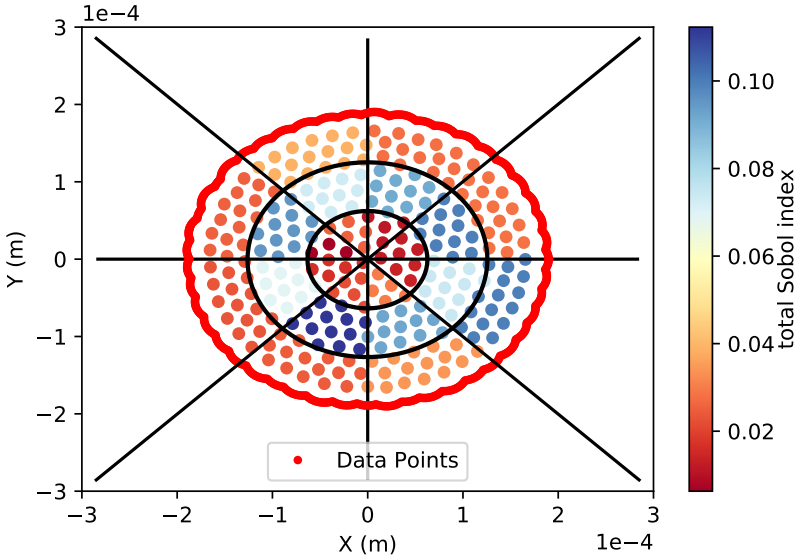

(a) AR = 1.00

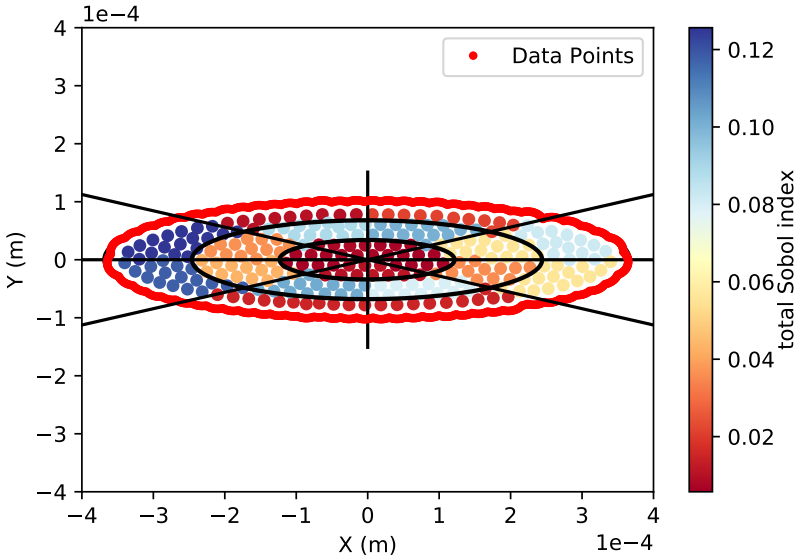

(b) AR = 0.25

Figure 6.20: Total Sobol' indices for the global problem for tow with $AR = 1.00$ and $AR = 0.25$.

6.5 Chapter summary

In this chapter, the uncertainty study and sensitivity analysis of three different models were presented: sub-critical crack propagation model, global model of the multi-physics problem for calculating the lifetime of a mini-composite SH-CMC under variable and constant external conditions. This study was possible through the building of respective PCE-based metamodels. Firstly, this study allowed to validate the metamodel built for the calculation of the sub-critical propagation through the comparison of the Sobol' indices obtained through the analytical formulation derived in chapter 3. Furthermore, this analysis permitted to highlight the most influential parameters in terms of lifetime for the considered problem. Subsequently, these parameters were used as input for the construction of the representative metamodel of the global process, obtaining a good representation of the response compared to that calculated with the true model. The sensitivity study on this metamodel has confirmed the strong influence of the external parameters in the determination of the mini-composite lifetime. Therefore, a study was performed taking into consideration only the internal and a priori defined parameters in order to evaluate the spatial influence of the fibre distribution in the tow for different tow configurations. The established metamodels for this purpose were validated with the response obtained through the true model, showing an excellent agreement. Finally, the sensitivity study performed on these metamodels demonstrated that the fibre sectors with the greatest influence on the mini-composite lifetime differed according to the configuration, and in particular the aspect ratio, of the considered tow.

Chapter 7

General conclusions and future works

7.1 Conclusions

This thesis aims to contribute to the modelling part concerning the behaviour and lifetime of self-healing CMC materials. In particular, it has the objective of developing a suitable multi-physics model for such materials from an image-based two-dimensional representation of a transverse crack within the mini-composite. The multi-physics model presented here can accurately describe the physico/chemical phenomena occurring in the crack over time, particularly the oxygen concentration field, the regression of the reactive matrix layers and the related oxide production, and the oxidation of the interphase around the fibres. This version is modified with respect to the work in [81] since, thanks to a dimensional analysis of the PDE describing the system, it was possible to make a suitable choice on the integration step, which is not a compromise between the two characteristic times of the problem. In particular, it was found that the diffusion/reaction process for the oxygen concentration can be assumed quasi-stationary. Thus it is possible to adapt the time step of the complete self-healing problem to follow the evolution of the oxide height. This choice solves a significant problem of the two-dimensional description of the self-healing process, i.e. the computational time required. In fact, previous work on modelling and describing the oxide-production mechanisms was developed in $OD/1D$ for this reason, resulting in an analytical solution that is easy to implement.
The numerical implementation approach presented in this thesis has thus enabled the computational time per simulation to be considerably reduced to a few minutes, allowing important information relating to the processes occurring in the crack not to be lost. In particular, the model highlighted the radial pattern of oxygen diffusion (diffusion occurs

from the outside to the inside of the tow), and the relative oxidation depending on the position of the various elements in the crack. As a result, this suggests the importance of taking into account the different topologies of the tow in order to evaluate their lifetime. This model has been coupled for the first time with a descriptive model of the sub-critical propagation of defects in the fibres [56] which explicitly links the environmental conditions inside the crack instant by instant to the fibre strength. This provided the opportunity to study how the mechanism of the propagation of defects in the fibres evolves in a self-healing crack context, i.e. taking into account the different oxygen diffusion rates for the gas or oxide diffusion phase, and the consequent degradation rate of the fibres.

Furthermore, in the present thesis, the descriptive analytical formula of the sub-critical propagation problem obtained in the case of constant external oxygen concentration was derived. It made it possible to calibrate the model and to perform a sensitivity analysis on the parameters involved in order to test the stability and to show the influence they have on the lifetime of the fibres. In particular, the model was stable concerning small variations in diffusive/kinetic parameters but highly sensitive to parameters defining external conditions such as temperature, applied stress and oxygen partial pressure. The multi-physics model described here is completed by integrating an analytical model for calculating the load distribution on the mini-composite and the progressive failure of the fibres.

Furthermore, by working on a two-dimensional domain it was possible to highlight the link between the naturally scattered fibre strength distribution and the computed physico-chemical variables inside tow and demonstrate how the failure scenario changes. Since this model is explicitly dependent on environmental and load parameters, it was, therefore, possible to analyse the changes in the lifetime of the mini-composite as a function of these parameters and the associated failure history. In particular, conditions (of stress and temperature) were highlighted for which the intrinsically stochastic nature of the problem leads to a bimodal behaviour of the mini-composite's lifetime. In fact, it has been shown that under such conditions the lifetime of the mini-composite can be thousands of hours or a few seconds depending on the initial strength properties of the fibres.

Moreover, it was shown that the fibre failure scenario is greatly influenced by the oxide presence, highlighting the fundamental role of the topological description of the fibre strength distribution in the tow. However, it should be noted that the absence of experimental tests at this scale on these SH-CMCs allowed analysing of the results obtained from a purely qualitative point of view. The stochastic nature of the problem made it possible to conduct multiple simulations that also gave us information on the

dispersion of the results in terms of lifetime. Considering this strong relationship between the tow failure scenario and the positioning of the fibres, it was possible to analyse the failure scenario of a tow with different shape and size configurations. In particular, it was shown how the lifetime is proportionally related to the aspect ratio of the tow considered, highlighting the importance of the geometric description of the mini-composite in the calculation of the lifetime. In particular, through the definition of scale and shape factors, calculated from reference lifetimes, the dependence on the minimum characteristic length associated with the tow was highlighted.
Understanding the main characteristics of the mini-composite that affect its lifetime and especially in which way they operate, it was therefore possible to obtain an estimate lifetime of different mini-composite configurations based purely on these information. This concept led naturally to the formal formulation of the sensitivity related to the main parameters involved in the SH mini-composite lifetime computation. It was therefore possible to build a PCE-based surrogate model that exactly (or almost) reproduces the lifetime of the mini-composite as the assigned input parameters change. The sensitivity analysis performed on the metamodel once again showed the great influence of the prediction of the lifetime by external conditions, such as temperature, oxygen partial pressure and applied stress. Therefore, a metamodel with constant environmental conditions was built in order to evaluate the spatial influence of the fibre strength distribution in the tow. The sensitivity analysis performed on this metamodel, fortunately, confirmed and formalised what had previously been deduced. A very interesting outcome of this study is that a spatial variation of the most influential parameters was found as the geometry of the mini-composite changed, highlighting different failure mechanisms and scenarios.

7.2 Future works

The described logical flow naturally leads to some considerations on possible future directions of work:

1. The analysis of the sensitivity of topological, geometrical, size and diffusive/kinetic parameters on the lifetime prediction opens the way to a possible upscaling of the problem analysed here on the mini-composite. The identification of these parameters could therefore allow a reduced model to be developed and integrated in multi-scale approach.

2. Concerning the multi-physical model developed for the calculation of the lifetime, it

could be integrated and enriched in the mechanical failure part by implementing different, more detailed microscopic damage approaches. This would allow a more complete and interesting field of mechanical variables to be analysed coupled with the other bricks of the model proposed in this thesis.

3. In modelling the behaviour and lifetime of the mini-composite under the temperature conditions analysed, it would be very interesting to consider more complex environmental conditions. For example, it would be useful to investigate the variation of the lifetime of the composite under humid air conditions by implementing a model describing the phenomenon of volatilisation in the crack. The equations for such a model are similar to those given in this thesis and already written in [80] with the addition of an equation describing the kinetics of volatilisation. The description of this phenomenology would also allow an extension of the sub-critical defect propagation model reliable for this case.

4. Having developed a multi-physics model in this thesis that is explicitly dependent on the parameters involved, it would be easily feasible and interesting to change the materials and thus the composition of the mini-composite in order to assess its effects on the lifetimes. For example, it would be possible to assess the behaviour of the mini-composite with different interphase, such as BN interphase, or even to add/change the matrix layers considered.

Appendices

A.1 Vertical averaging for 2D diffusion equation in thin cracks

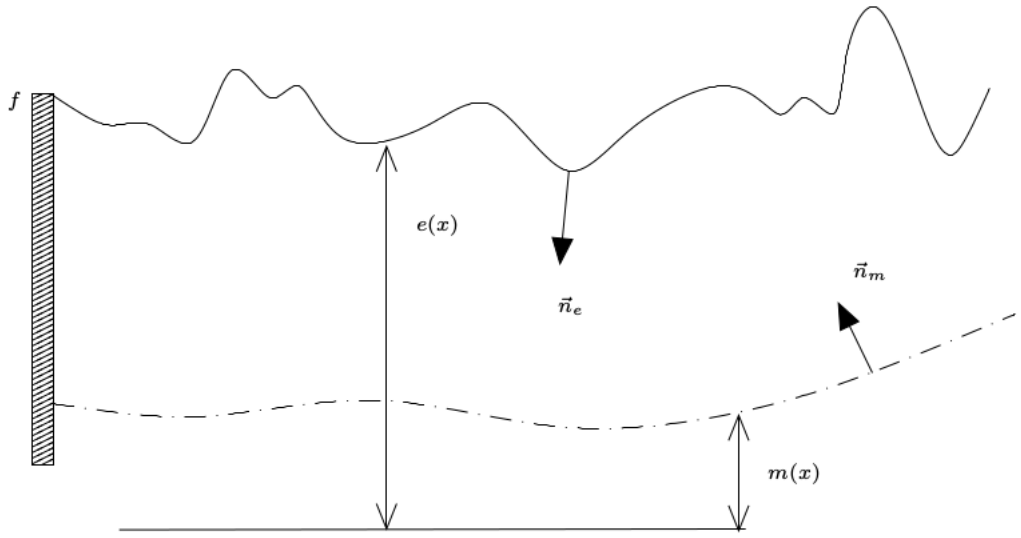

Figure 1: Geometrical sketch for the diffusion through a thin crack.

We want to derive an approximate averaged model for the diffusion of a gas through a very thin crack, as the one depicted in Fig. 1. By very thin we mean that the ratio between the typical length scale in the horizontal direction L and the characteristic height of the crack δ is $\delta/L \approx 10^{-3}$ - 10^{-2} . We shall set:

$$\epsilon_{ef} = \frac{e_f}{L} \approx 10^{-3} - 10^{-2} \text{ and } \epsilon_{ef}^2 \approx 10^{-6} - 10^{-4} \tag{1}$$

With reference to Fig. 1, we note that the unit vectors $\overrightarrow{n}_m$ and $\overrightarrow{n}_e$ are obtained as:

$$\overrightarrow{n}_e = \frac{(\partial_x e,) - 1}{\sqrt{1 + (\partial_x e)^2}}, \overrightarrow{n}_m = \frac{(-\partial_x m,) - 1}{\sqrt{1 + (\partial_x m)^2}} \tag{2}$$

Consider now the two-dimensional problem:

$$\begin{cases} \partial_t C + \nabla \cdot F = 0 \\ F = -D\nabla C \end{cases} \quad \text{with} \quad \begin{cases} F(x, m(x), t) \cdot \overrightarrow{n}_m = 0 \\ F(x, e(x), t) \cdot \overrightarrow{n}_e = 0 \end{cases} \tag{3}$$

and with one extra Neumann condition on the left boundary and a Dirichlet condition on the right boundary. Given the hypothesis on the height of the crack, we want to replace the two-dimensional problem (3) by an averaged one-dimensional equation obtained as:

$$\int_{m(x)}^{e(x)} (\partial_t C + \nabla \cdot F)\, dy = 0 \tag{4}$$

Before proceeding further we recall the following Leibniz rule on integral with variable extrema:

$$\int_{a(x)}^{b(x)} \partial_x f(t,x) dt = \partial_x \left[\int_{a(x)}^{b(x)} f(t,x) dt \right] - (f(b(x),x)b'(x) - f(a(x),x)a'(x))) \tag{5}$$

A.1.1 Vertical averaging for derivatives and boundary conditions

Application of the Leibniz rule to the vertical integral gives immediately:

$$\begin{aligned} \partial_x \left(\int_{m(x)}^{e(x)} C(x,y,t) dy \right) + \partial_x \left(\int_{m(x)}^{e(x)} F_x(x,y,t) dy \right) - (F_x(x, e(x,t)e'(x)) + \\ - F_x(x, m(x), t)m'(x)) + F_y(x, e(x), t) - F_y(x, m(x), t) = 0 \end{aligned} \tag{6}$$

having considered the independence of m and e on time. Using the boundary conditions in (3), the last equation can be immediately recast as:

$$\begin{aligned} \partial_t \left(\int_{m_(x)}^{e(x)} C(x,y,t) dy \right) + \partial_x \left(\int_{m(x)}^{e(x)} F_x(x,y,t) dy \right) = \alpha(x) F(x, e(x), t) \cdot \overrightarrow{n}_e + \\ - \beta(x) F(x, m(x), t) \cdot \overrightarrow{n}_m \end{aligned} \tag{7}$$

where $\alpha(x) = \sqrt{1 + (\partial_x e)^2}$ and $\beta(x) = \sqrt{1 + (\partial_x m)^2}$

A.1.2 Vertical averaging for 2D diffusion, boundary conditions and final model

To complete the development we must compute the vertical average of the horizontal flux, as:

$$\int_{m(x)}^{e(x)} F_x(x,y,t)dy = -D\partial_x\left(\int_{m(x)}^{e(x)} C(x,y,t)dy\right)+D\left(C(x,e(x),t)e'(x)-C(x,m(x),t)m'(x)\right) \tag{8}$$

Let us define the following quantities:

$$h_g(x) = e(x) - m(x), \quad e_f(x)\overline{C}(x,t) = \textstyle\int_{m(x)}^{e(x)} C(x,y,y)dy \tag{9}$$

The model can be written as:

$$\partial_t\left(h_g(x)\overline{C}(x,t)\right)-\partial_{xx}\left(Dh_g(x)\overline{C}(x,t)\right) = -\partial_x\left(DC(x,e(x),t)e'(x)-DC(x,m(x),t)m'(x)\right) \tag{10}$$

To proceed further, we invoke the mean value theorem, which allows to write:

$$\overline{C}(x,t) = C(x,\overline{y}(x),t) \quad \text{with} \quad m(x) \le \overline{y}(x) \le e(x) \tag{11}$$

We then perform the following truncated developments:

$$\overline{C} = C(x,e,t) - (e-\overline{y})\partial_y C\left(x,(e(x),t\right) + \mathcal{O}\left((e-\overline{y})^2\right) \tag{12}$$

and

$$\overline{C} = C(x,m,t) + (\overline{y}-m)\partial_y C\left(x,(m(x),t\right) + \mathcal{O}\left((\overline{y}-m)^2\right) \tag{13}$$

By virtue of the boundary conditions in (3) these developments can be recast as

$$\overline{C} = C(x,e,t) - (e-\overline{y})\partial_x C\left(x,(e(x),t\right)e'(x) + \mathcal{O}\left((e-\overline{y})^2\right) \tag{14}$$

and

$$\overline{C} = C(x,m,t) + (\overline{y}-m)\partial_x C\left(x,(m(x),t\right)m'(x) + \mathcal{O}\left((\overline{y}-m)^2\right) \tag{15}$$

Passing to non-dimensional variables, using L as a x length scale, and δ for the vertical lengths such as y, e and m, we obtain:

$$\overline{C} = C(x,e,t) - \epsilon_{ef}^2(e-\overline{y})\partial_x C(x,e(x),t)e'(x) + \text{higher order terms} \tag{16}$$

and

$$\overline{C} = C(x,m,t) - \epsilon_{ef}^2(\overline{y}-m)\partial_x C(x,m(x),t)m'(x) + \text{higher order terms} \tag{17}$$

where we recall that all the quantities in the last two expressions are non-dimensional. The final result is that up to $\mathcal{O}\left({\epsilon_\delta}^2\right)$ our simplified model is:

$$\partial_t(h_g(x)\overline{C}(x,t)) + \partial_x(a(x)\overline{C}(x,t)) = \partial_{xx}\left(Dh_g(x)\overline{C}(x,t)\right) \quad \text{with} \quad a(x) = Dh_g'(x) \tag{18}$$

We have obtained a conservation law with spatially varying fluxes and diffusion. The last equation can be recast in several other useful forms. One of these is the advection diffusion reaction equation:

$$\partial_t u(x,t) + b(x)\partial_x u(x,t) = \partial_{xx}(Du(x,t)) - b'(x)u(x,t) \quad \text{with} \quad u = h_g\overline{C},\ b(x) = D\frac{h_g'}{h_g} \tag{19}$$

and the advection-diffusion form:

$$\partial_t\overline{C}(x,t) + \lambda(x)\partial_x\overline{C} = D\partial_{xx}\overline{C}(x,t) \quad \text{with} \quad \lambda(x) = -\frac{Dh_g'}{h_g} \tag{20}$$

and finally the variable coefficients diffusion equation:

$$\partial_t(h_g(x)\overline{C}(x,t)) = \partial_x(Dh_g(x)\partial_x\overline{C}(x,t)) \tag{21}$$

A.2 Analytical solution for SCG problem

Given the following system:

$$\begin{cases} \dot{a}(t) = \dfrac{1}{(\lambda K_c)^{1/n}} \cdot \dfrac{k \cdot C}{(1 + k \cdot e(t)/D)} \cdot \sigma^{1/n} Y^{1/n} \sqrt{a(t)}^{1/n} \\ \dfrac{de}{dt} = -\dfrac{\rho}{M} \cdot \dfrac{k \cdot c_0(t)}{(1 + k \cdot e(t)/D)} \\ e(t=0) = 0 \\ a(t=0) = a_0(\sigma_R) \\ a(t=t_R) = a_c(\sigma) \end{cases} \tag{22}$$

we want to derive the solution in the case where C is constant ($C = c_0$). Starting from the equation for SiO_2 oxide growth:

$$\dot{e} = \frac{\rho}{M} \cdot \frac{k c_0}{(1 + ke/D)} \tag{23}$$

$$(1 + ke/D)\, \dot{e} = \frac{\rho}{M} k c_0 \tag{24}$$

if $t_0 = 0$

$$e + \frac{k}{D}\frac{e^2}{2} = \frac{\rho}{M} k c_0 t \tag{25}$$

$$e^2 + \frac{2D}{k} e - \frac{2D}{k}\frac{\rho}{M} k c_0 t = 0 \tag{26}$$

$$e^2 + \frac{2D}{k} e - \frac{2D\rho}{M} c_0 t = 0 \tag{27}$$

We then get:

$$\Delta = \left(\frac{2D}{k}\right)^2 - 4\left(\frac{2D\rho}{M} c_0 t\right) = \left(\frac{D}{k}\right)^2 + 2\left(\frac{D\rho}{M} c_0 t\right) \tag{28}$$

and the respective solutions as:

$$e_{1-2} = -\frac{D}{k} \pm \sqrt{\left(\frac{D}{k}\right)^2 + 2\left(\frac{D\rho}{M} c_0 t\right)} \tag{29}$$

The solution has to increase with respect to time. For this reason, only the positive solution is considered.

$$\frac{de}{dt} = \frac{1}{2}\frac{\frac{2D\rho c_0}{M}}{\sqrt{\left(\frac{D}{k}\right)^2 + \frac{2D\rho c_0 t}{M}}} = \frac{D\rho c_0}{M\sqrt{\left(\frac{D}{k}\right)^2 + \frac{2D\rho c_0 t}{M}}} \tag{30}$$

The first differential equation of the system is solved as follows:

$$\frac{da}{dt} = \frac{1}{\lambda^{\frac{1}{n}} K_c^{\frac{1}{n}}} \frac{kc_0}{1 + k\frac{e(t)}{D}} \left(\frac{\rho}{M}\right)\left(\frac{M}{\rho}\right) \cdot \sigma^{1/n} Y^{1/n} \sqrt{a}^{1/n} \tag{31}$$

In the previous equation, the term $\frac{kc_0}{1+k\frac{e(t)}{D}}\left(\frac{\rho}{M}\right)$ correspond to the second equation of the system. Thus, Eq. (31) can be simplified as follows:

$$\frac{da}{dt} = \frac{\sigma^{1/n} Y^{1/n} \sqrt{a}^{1/n}}{\lambda^{1/n} K_c^{1/n}} \cdot \frac{D\rho c_0}{M\sqrt{\left(\frac{D}{k}\right)^2 + \frac{2D\rho c_0 t}{M}}} \cdot \left(\frac{M}{\rho}\right) \tag{32}$$

$$\frac{1}{a^{\frac{1}{2n}}}\frac{da}{dt} = \frac{d}{dt}\left(\frac{1}{1-\frac{1}{2n}} a^{1-\frac{1}{2n}}\right) = \frac{d}{dt}\left(\frac{2n}{2n-1} a^{\frac{2n-1}{2n}}\right) = \left(\frac{\sigma Y}{\lambda K_c}^{1/n}\right)\frac{d}{dt}\left(2\frac{M}{\rho}\sqrt{\left(\frac{D}{k}\right)^2 + \frac{2D\rho c_0}{M}t}\right) \tag{33}$$

$$\frac{2n}{2n-1}\left(a_c^{\frac{2n-1}{2n}} - a_0^{\frac{2n-1}{2n}}\right) = \frac{M}{\rho}\left(\frac{\sigma Y}{\lambda K_c}\right)^{\frac{1}{n}}\left[\sqrt{\left(\frac{D}{k}\right)^2 + \frac{2D\rho c_0 t_R}{M}} - \frac{D}{k}\right] \tag{34}$$

Eq. (34) can be rearranged focusing on t_R:

$$\left[\frac{2n}{2n-1}\left(a_c^{\frac{2n-1}{2n}} - a_0^{\frac{2n-1}{2n}}\right)\frac{\rho}{M}\left(\frac{\sigma Y}{\lambda K_c}\right)^{-\frac{1}{n}} + \frac{D}{k}\right] = \sqrt{\left(\frac{D}{k}\right)^2 + \frac{2D\rho c_0 t_R}{M}} \tag{35}$$

$$\left[\frac{2n}{2n-1}\left(a_c^{\frac{2n-1}{2n}} - a_0^{\frac{2n-1}{2n}}\right)\frac{\rho}{M}\left(\frac{\sigma Y}{\lambda K_c}\right)^{-\frac{1}{n}} + \frac{D}{k}\right]^2 = \left(\frac{D}{k}\right)^2 + \frac{2D\rho c_0 t_R}{M} \tag{36}$$

$$\left[\frac{2n}{2n-1}\left(a_c^{\frac{2n-1}{2n}} - a_0^{\frac{2n-1}{2n}}\right)\frac{\rho}{M}\left(\frac{\sigma Y}{\lambda K_c}\right)^{-\frac{1}{n}} + \frac{D}{k}\right]^2 - \left(\frac{D}{k}\right)^2 = \frac{2D\rho c_0 t_R}{M} \tag{37}$$

Finally the solution of the system in term of failure time can be expressed as shown below:

$$t_R = \left(\frac{M}{2D\rho c_0}\right)\left[\frac{2n}{2n-1}\left(a_c^{\frac{2n-1}{2n}} - a_0^{\frac{2n-1}{2n}}\right)\frac{\rho}{M}\left(\frac{\sigma Y}{\lambda K_c}\right)^{-\frac{1}{n}} + \frac{D}{k}\right]^2 - \left(\frac{D}{k}\right)^2 \tag{38}$$

List of Figures

List of Tables

Bibliography

[1] A Aveston. Single and multiple fracture, the properties of fibre composites. In *Proceeding of Conference, National Physical Laboratories, IPC*, pages 15–24. Science and Technology Press, 1971.

[2] E Baranger, C Cluzel, P Ladevèze, and L Baroumes. Macro-modélisation de durée de vie de CMC à matrice autocicatrisante: capacité de prédiction actuelle et aide à la définition de nouveaux essais= lifetime macro-modelling of a self-healing ceramic matrix composite: current predictive capability and exploitation for new tests definition. In *JNC 16*, pages 10–p. AMAC, 2009.

[3] Y Bazilevs and T Hughes. Weak imposition of dirichlet boundary conditions in fluid mechanics. *Computers & Fluids*, 36(1):12–26, 2007. Challenges and Advances in Flow Simulation and Modeling.

[4] S Bertrand. Développement et optimisation des procédés CVI, appliqués à la fabrication de nouveaux matériaux composites thermostructuraux pour applications aéronautiques, spatiales et industrielles = CVI process development and optimization for new thermostructural composites, for aeronautical, spatial and industrial applications. In *JNC 16*, pages 7–p. AMAC, 2009.

[5] M Boyer. *Oxidation/Corrosion of ceramic matrix composites in aircraft type atmospheres*. PhD thesis, Master thesis, LCTS, Bordeaux I University, 2005.

[6] FJ Buchanan and JA Little. Glass sealants for carbon-carbon composites. *Journal of materials science*, 28(9):2324–2330, 1993.

[7] B Budiansky, JW Hutchinson, and AG Evans. Matrix fracture in fiber-reinforced ceramics. *Journal of the Mechanics and Physics of Solids*, 34(2):167–189, 1986.

[8] P Busquin, P Arguelles, J Lumsden, and M Bishoff. European aeronautics: A vision for 2020. *European Community, Bruxelles*, 2001.

[9] V Calard and J Lamon. Failure of fiber bundles. *Composites science and technology*, 64(5):701–710, 2004.

[10] G Camus. Modelling of the mechanical behavior and damage processes of fibrous ceramic matrix composites: application to a 2-D SiC/SiC. *International Journal of solids and Structures*, 37(6):919–942, 2000.

[11] N Carrère, E Martin, and J Lamon. The influence of the interphase and associated interfaces on the deflection of matrix cracks in ceramic matrix composites. *Composites Part A: Applied Science and Manufacturing*, 31(11):1179–1190, 2000.

[12] JL Chaboche and JF Maire. New progress in micromechanics-based CDM models and their application to CMCs. *Composites Science and Technology*, 61(15):2239–2246, 2001.

[13] JL Chaboche and JF Maire. A new micromechanics based CDM model and its application to CMCs. *Aerospace Science and Technology*, 6(2):131–145, 2002.

[14] FA Christin. A global approach to fiber nD architectures and self-sealing matrices: from research to production. *International Journal of Applied Ceramic Technology*, 2(2):97–104, 2005.

[15] C Cluzel, E Baranger, P Ladevèze, and A Mouret. Mechanical behaviour and lifetime modelling of self-healing ceramic-matrix composites subjected to thermomechanical loading in air. *Composites Part A: Applied Science and Manufacturing*, 40(8):976–984, 2009.

[16] BD Colman. On the strength of classical fibers and fiber bundles. *J. Mech. Phys. Solids*, 7:60, 1958.

[17] G Couégnat, V Dréan, W Ros, M Eric, M Ricchiuto, C Germain, M Cataldi, and GL Vignoles. Virtual material approach to self-healing CMCs. In *4th European Conference for Aerospace Sciences*, page nc, 2011.

[18] WA Curtin. Theory of mechanical properties of ceramic-matrix composites. *Journal of the American Ceramic Society*, 74(11):2837–2845, 1991.

[19] WA Curtin. The "tough" to brittle transition in brittle matrix composites. *Journal of the Mechanics and Physics of Solids*, 41(2):217–245, 1993.

[20] WA Curtin, BK Ahn, and N Takeda. Modeling brittle and tough stress–strain behavior in unidirectional ceramic matrix composites. *Acta Materialia*, 46(10):3409–3420, 1998.

[21] T Cutard. *Caractérisation ultrasonore à haute température et sous contrainte de traction de composites céramique-céramique*. PhD thesis, Limoges, 1993.

[22] HE Daniels. The statistical theory of the strength of bundles of threads. i. *Proceedings of the Royal Society of London. Series A. Mathematical and Physical Sciences*, 183(995):405–435, 1945.

[23] BE Deal and AS Grove. General relationship for the thermal oxidation of silicon. *Journal of Applied Physics*, 36(12):3770–3778, 1965.

[24] AG Evans, JM Domergue, and E Vagaggini. Methodology for relating the tensile constitutive behavior of ceramic-matrix composites to constituent properties. *Journal of the American Ceramic Society*, 77(6):1425–1435, 1994.

[25] AG Evans and DB Marshall. Overview no. 85 the mechanical behavior of ceramic matrix composites. *Acta Metallurgica*, 37(10):2567–2583, 1989.

[26] AG Evans and FW Zok. The physics and mechanics of fibre-reinforced brittle matrix composites. *Journal of Materials science*, 29(15):3857–3896, 1994.

[27] AG Evans, FW Zok, RM McMeeking, and ZZ Du. Models of high-temperature, environmentally assisted embrittlement in ceramic-matrix composites. *Journal of the American Ceramic Society*, 79(9):2345–2352, 1996.

[28] Z Fan, T Wei, J Shi, G Zai, J Song, L Liu, J Li, and J Chen. New route for preparation of SiC–B_4C/C composite with excellent oxidation resistance up to 1400 ℃. *Journal of materials science letters*, 22(3):213–215, 2003.

[29] Zn Fan, Y Song, J Li, L Liu, J Song, J Chen, G Zhai, and J Shi. Oxidation behavior of fine-grained SiC–B_4C/C composites up to 1400 ℃. *Carbon*, 41(3):429–436, 2003.

[30] G Fantozzi, P Reynaud, and D Rouby. Thermomechanical behaviour of long fibres ceramic-ceramic composites. *Silicates industriels*, pages 109–119, 2001.

[31] L Filipuzzi, G Camus, R Naslain, and J Thebault. Oxidation mechanisms and kinetics of 1D-SiC/C/SiC composite materials: I, an experimental approach. *Journal of the American Ceramic Society*, 77(2):459–466, 1994.

[32] P Forio and J Lamon. Fatigue behavior at high temperatures in air of a 2D SiC/Si-B-C composite with a self-healing multilayered matrix. *Advances in Ceramic Matrix Composites VII*, 128:127–141, 2006.

[33] P Forio, F Lavaire, and J Lamon. Delayed failure at intermediate temperatures (600–700 °C) in air in silicon carbide multifilament tows. *Journal of the American Ceramic Society*, 87(5):888–893, 2004.

[34] E Garitte. *Etude de l'oxydation/corrosion des composites céramiques*. PhD thesis, Bordeaux 1, 2007.

[35] E Garitte, F Rebillat, and A Guette. B_4C as the precursor of the healing in a SiC/SiC composite: behaviour under wet atmosphere. In *Proceedings of the 12th European Conference on Composite Materials (ECCM12)*, 2006.

[36] A Gasser, P Ladevèze, and M Poss. Damage mechanisms of a woven SiC/SiC composite: Modelling and identification. *Composites Science and Technology*, 56(7):779–784, 1996.

[37] W Gauthier and J Lamon. Delayed failure of Hi-Nicalon and Hi-Nicalon S multifilament tows and single filaments at intermediate temperatures (500–800 °C). *Journal of the American Ceramic Society*, 92(3):702–709, 2009.

[38] W Gauthier, J Lamon, and R Pailler. Fatigue statique de monofilaments et de fils SiC Hi-Nicalon at 500 °C et 800 °C. *Revue des Composites et des Matériaux Avancés*, 16(2):221, 2006.

[39] W Gauthier, F Pailler, J Lamon, and R Pailler. Oxidation of silicon carbide fibers during static fatigue in air at intermediate temperatures. *Journal of the American Ceramic Society*, 92(9):2067–2073, 2009.

[40] M Genet, L Marcin, E Baranger, C Cluzel, P Ladevèze, and A Mouret. Computational prediction of the lifetime of self-healing CMC structures. *Composites Part A: Applied Science and Manufacturing*, 43(2):294–303, 2012.

[41] S Goujard, JL Charvet, JL Leluan, F Abbé, and G Lamazouade. Matériau composite protégé contre l'oxydation par une matrice autocicatrisante et son procédé de fabrication. *French Patent*, (FR95-03606), 1995.

[42] AI Grigor'ev and DI Polishchuk. Determination of the coefficient of oxygen diffusion in boron oxide and its dependence on temperature. *Fizika Aerodispersnykh Sistemykh*, 8:87–90, 1973.

[43] L Guillaumat and J Lamon. Probabilistic-statistical simulation of the non-linear mechanical behavior of a woven SiC/SiC composite. *Composites Science and Technology*, 56(7):803–808, 1996.

[44] R. Gulino and SL Phoenix. Weibull strength statistics for graphite fibres measured from the break progression in a model graphite/glass/epoxy microcomposite. *Journal of Materials Science*, 26(11):3107–3118, 1991.

[45] CY Hui, SL Phoenix, M Ibnabdeljalil, and RL Smith. An exact closed form solution for fragmentation of weibull fibers in a single filament composite with applications to fiber-reinforced ceramics. *Journal of the Mechanics and Physics of Solids*, 43(10):1551–1585, 1995.

[46] N Jacobson, D Myers, E Opila, and E Copland. Interactions of water vapor with oxides at elevated temperatures. *Journal of Physics and Chemistry of Solids*, 66(2-4):471–478, 2005.

[47] NS Jacobson, GN Morscher, DR Bryant, and RE Tressler. High-temperature oxidation of boron nitride: II, boron nitride layers in composites. *Journal of the American Ceramic Society*, 82(6):1473–1482, 1999.

[48] A Kaflou. *Etude du comportement des interfaces et des interphases dans les composites à fibres et à matrices céramiques.* PhD thesis, Lyon, INSA, 2006.

[49] RJ Kerans. Life-limiting behavior and life management of SiC-based composites. *Engineered Ceramics: Current Status and Future Prospects*, pages 160–186, 2015.

[50] K Kobayashi, K Maeda, H Sano, and Y Uchiyama. Formation and oxidation resistance of the coating formed on carbon material composed of B_4C–SiC powders. *Carbon*, 33(4):397–403, 1995.

[51] W Krenkel. *Ceramic matrix composites: fiber reinforced ceramics and their applications.* John Wiley & Sons, 2008.

[52] P Ladevèze. Sur une thèorie de l'endommagement anisotrope. rapport interne n. 34. *Laboratoire de Mécanique et Technologie, Cachan*, 1983.

[53] P Ladevèze. Modeling and simulation of the mechanical behavior of CMC. In *Procs. 3rd Intl. Conf. on High-Temperature Ceramic-Matrix Composites*, pages 53–63, 1995.

[54] P Ladevèze. An anisotropic damage theory with unilateral effects: applications to laminates and to three-and four-dimensional composites. *Continuum damage mechanics of materials and structures*, pages 205–233, 2002.

[55] P Ladevèze, A Gasser, and O Allix. Damage mechanisms modeling for ceramic composites. *Journal of Engineering Materials and Technology*, 116(3), 1994.

[56] P Ladevèze and M Genet. A new approach to the subcritical cracking of ceramic fibers. *Composites Science and Technology*, 70(11):1575–1583, 2010.

[57] P Ladevèze, S Letombe, and C Cluzel. A CMC damage model based on micro-and macromechanics for high-temperature and complex loading. pages 578–583. Wiley-VCH, 2001.

[58] A Laforêt. *Rupture différée en fatigue statique aux très hautes températures (800°C–1300°C) des fils Hi-Nicalon, des composites Hi-Nicalon/Type PyC/SiC et des composites Hi-Nicalon Type PyC/B4C*. PhD thesis, Bordeaux 1, 2009.

[59] J Lamon. A micromechanics-based approach to the mechanical behavior of brittle-matrix composites. *Composites science and technology*, 61(15):2259–2272, 2001.

[60] J Lamon. *Mécanique de la rupture fragile et de l'endommagement: approches statistiques et probabilistes*. Hermes Sciences, 2007.

[61] F Lamouroux, S Bertrand, R Pailler, and R Naslain. A multilayer ceramic matrix for oxidation resistant carbon fibers-reinforced CMCs. *Key Engineering Materials*, 164, 1999.

[62] F Lamouroux, S Bertrand, R Pailler, R Naslain, and M Cataldi. Oxidation-resistant carbon-fiber-reinforced ceramic-matrix composites. *Composites Science and Technology*, 59(7):1073–1085, 1999.

[63] CM Landis, IJ Beyerlein, and RM McMeeking. Micromechanical simulation of the failure of fiber reinforced composites. *Journal of the Mechanics and Physics of Solids*, 48(3):621–648, 2000.

[64] M Leparoux, L Vandenbulcke, V Serin, J Sevely, S Goujard, and C Robin-Brosse. Oxidizing environment influence on the mechanical properties and microstructure of 2D - SiC/BN/SiC composites processed by ICVI. *Journal of the European Ceramic Society*, 18(6):715–723, 1998.

[65] S Letombe. *Modélisation du couplage oxydation/endommagement des Compositesa Matrice Céramique Autocicatrisante*. PhD thesis, PhD thesis. ENS-Cachan, 2005.

[66] L Li. A time-dependent tensile constitutive model for long-fiber-reinforced unidirectional ceramic-matrix minicomposites considering interface and fiber oxidation. *International Journal of Damage Mechanics*, 29(7):1138–1166, 2020.

[67] N Lissart and J Lamon. Damage and failure in ceramic matrix minicomposites: experimental study and model. *Acta Materialia*, 45(3):1025–1044, 1997.

[68] JF Maire and JL Chaboche. A new formulation of continuum damage mechanics (CDM) for composite materials. *Aerospace Science and Technology*, 1(4):247–257, 1997.

[69] JF Maire and PM Lesne. A damage model for ceramic matrix composites. *Aerospace science and technology*, 1(4):259–266, 1997.

[70] S Marelli and B Sudret. *UQLab: A framework for uncertainty quantification in Matlab*. American Society of Civil Engineers, 2014.

[71] S Marelli and B Sudret. UQLab user manual–polynomial chaos expansions. *Chair of risk, safety & uncertainty quantification, ETH Zürich*, pages 97–110, 2015.

[72] DB Marshall, BN Cox, and AG Evans. The mechanics of matrix cracking in brittle-matrix fiber composites. *Acta metallurgica*, 33(11):2013–2021, 1985.

[73] X Martin. *Oxydation/corrosion de matériaux composites (SiC_f/SiC_m) à matrice auto-cicatrisante*. PhD thesis, Université Bordeaux 1, 2003.

[74] R Muller. Acare goals (agape) progress evaluation. *Project Final Report Publishable Summary, Support Action Funding Scheme, Proposal*, (205768), 2010.

[75] R Naslain. The design of the fibre-matrix interfacial zone in ceramic matrix composites. *Composites Part A: Applied Science and Manufacturing*, 29(9-10):1145–1155, 1998.

[76] R Naslain, A Guette, F Rebillat, R Pailler, F Langlais, and X Bourrat. Boron-bearing species in ceramic matrix composites for long-term aerospace applications. *Journal of Solid State Chemistry*, 177(2):449–456, 2004.

[77] R Naslain, J Lamon, R Pailler, X Bourrat, A Guette, and F Langlais. Micro/minicomposites: a useful approach to the design and development of

non-oxide CMCs. *Composites Part A: applied science and manufacturing*, 30(4):537–547, 1999.

[78] S Pasquier. *Comportement thermomécanique d'un composite de type SiC/SiC à interphase séquencée: effet de l'environnement*. PhD thesis, Bordeaux 1, 1997.

[79] O Penas, P Reynaud, D Rouby, and G Fantozzi. Self-healing SiCf/SiC composite behaviour under high-temperature cyclic fatigue in air. In *Procs. 5th Intl. Conf. on High-Temperature Ceramic-Matrix Composites*, pages 480–485. Wiley-VCH, 2001.

[80] G Perrot. *Modélisation du comportement des composites à matrice céramique auto-cicatrisante sous charge et atmosphère oxydante*. PhD thesis, Bordeaux, 2015.

[81] G Perrot, G Couégnat, M Ricchiuto, and GL Vignoles. Image-based numerical modeling of self-healing in a ceramic-matrix minicomposite. *Ceramics*, 2(2):308–326, 2019.

[82] SL Phoenix. Probabilistic strength analysis of fibre bundle structures. *Fibre Science and Technology*, 7(1):15–31, 1974.

[83] SL Phoenix and R Raj. Overview no. 100 scalings in fracture probabilities for a brittle matrix fiber composite. *Acta Metallurgica et Materialia*, 40(11):2813–2828, 1992.

[84] SL Phoenix and HM Taylor. The asymptotic strength distribution of a general fiber bundle. *Advances in Applied Probability*, 5(2):200–216, 1973.

[85] F Rebillat. Original 1D oxidation modeling of composites with complex architectures. In *Procs. 5th Intl. Conf. on High-Temperature Ceramic-Matrix Composites*, pages 315–320. Wiley-VCH, 2005.

[86] F Rebillat. Advances in self-healing ceramic matrix composites. In *Advances in ceramic matrix composites*, pages 475–514. Elsevier, 2014.

[87] F Rebillat, J Lamon, R Naslain, E Lara-Curzio, MK Ferber, and TM Besmann. Properties of multilayered interphases in SiC/SiC chemical-vapor-infiltrated composites with "weak" and "strong" interfaces. *Journal of the American Ceramic Society*, 81(9):2315–2326, 1998.

[88] RC Reid, JM Prausnitz, and BE Poling. The properties of gases and liquids. 1987.

[89] D Rouby and N Louet. The frictional interface: a tribological approach of thermal misfit, surface roughness and sliding velocity effects. *Composites Part A: Applied Science and Manufacturing*, 33(10):1453–1459, 2002.

[90] D Rouby and P Reynaud. Fatigue behaviour related to interface modification during load cycling in ceramic-matrix fibre composites. *Composites Science and Technology*, 48(1-4):109–118, 1993.

[91] G Savage. The properties of carbon-carbon composites. In *Carbon-Carbon Composites*, pages 277–322. Springer, 1993.

[92] B Schneider. *Sur l'oxydation active des céramiques à base de carbure de silicium*. PhD thesis, Bordeaux 1, 1995.

[93] A Shojaei, G Li, J Fish, and PJ Tan. Multi-scale constitutive modeling of ceramic matrix composites by continuum damage mechanics. *International Journal of Solids and Structures*, 51(23-24):4068–4081, 2014.

[94] J Steibel. Ceramic matrix composites taking flight at GE aviation. *Am. Ceram. Soc. Bull*, 98(3):30–33, 2019.

[95] M Sutcu. Weibull statistics applied to fiber failure in ceramic composites and work of fracture. *Acta Metallurgica*, 37(2):651–661, 1989.

[96] M Takeda, A Urano, J Sakamoto, and Y Imai. Microstructure and oxidative degradation behavior of silicon carbide fiber Hi-Nicalon type S. *Journal of Nuclear Materials*, 258:1594–1599, 1998.

[97] JP Viricelle, DJ Bahloul-Hourlier, and P Goursat. Oxidation behaviour of a sic based fiber. In *Key Engineering Materials*, volume 127, pages 203–210. Trans Tech Publ, 1997.

[98] JB Wachtman, WR Cannon, and MJ Matthewson. *Mechanical properties of ceramics*. John Wiley & Sons, 2009.

[99] J Wang, L Z, Q Z, GL Vignoles, and A Guette. Theoretical investigation for the active-to-passive transition in the oxidation of silicon carbide. *Journal of the American Ceramic Society*, 91(5):1665–1673, 2008.

[100] W Weibull. A statistical distribution function of wide applicability. *Journal of applied mechanics*, 1951.

[101] S Wéry. *Etude de la réactivité de composites à matrice céramique á haute température*. PhD thesis, Perpignan, 2011.

[102] S Wery and F Teyssandier. Physico-chemical reactivity of ceramic composite materials at high temperature: Vaporization and reactivity with carbon of borosilicate glass. In *Procs. 31st International Conference on Advanced Ceramics and Composites, Daytona Beach, Florida*, pages 307–317. John Wiley & Sons, Inc. Hoboken, NJ, USA, 2007.

[103] S Wery and F Teyssandier. Use of the sessile drop method to understand the behaviour of self healing ceramic matrix composite. In *Materials Science Forum*, volume 595, pages 1173–1180. Trans Tech Publ, 2008.

[104] SM Wiederhorn, ER Fuller, and R Thomson. Micromechanisms of crack growth in ceramics and glasses in corrosive environments. *Metal Science*, 14(8-9):450–458, 1980.

[105] S Zhu, M Mizuno, Y Kagawa, and Y Mutoh. Monotonic tension, fatigue and creep behavior of SiC-fiber-reinforced SiC-matrix composites: a review. *Composites Science and Technology*, 59(6):833–851, 1999.

[106] O Zienkiewicz, R Taylor, and J Zhu. *The finite element method: its basis and fundamentals*. Elsevier, 2005.